The Cross-linking Mechanism of Filamin A in the Actin Cytoskeleton

by

Christopher A. Hartemink

B.S., Mechanical Engineering, Calvin College, 1996

B.S., Physics, minor in Mathematics, Calvin College, 1996

S.M., Mechanical Engineering, Massachusetts Institute of Technology, 1999

SUBMITTED TO THE DIVISION OF HEALTH SCIENCES AND TECHNOLOGY IN PARTIAL FULFILLMENT OF THE REQUIREMENTS FOR THE DEGREE OF

DOCTOR OF PHILOSOPHY IN
MECHANICAL AND MEDICAL ENGINEERING
AT THE
MASSACHUSETTS INSTITUTE OF TECHNOLOGY

JUNE 2005

Signature of Author:.....
Harvard–MIT Division of Health Sciences and Technology
February 10, 2005

Certified by:.....
C. Forbes Dewey, Jr., Ph.D.
Professor of Mechanical Engineering and Bioengineering
Massachusetts Institute of Technology
Thesis Supervisor

Certified by:.....
John H. Hartwig, Ph.D.
Professor of Cell Biology
Harvard Medical School
Thesis Supervisor

Accepted by: .....
Martha L. Gray, Ph.D.
Edward Hood Taplin Professor of Medical and Electrical Engineering
Co-Director, Harvard–MIT Division of Health Sciences and Technology

The Cross-linking Mechanism of Filamin A in the Actin Cytoskeleton

by

Christopher A. Hartemink

Submitted to the Harvard–MIT Division of Health Sciences and
Technology on February 10, 2005 in Partial Fulfillment of the Requirements
for the Degree of Doctor of Philosophy in
Mechanical and Medical Engineering

Eukaryotic cells are permeated by a three-dimensional network of entangled filamentous proteins termed the cytoskeleton. Like scaffolding, the cytoskeleton provides rigidity and resistance to deformation from forces transmitted to and from the cell membrane.

In order to model the mechanics of the cytoskeleton, the interaction of individual structural proteins must be established. To this end the relationship between two critical proteins of the actin cytoskeleton is examined. Actin reversibly assembles into filaments that provide cells with shape and confer to the cell its mechanical properties. Filamin is an abundant actin-binding protein that efficiently cross-links actin filaments in large-angle orientations, requiring the lowest concentration to convert actin filaments into a cohesive gel.

Filamin dimers are composed of two 24-repeat domains that come together like a V with an actin-binding region at each free end. Analysis reveals that the repeat domains of filamin are more flexible than the self-association region of the dimer. These findings dispute the initial claim that filamin is a rigid molecule. This thesis investigates the binding modality of filamin to actin. The structure of filamin bound to actin was compared to filamin in solution and immunogold molecules bound along the filamin rod were used to map the 3-D organization of filamin-actin junctions. There is evidence that filamin binds to actin at more sites than filamin's two established N-terminal actin-binding sites.

These features, flexible repeat extensions, multiple-site binding, and a rigid self-association region, make filamin a potent cross-linking agent. The long flexible extensions allow filamin molecules to sample a large volume of cytoplasm in search of an actin target. The binding length of filamin along actin filaments provides a less-flexible linkage from actin to the rigid filamin self-association region, enabling reproducible large angles. At the same time, filamin brings actin filaments into close proximity, creating tight network entanglement, while filamin's angle prevents linked actin filaments from slipping into dense bundles as they do with short cross-linkers like α-actinin, instead maintaining a strong, disperse network. Tightly constrained junctions support recent entropic and enthalpic models of the cytoskeleton.

Thesis Supervisor: C. Forbes Dewey, Jr., Ph.D.
Title: Professor of Mechanical Engineering and Bioengineering, MIT

Thesis Supervisor: John H. Hartwig, Ph.D.
Title: Professor of Cell Biology, Harvard Medical School

About the Author

Chris Hartemink grew up in Fort Myers Florida and has long been drawn to the interface of engineering and human welfare. He attended Calvin College, a liberal arts school in Grand Rapids Michigan, where he developed his soul and his mind. After a lengthy tenure in biology at MIT for graduate school, including two years at Harvard Medical School, Chris now works at Guidant in Minneapolis, Minnesota, working on heart failure resynchronization in Applied Research for the Cardiac Rhythm Management division, returning to his engineering and design roots.

Acknowledgements

A thesis in the sciences is a monumental undertaking, and could never be done alone. I would like to thank, first and foremost, my two advisors. **Professor C. Forbes Dewey** took a chance on a young ideological engineer coming from an unknown school, and may have regretted his choice at times. But he has been a good source of encouragement and guidance throughout the years in his efforts to transform me into a high-caliber scientist worthy of MIT's highest degree. **Professor John Hartwig** has been my day-to-day advisor in the laboratory. Letting a mechanical engineer into his cell biology lab was a significant risk, and I pray I have not done more harm than good. I realize I did not always fit the mold of a biologist, and I hope someday John can forgive me. He has been supportive and instructive, and I sincerely appreciate him taking me under his wing as I ventured into an entirely new field. I would also like to thank **Fumi Nakamura**, **Ralph Neujahr**, and **Kurt Barkalow**, three post-docs in the laboratory, for their constant advice and instruction on technical matters in biology protocols, preparations, and procedures. Finally I'd like to thank the **technicians** who were always willing to order the supplies I requested, kept the lab stocked with equipment, and greeted me with smiles.

On the personal side I have to thank **Samantha**, my wife of five years now, for her ceaseless support and sacrifice. She put up with the excessive, irregular hours of a graduate student without complaint, and I never could have done it without her love. Likewise, my brother **Alex** has been an inspiration from the day I was born. Our five years together at MIT were some of the greatest of my life, and I thank him for his fraternity and even more so his friendship. I want to also thank my **Mom and Dad**, who on more than one occasion talked me into staying with it when the night was cold and dark. They have led me to fulfill my potential by example, and I thank them.

I would also like to thank my wonderful MIT/HST classmates with whom I've bonded and commiserated, as well the beautiful women of Alpha Phi who offered me their home, just a mile from the lab, where I spent many short nights.

Historical Contributions

In 1870, Ernest Abbe postulated that the resolution for a microscope was limited by the wavelength of the beam. For 50 years, the practical limit of light microscopes was 200 nm. In 1924, Antone de Broglie postulated that electrons have a wave nature, and thus a wavelength. At 60 kV, the resolution of electrons would be on the order of 0.005 nm, an improvement of 200,000 over light. In 1926, Hermann Busch discovered that magnets can deflect electrons, and thus act as lenses. In 1931, armed with these foundations, Max Knoll and Ernst Ruska built the first electron microscope, an achievement for which Ruska would win the Nobel Prize in Physics in 1986.

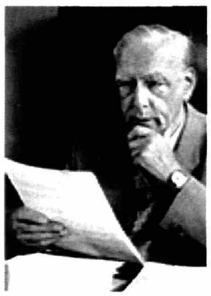

Ernst Ruska

In 1959, two biochemists separately discovered the structure and function of antibodies. Rodney Porter discovered that papain cleaved antibodies, and from the products determined that antibodies have two functional domains and a base. Simultaneously, Gerald Edelman presumed that antibodies were two separate chains held together by disulfide bonds. By severing these bonds, he proved his presumptions correct. With these findings, both gentlemen showed that antibodies are comprised of two identical light chains and two identical heavy chains. For launching the exploding field of immunochemistry, both men shared the Nobel Prize in Physiology or Medicine in 1972.

Rodney Porter

Dedication

I dedicate this thesis to Samantha, my Penelope, and Matthew, my Telemachus.

In honor of my Father, my father, and my father's father.

Table of Contents

Table of Figures

Table of Tables

Chapter 1 The Cytoskeleton and Cellular Models

The human body comprises one hundred million million (10^{14}) cells which are divided into 200 widely diverse types, from meter-long neurons to regenerative liver cells [1]. Each of these cell types performs a highly specialized function in the body and that function depends on many factors, including the cell's shape, strength, and mobility. Cells are not passive building blocks like bricks or atoms; the dynamic nature of cells sustains life as they adapt to stimuli by growing, proliferating, communicating, specializing, and coordinating.

To provide a foundation for this incredible demand, a three-dimensional network called the cytoskeleton permeates each cell of the human body (Figure 1.1). The cytoskeleton is responsible for a variety of cell functions, including separation of chromosomes during mitosis, intracellular trafficking of organelles, maintenance of cell membrane integrity under stress and strain, contraction of muscles, penetration of neurons through the brain, and motility of cells from swimming sperm to crawling fibroblasts [2]. Although it is often compared to construction scaffolding in appearance and function, the cytoskeleton is a complicated, ever-changing structure that adapts and remodels every minute to best suit its purpose, much like the cell itself.

The cells that compose the blood-surface monolayer of the cardiovasculature are termed endothelial cells. These cells provide a non-coagulative surface for blood vessels, regulate the passage of chemicals into and out of the blood supply, and transduce mechanical flow signals to the vessel muscles below them to maintain blood pressure and flow rates. Endothelial cells also initiate angiogenesis, the formation of new blood vessels, in response to factors like vascular endothelial growth factor (VEGF) which are secreted by tissues after wounding, after infection or during growth. As such, a healthy endothelium helps prevent heart disease and circulatory disorders while contributing to healing and development. Damaged endothelium, on the other hand, contributes to pathologic processes such as atherosclerotic progression of plaque formation in blood vessels. In the case of cancer, the therapeutic strategy is reversed: because tumors cannot thrive without nutrients carried by blood, one current therapy for cancer locally disrupts endothelial angiogenesis to weaken the disease. For both cardiovascular disorders and cancer, the ability to understand the function of endothelial cells enables the advancement of medical treatment.

Atherosclerotic lesions develop predominately at regions within the arterial tree where turbulence and shear stress irregularities occur, such as highly curved or bifurcating blood vessels [3]. Twenty-five years ago scientists demonstrated that endothelial cells rearrange their cytoskeletons to align with shear stress [4], which provides a connection between cell response and tissue damage. Neither the mechanism nor the purpose of this alignment is well understood. The mechanism of realignment involves a signaling pathway from receptors on the cell surface to the proteins and nucleus within the cell, but the precise details have not yet been confirmed.

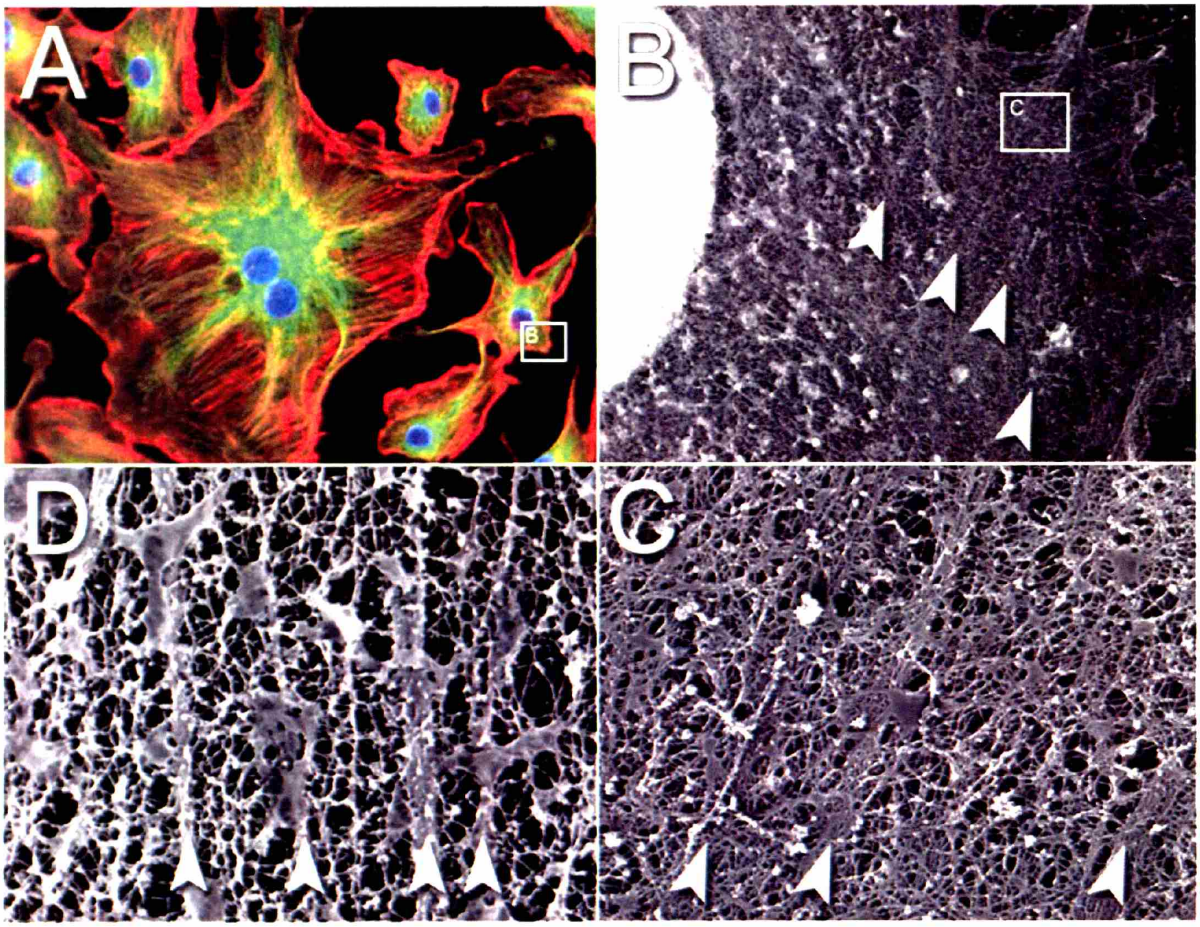

Figure 1.1 The endothelial cytoskeleton in increasing magnification, clockwise. A, Fluorescently labeled endothelial cell cytoskeletons with nuclei stained blue, F-actin stained red, and microtubules stained green. The "striped" actin appearance throughout the cells is due to the bundling of F-actin into stress fibers which are differentiable at optical resolution, panel width 200 μm. B, Higher magnification reveals that the cells actually contain a pervasive network of actin filaments that fills the space between stress fibers (arrowheads), staining a diffuse red in fluorescent imaging, panel width 20 μm. C, D, Increasing magnification of the network showing it to be a dense, porous, evenly-distributed web of individual filaments. The pore size of the network is approximately 100 nm, (A, image courtesy of Molecular Probes. B-D, images courtesy of John Hartwig. All four panels are taken from different cells; inset boxes are placed solely for scale).

The purpose of realignment is likely mechanical stiffening of the cell and strengthening of the monolayer, but how this change in cell shape affects cell mechanics has not been elucidated.

Understanding how these cells respond to shear stress to protect the endothelium may prove critical for understanding how atherosclerosis, the leading cause of death in the United States, develops.

Three protein structures constitute the cytoskeletal network: actin filaments, microtubules, and intermediate filaments. Additionally, dozens of binding proteins modulate these principal members. Some of these secondary proteins serve regulatory functions, such as capping and sequestering proteins, and some serve structural functions, such as bundling and cross-linking proteins. Several structural actin-binding proteins are listed in Table 1.1.

Table 1.1 Structural binding proteins of actin and their properties

Name	Shape	Molecular Weight	Common Location	Other
α-actinin	30 nm anti-parallel overlapping dimeric rod	100 kDa	Loose bundles in cells	
Arp2/3	10 × 15 nm ellipsoid	225 kDa	Cell cortex branches, bacterial "comet tails"	
Dystrophin	150 nm rod	430 kDa	Near muscle cell membranes	
Fascin	5 nm globular monomer	55 kDa	Tight bundles within membrane protrusions	
Filamin	160 nm V-shaped dimer	560 kDa (dimer)	3-D large-angle junctions throughout cells	
Fimbrin	14 nm rod	20 kDa	Tight bundles in cells	
Fodrin	200 nm anti-parallel overlapping tetrameric rod	240 kDa (monomer)	2-D large-angle junctions near membrane	Non-erythroid spectrin
Scruin	10 nm rod	120 kDa	Tight bundles in sperm acrosomes	Coats actin in perpendicular fashion; scruin cross-links by binding to each other, not multiple F-actin
Spectrin	200 nm anti-parallel overlapping tetrameric rod	930 kDa (tetramer)	2-D large-angle junctions near membranes	In erythrocytes
Titin	1000 nm rod	3000 kDa	Muscle sarcomeres	Largest known protein
Villin	10 nm rod	95 kDa	Tight bundles in microvilli	Related to gelsolin

1.1 Cellular experiments

While there is ample equipment to measure the stiffness of polymer networks resembling the cytoskeleton *in vitro*, the cytoskeleton is too complicated to be fully reconstituted. Therefore, the most direct way to probe the stiffness of cytoskeletons is to measure cells. There are a variety of techniques to study cell stiffness, including twisting magnetic beads attached to the surface of a cell [5-7], aspirating part of a cell into a micropipette [8, 9], pulling on a cell membrane with magnetic beads [10], compressing or shearing a cell between surfaces [11], and using atomic force microscopy [12, 13]. In addition to the variety of techniques, scientists perform these experiments on a variety of cell types including fibroblasts [10, 11], endothelial cells [7-9], epithelial cells [6], and myocytes [5, 12, 13]. Figure 1.2 summarizes these results.

The variation in reported values of the cell modulus may be due to genuine differences in cytoskeletal composition and architecture of different cell types. However, limiting the comparison to endothelial cells yields a modulus which varies from 1 Pa to 100 Pa.

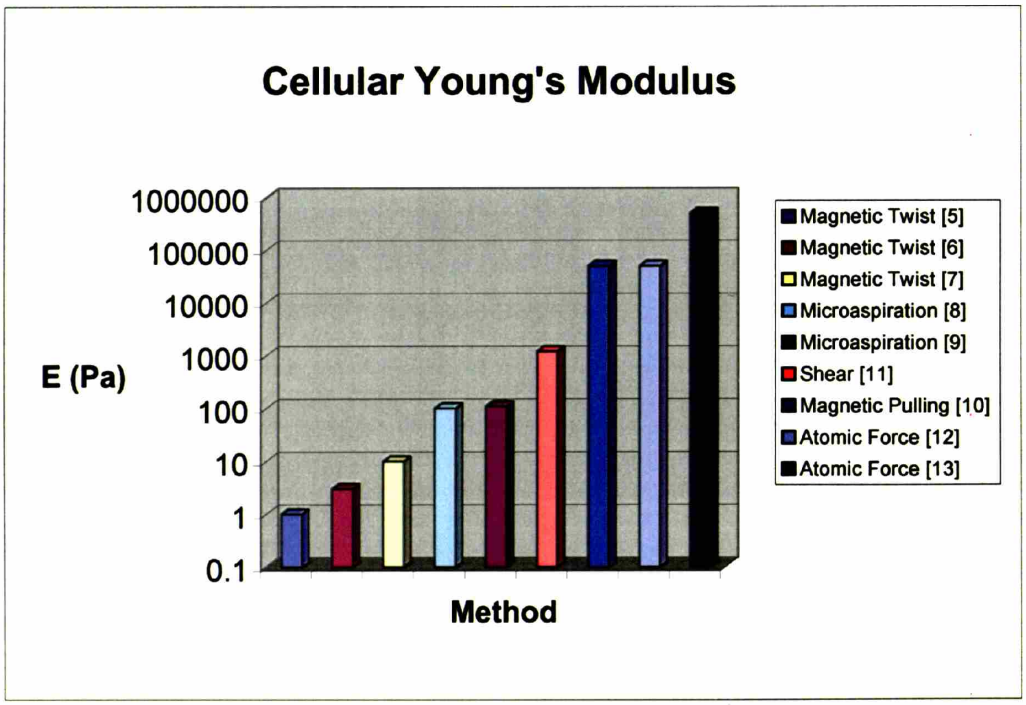

Figure 1.2 The elasticity of cells varies widely in the literature due to varying measurement techniques, cell types, and cell conditions. The total range is over 5 orders of magnitude, with even the same methods varying more than one order.

These variations could be temporal, as mechanical properties are dependent on cell state, and they could be spatial, since the cytoskeleton is not homogeneous. As well, each method measures a different mode of deformation: measuring the motion of a bead being twisted on a cell's membrane may not test the same aspect of cell structure that sucking a cell into a pipette does.

1.2 Cellular models

An alternate approach to determining cell stiffness is calculating the expected stiffness of a filamentous-protein model. One approach uses actin properties reported in the literature to attempt a quantitative analysis of the cell cytoskeleton, constructing a system of beams as shown in Figure 1.3A [14]. The deformation of the structure is based on the filaments bending under compression and shear. By treating the cell as a "cellular solid" (akin to paper, cork, or bread) actin density and stiffness are extrapolated to the shear modulus of an endothelial cell. The stiffness of the "cellular solid" is 10^4 Pa, in the middle of the range of cell measurements.

The scaling of this model is not dependent on the specifics of the protein interactions or the geometry. The chief parameter of the cellular solid model for open cell foams is the effective polymer density [15] which affects beam length and hence bending deflection.

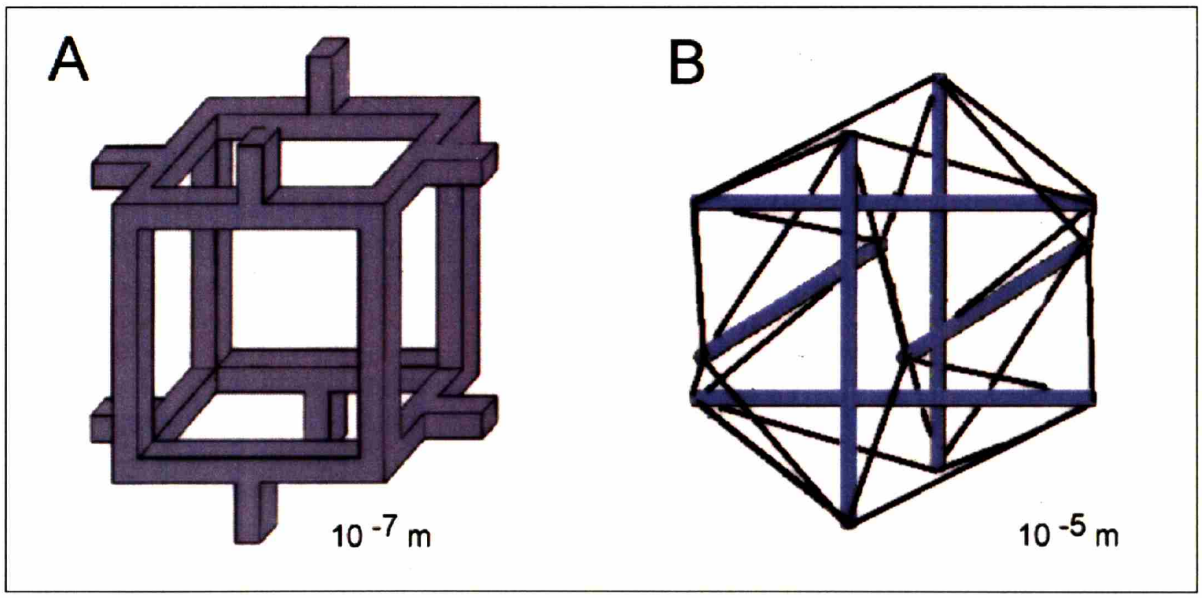

Figure 1.3 A, One pore of the "cellular solid" model for the cell (length scale 100 nm); the whole cell is modeled as a repeating lattice of such units. Actin filaments are considered beams which deflect under compression and shear. This stylized model predicts the cell stiffness is comparable to the higher values reported in experiments. B, The "tensegrity" model of the entire cell (length scale, 10 μm). The large gray elements are microtubules in compression and the black cables are elastic actin filaments in tension. The cell resembles a common children's toy that balances tension and compression to maintain a deformable structure.

Another theory, tensegrity, hypothesizes that the cell is like a geodesic dome, as shown in Figure 1.3B. The interaction between actin filaments in tension and microtubules in compression [16-19]; creates the cell's dynamic nature. The tensegrity concept derives from the fact that the cell membrane is in tension and exerts a force on the substrate to which it is bound.

Both these models, while conceptually powerful, simplify the details of the cytoskeleton. The cellular solid model assumes a perfectly organized cytoskeleton with perfectly rigid cross-linking at every junction – likely explaining why its stiffness is high. The tensegrity model incorporates no specific structural protein details aside from a handful of actin filaments and microtubules; no mention is made of architecture, protein concentrations, or cross-linking, and no numerical estimate for cell stiffness is proffered.

1.3 Analysis of *in vitro* actin networks

In order to understand the role of cross-linking, the protein network must be modeled at the molecular level. Each of the three cytoskeletal polymers has been isolated and studied in detail and actin is believed to impart dynamic mechanical structure to the cell [20-23]. Experiments show that disrupting the cell membrane [24, 25] or microtubules [6] has little effect on cell structure, whereas disrupting the actin network has great effect [6, 12]. Disrupting the actin cytoskeleton reduces cell stiffness sixfold. Preliminary mathematical modeling demonstrates that the few actin stress fibers (bundles) in a cell contribute little to mechanical stiffness [14]. For these reasons it is believed that the distributed actin network provides primary mechanical structure to cells. The similarity between cross-linked actin networks and cell cytoskeletons in electron micrographs further demonstrates that reconstituted actin networks provide a model system for cytoskeletal study [26]. The cellular solid model assumes permanent, perfectly stiff cross-linkers at every junction. The tensegrity model does not include cross-linkers in its analysis. Modeling the interaction of individual filaments and cross-linkers provides insight into the mechanical behavior of a complicated, irregular network like the cytoskeleton.

The field of actin polymer mechanics has exploded in the past decade because of an interest in the molecule from a physical perspective. Actin networks dissipate energy in a thermally energetic medium through bending, reptating (sliding), or stretching. As a result, the network possesses a stiffness and resists deformation even without cross-links between filaments. Actin forms polymers that are neither flexible nor rigid, instead being classified as "semi-flexible." As a representative of this class of polymer, there are numerous experimental and theoretical studies of pure actin gels detailing their stiffness, frequency dependence, and concentration dependence. Many explore actin networks using microrheology, such as particle tracking [27-44] or diffusing wave spectrometry [43-52]. There is also great interest in modeling the dynamics of semi-flexible polymers to interpret experimental data [53-70]; a few models are discussed in more detail in Chapter 6. However, these studies are not directly applicable to cells because they omit the crucial detail of cross-linking: "Cross-linking impurities present in very low concentrations would be sufficient to significantly modify the elastic behavior [of an entangled polymer model];

indeed, impurities present at the level of a few parts per thousand would be enough to invalidate it" [63]. In the cell, cross-linkers are present at a molar ratio to actin as high as 1:10 [71-73].

In vitro rheology experiments have shown that actin gels must be cross-linked to be strong enough support a cell [51]. The dramatic effect of cross-linking *in vitro* has been demonstrated by several groups. Several reports have shown that cross-linking with filamin increases the stiffness of actin gels by several orders of magnitude [74-77] using a variety of techniques, although the degree of the increase varies with experimental conditions and protocols. For example, with an actin concentration of 50 μM, adding filamin at a concentration of 1:100 with actin twentyfold [74]. The strongest evidence for the importance of filamin cross-linking *in vivo* is the deleterious state of cells without it. M2 is a melanoma cell line naturally lacking the primary isoform of filamin. Despite expressing approximately wild-type levels of gelsolin, α-actinin, profilin, fodrin, and the Arp2/3 complex, M2 cells are unable to crawl and have a surface replete with spherical aneurysms (blebs) indicating a lack of cortical stability [78, 79]. Rescuing these cells with filamin cDNA results in the reappearance of lamellar protrusions and membrane ruffles and restores a normal motile phenotype [79].

There is not yet an established model for cross-linked semi-flexible polymers, although there have been recent offerings [69, 70, 80, 81]. Classic studies of the dynamics of flexible polymers like rubber show that cross-linked flexible polymer gels are linearly dependent on cross-linker density [82, 83]. This flexible analysis has been adapted to actin networks, reaching the same linear dependence conclusion [84]. However, in these analyses, polymers are so flexible that they can pass through each other, and even themselves, which renders their physical applicability uncertain. Two experimental reports confirm that the change in actin network rigidity is linearly dependent on cross-linking [75, 76].

The importance of the structure of the cross-linker on network stiffness is unknown. Cross-linkers may tether filaments together to restrain diffusion, in which case the structure of the cross-linker is negligible and all cross-linkers should stiffen networks similarly. Cross-linkers may physically reinforce the actin junction, the impact of which would depend strongly on cross-linker structure. Several studies have demonstrated great difference in the potency of different cross-linkers at the same concentrations. These studies differentiate between different classes of cross-linkers (α-actinin and filamin [77, 85]), different members of the same cross-linker family (human filamin and *Dictyostelium* filamin [86]), isoforms of the same protein from different species (human filamin and chicken filamin, [77]; chicken α-actinin and amoeba α-actinin, [87, 88]), and mutations of a single cross-linker (filamin [32], α-actinin [85]). Every study finds a wide disparity between different cross-linkers in identical preparations at identical concentrations. A single experiment demonstrated that filamin cross-linking resembles avidin-biotin cross-linking [74] leading some to conclude the cross-linker structure is not important. Due to the binding kinetics of different proteins, experiments comparing different proteins at the same concentrations might have different amounts of bound protein, affecting the number of cross-links.

In order to better understand the importance of cross-linkers, this thesis explores the effect of a ubiquitous cross-linker on the junction of two actin filaments, as described in Chapter 2.

Chapter 2 Actin and Filamin

The basic structural unit of the actin cytoskeleton is the junction of two actin filaments. Chapter 1 details the evidence demonstrating the effect of cross-linking on a solution of actin filaments, as well as the importance of cross-linking in developing a model that adequately describes the cytoskeleton *in vivo*. Chapter 2 expounds the properties of two primary constituents of the cytoskeleton, actin and filamin. The properties of actin are well-established in the literature; its mechanical properties are only briefly summarized here. Because filamin is present in all tissues, is expressed at high 1-5 μM concentrations, and is the most potent actin cross-linker in the human body, it is the focus of this thesis.

2.1 The biophysical properties of actin

Actin is a ubiquitous protein in eukaryotic cells, a 42 kDa globular protein (G-actin) about 5 nm in diameter that spontaneously polymerizes into polarized double-helical filaments (F-actin) in the presence of salts such as KCl and $MgCl_2$ [2]. The concentration of actin in cells is on the order of 200-500 μM [26], and approximately half of the actin is F-actin [26, 89] (the polymer fraction varies with cell state [90] to meet the needs of the cell). F-actin is approximately 9 nm in diameter [2] and has a persistence length of 15 μm [60] (a measure of how long a polymer must be before the motion of its ends in thermal fluctuation is uncorrelated). In cells, F-actin extends up to a micron in length [89, 91] and the "pore size" of the cytoskeleton is about 100 nm. At these lengths the actin is rigid [92], with only minor fluctuations due to thermal collisions of the aqueous buffer.

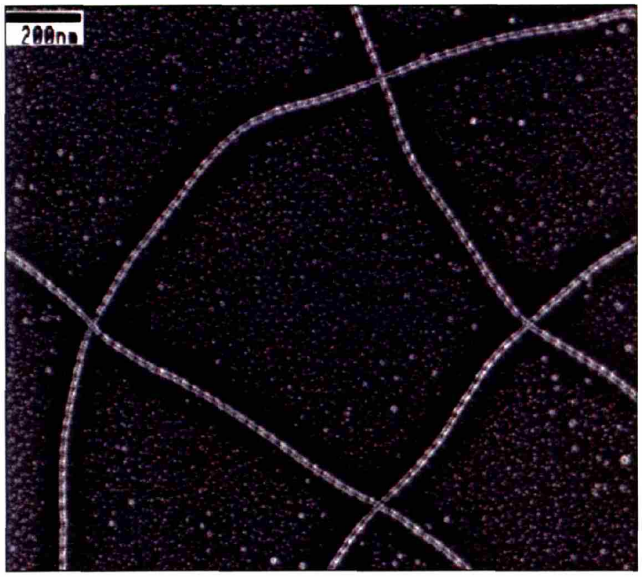

Figure 2.1 Electron micrograph of filamentous actin (F-actin) coated on freshly cleaved mica and low-angle rotary shadowed with platinum following the Mabuchi method (Section 3.9). The 36 nm helical periodicity is visible. This sample has been mixed with filamin and the orthogonality of junctions discussed below is apparent.

2.2 Filamin

Filamin is an actin-cross-linking protein ubiquitous in mammalian cells, composed of two strand-like subunits with length 80 nm, diameter 3-5 nm, and molecular weight 280 kDa [72]. Filamin subunits dimerize to form the roughly U- or V-shaped connection shown in Figure 2.2.

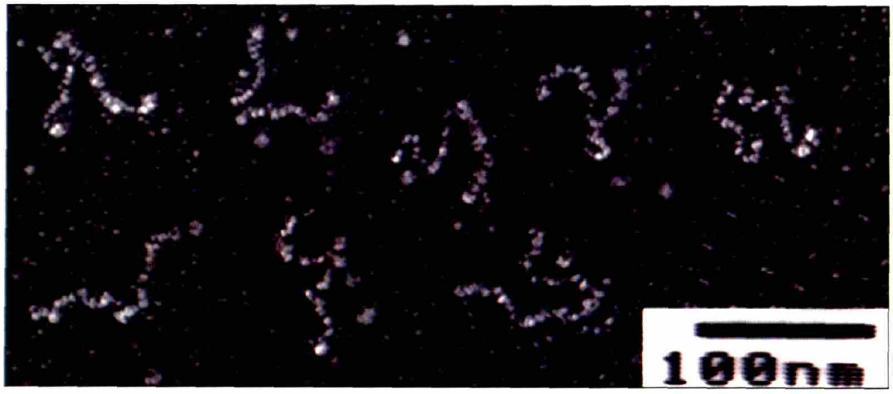

Figure 2.2 Electron micrograph of filamin molecules diluted in 50% glycerol, sprayed onto freshly cleaved mica, and low-angle rotary shadowed with platinum (Section 3.8).

Cells require filamin to function. As described in Chapter 1, cell lines that lack filamin lack motility and normal membrane appearance [78, 79]. Human embryos that do not express it die *in utero* [93]. While many of these effects can be traced to its actin cross-linking role, filamin differs from other actin cross-linkers in that it interacts with dozens of cellular proteins and therefore has multiple functions to supplement its role in cell mechanics. For example, filamin connects the cytoskeleton to the membrane by binding to the cytoplasmic domain of β-integrin to control cell adhesion and migration [94, 95]. Filamin binds to RalA to induce filopodia [96] and binds to glycoprotein-Ib-IX complex which induces platelet activation and aggregation [97]. Filamin binds to a number of transmembrane receptors, signaling molecules, growth factors, kinases, and phosphotases as reviewed in detail elsewhere [98, 99] and summarized in Table 2.1.

Table 2.1 Summary of filamin-binding proteins, their binding location, and significance.

Partner	**Binding site on filamin**	**Functional significance of the association**	**Reference**
GpIb/V/IX (Von Willebrand receptor) complex	Repeats 17-19 (FLNa, b)	Promotes cell spreading	[100]
β1A, β1D, β2, β3, β7 integrins	Carboxy-terminal half	Mechanoprotection	[95]
Tissue factor	Repeats 23-24	Regulates endothelial cell adhesion in embryonic vasculature	[101]
FcγR1 (CD64)	?	Tethers FcγR1 to cytoskeleton, sequestering it from endocytic pathway	[102]
Furin	Repeats 13-14	Directs furin from early endosomes to Golgi	[103]
δ-Sarcoglycan	Repeats 23-24 (FLNc)	Possible role in limb girdle muscular dystrophy	[104]
Myotilin	Repeats 19-21 (FLNc)	Possible role in limb girdle muscular dystrophy	[105]
Caveolin-1	Carboxy-terminal half	Organizes endocytosis and cholesterol transport molecules	[106]
Presenilins	Carboxyl terminus (FLNa, b, dmFLN1)	FLN1 overexpression inhibits presenilin overexpression phenotype in *Drosophila*	[107]
Dopamine D2, D3 receptors	Repeats 16-10	Participates in response to dopamine	[108]
Granzyme B	Repeat 24	Participates in granzyme-mediated apoptosis	[109]
Toll	Repeats 21-24 (dmFLN1)	Involved in inflammatory signal transduction pathways	[110]
TRAF2	Repeats 21-24	Involved in SAPK or NF-κB activation by TRAF2 or TNF	[111]
SEK-1	Repeats 21-24	Involved in response to SAPK-activators, lysophosphatidic acid, and TNF	[112]
Androgen receptor	Carboxyl terminus	Involved in translocation of androgen receptor to the nucleus	[113]

Table 2.1 Cont'd. Summary of filamin-binding proteins, their binding location, and significance.

Rho, Rac, Cdc42	Repeats 21-24	Organizes the formation of filopodia	[96]
Ral A	Repeat 24	Promotes the formation of microspikes downstream of Cdc42	[96]
Trio	Repeats 23-24	Promotes dorsal ruffling	[114]
cvHSP	Repeats 21-24	cvHSP acts as a chaperon protein	[115]
Kv4.2 potassium Channel	Carboxyl terminus	Promotes current density mediated by this specific channel	[116]
Kir2.1	Repeats 23-24	Organizes potassium channel molecules	[117]
BRCA2	Repeats 21-24	Regulates DNA sensitivity to radiation	[118]
Smad	Repeats 20-23	Regulates TGF-β mediated signaling	[119]
Calcium-sensing receptor	Repeats 15-16	Activates p42ERK and its activated MAP kinase pathway	[120]
Protein kinase Cα	Repeats 4-10	Phosphorylates filamin for signalling	[121]
FILIP	Repeats 15-17	Regulates cortical cell migration out of the ventricular zone	[122]
Migfilin	Repeat 21	Localizes Mig-2 to focal adhesions	[123]
Ribosomal S6 kinase (RSK)	Repeats 19-21	ERK targeting	[124]
SHIP-2	Repeats 22-23	Regulates PI3 kinase signaling	[125]
PAK 1	Repeats 21-23	Reorganizes cytoskeleton in response to external stimuli	[126]
N-RAP	?	Participates in sequential myofibril assembly	[127]
Insulin receptor	?	Alters insulin-dependent activation of MAP kinase pathway	[128]
Tc-mip	?	Involved in c-maf-dependent Th2 signaling pathway for cytoskeletal organization in glomerular disease	[129]
FAP52	Carboxy-terminal half	Involved in cytoskeletal organization at focal adhesions	[130]
Calmodulin	?	Participates in calcium dependent pathway for cytoskeletal organization	[131]
Actin	N-terminus	Cross-links actin into large-angle junctions	[132]

The discovery of filamin occurred serendipitously during efforts to isolate myosin from rabbit macrophages [132]. The protein was generically termed "actin-binding protein" (ABP) at the time because it was the first non-muscle actin-binding protein to aggregate actin extensively, and subsequent immunolabeling experiments confirmed the presence of ABP in cellular actin bundles. These discoveries were made in different cells (macrophages and fibroblasts) from different species (rabbit and chicken), giving an indication of the diversity of this protein. Further immunolabeling experiments confirmed that ABP, or proteins very similar to it, was present in a diverse range of vertebrate cells. Independent research in *Dictyostelium discoideum*, *Entamoeba histolytica*, and *Drosophila melanogaster* led to the discovery of proteins with similar structure and function, as well as to confusion about the relationships and identities of these proteins [133-135]. A recent review of the filamin family[98] proposes the nomenclature summarized in Table 2.2.

Table 2.2 A summary of the nomenclature of the filamin family, as proposed in [98].

Name	**Previous names**	**Distribution**
hsFLNa	αFLN, FLN1, ABP, ABP-280, non-muscle FLN	*Homo sapiens*, broadest distribution
hsFLNb	βFLN, FLN3, FH1	*Homo sapiens*, broad distribution
hsFLNc	γFLN, FLN2, ABP-L	*Homo sapiens*, predominantly muscle
ddFLN	ABP-120, gelation factor	*Dictyostelium discoideum*
ggFLNb	FLN	*Gallus gallus*, retinal epithelium
dmFLN1-20	FLN-240, FLN1	*Drosophila melanogaster*, ovarian ring canals
dmFLN1-9	FLN-90	*Drosophila melanogaster*, ovarian muscle sheath
dmFLN2		*Drosophila melanogaster*

Figure 2.3 shows the structure of human filamin, as discussed in detail in Section 2.3. The N-terminus contains the actin-binding domain (ABD) and the C-terminus contains the self-association site where two filamin monomers attach. Beyond the actin-binding domain, amino acids divide into 24 repeat regions, each approximately 96 residues long. Two irregularities interrupt the primary sequence of each subunit, between repeats 15/16 and between repeats 23/24. The current theory of filamin's structure speculates that these insertions serve as hinges between the rigid rod-like domains [136].

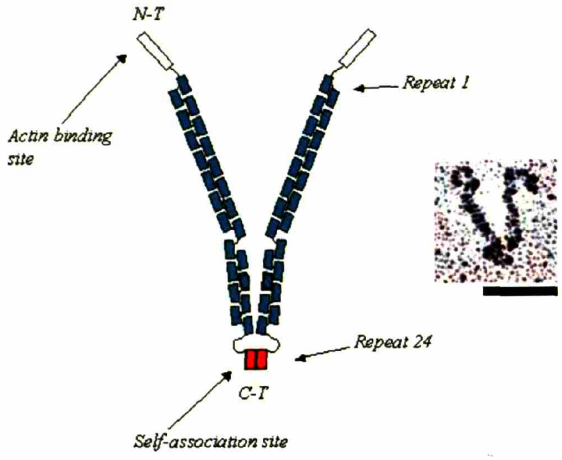

Figure 2.3 A model for filamin. Each mer is composed of two "rod-like" domains joined by a "hinge." Another hinge is found near the self-association site. Actin presumably binds at the N terminus. The inset photograph is a micrograph of filamin. Bar 60 nm.

As shown in Table 2.2, humans express three isoforms of filamin: A, B, and C. These three isoforms can be differentiated by their genes, by their tissue distribution, and by slight differences in their structure. The general repeat structure of the three filamin isoforms is identical, and the isoforms have 60-80% homology over the 24 repeats and 45% homology over the two hinges [137]. The importance of each of the three isoforms is clear from a number of human disorders that result from their deletion or mutation, as discussed following.

Filamin A is the most ubiquitous isoform in humans, distributed through all cells and organs. It is encoded in the gene FLNA located on the X chromosome at Xq28 [138]. Localized mutations in filamin A lead to such disorders as periventricular heterotopia [93, 139-141], otopalatodigital syndrome type 1 and type 2, frontometaphyseal dysplasia, and Melnik-Needles syndrome [142]. Repeat 15 of filamin A can contain an alternative splice of 8 amino acids. $FLNa_{var\text{-}1}$ has a deletion of 41 amino acids between repeats 19 and 20 and is expressed widely at low levels [137]. There is no known naturally occurring filamin A lacking either hinge.

Filamin B has a similar distribution to filamin A in humans, but at lower expression levels. It is encoded in the gene FLNB located on chromosome 3 at 3p14.3 [143]. Mutations in filamin B lead to disorders including spondylocarpotarsal syndrome, Larsen syndrome, and atelosteogenesis I and III [144]. FLNb(ΔH1) is a variant lacking hinge 1 and $FLNb_{var\text{-}1}$ has a deletion of 41 amino acids between repeats 19 and 20. Two variants, $FLNb_{var\text{-}2}$ and $FLNb_{var\text{-}3}$, found in cardiac tissue only, lack Repeats 21-24 which includes hinge 2 and the self-association site [137].

Filamin C is found primarily in cardiac and skeletal muscle, occurring rarely in other tissues [145]. An 81 amino acid insertion in repeat 20 differentiates filamin C from filamins A and B. Filamin C is encoded in the gene FLNC located on chromosome 7 at 7q32 [143]. FLNc(ΔH1) is a splice variant lacking hinge 1 and in fact, FLNc(ΔH1) is more prevalent than hinged FLNc [137].

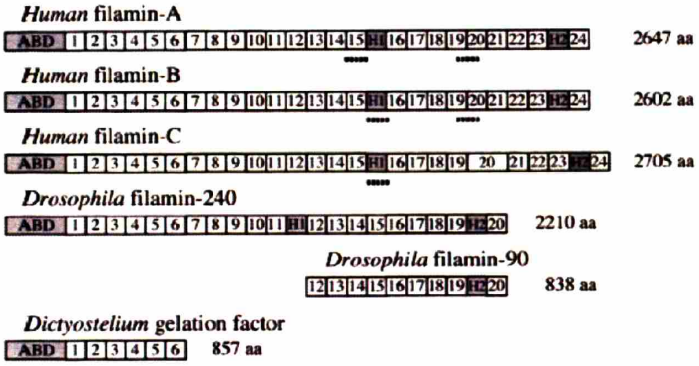

Figure 2.4 Three proteins constitute the human filamin family. The three have similar but distinct structure and function. Additionally, other species have related proteins. (Figure 2 from [137])

Due to its prevalence (platelets, for example, have tenfold more filamin A than filamin B and no filamin C[146]), filamin A is the chosen isoform for modeling the cytoskeleton, and for the remainder of this thesis the term "filamin" refers to filamin A unless otherwise stated.

2.3 The structure of filamin A

Early studies reported cleavage of filamin with a Ca^{2+} protease yields a heavy fragment and a light fragment, denoted heavy merofilamin (M_r = 240 kDa) and light merofilamin (M_r = 9.5 kDa) [147]. Heavy merofilamin binds to F-actin, but does not cross-link it, while light merofilamin neither binds nor cross-links F-actin. Because the molecule binds and cross-links actin when whole, the heavy fragment of filamin contains the actin-binding domain and the light fragment of filamin contains the self-association site.

When the amino acid sequence was determined, the fine details of the domains of filamin became clear [136]. Each filamin monomer is composed of 2,647 amino acids, listed in Figure 2.5. 275 amino acids at the N-terminus bind to actin, and the remaining amino acids form 24 immunoglobulin-like (Ig-like) repeats, each approximately 96 aa long. Comparison to the cleavage studies above reveals that heavy merofilamin contains the ABD and repeats 1-23 and light merofilamin is repeat 24.

```
N     1 mssshsragq saagaapggg vdtrdaempa tekdlaedap wkkiqqntft rwcnehlkcv  ABD
     61 skrianlqtd lsdglrlial levlsqkkmh rkhnqrptfr qmqlenvsva lefldresik
    121 lvsidskaiv dgnlklilgl iwtlilhysi smpmwdeeed eeakkqtpkq rllgwiqnkl
    181 pqlpitnfsr dwqsgralga lvdscapglc pdwdswdask pvtnareamq qaddwlgipq
    241 vitpeeivdp nvdehsvmty lsqfpkaklk pgaplrpkln pkkaraygpg ieptgnmvkk
    301 raeftvetrs agqgevlvyv edpaghqeea kvtanndknr tfsvwyvpev tgthkvtvlf  1
    361 agqhiakspf evyvdksqgd askvtaqgpg lepsgniank ttyfeiftag agtgevevvi  2
    421 qdpmgqkgtv epqleargds tyrcsyqptm egvhtvhvtf agvpiprspy tvtvgqacnp  3
    481 sacravgrgl qpkgvrvket adfkvytkga gsgelkvtvk gpkgeervkq kdlgdgvygf
    541 eyypmvpgty ivtitwggqn igrspfevkv gtecgnqkvr awgpgleggv vgksadfvve  4
    601 aigddvgtlg fsvegpsqak iecddkgdgs cdvrywpqea geyavhvlcn sedirlspfm
    661 adirdapqdf hpdrvkargp glektgvavn kpaeftvdak hggkaplrvq vqdnegcpve  5
    721 alvkdngngt yscsyvprkp vkhtamvswg gvsipnspfr vnvgagshpn kvkvygpgva  6
    781 ktglkahept yftvdcaeag qgdvsigikc apgvvgpaea didfdiirnd ndtftvkytp
    841 rgagsytimv lfadqatpts pirvkvepsh daskvkaegp glsrtgvelg kpthftvnak  7
    901 aagkgkldvq fsgltkgdav rdvdiidhhd ntytvkytpv qqgpvgvnvt yggdpipksp
    961 fsvavspsld lskikvsglg ekvdvgkdqe ftvkskgagg qgkvaskivg psgaavpckv  8
   1021 epglgadnsv vrflpreegp yevevtydgv pvpgspfple avaptkpskv kafgpglqgg  9
   1081 sagsparfti dtkgagtggl gltvegpcea qlecldngdg tcsvsyvpte pgdyninilf
   1141 adthipgspf kahvvpcfda skvkcsgpgl eratagevgq fqvdcssags aeltieicse  10
   1201 aglpaevyiq dhgdgthtit yiplcpgayt vtikyggqpv pnfpsklqve pavdtsgvqc  11
   1261 ygpgiegqgv freattefsv daraltqtgg phvkarvanp sgnltetyvq drgdgmykve
   1321 ytpyeeglhs vdvtydgspv psspfqvpvt egcdpsrvrv hgpgiqsgtt nkpnkftvet  12
   1381 rgagtgglgl avegpseakm scmdnkdgsc sveyipyeag tyslnvtygg hqvpgspfkv
   1441 pvhdvtdask vkcsgpglsp gmvranlpqs fqvdtskagv aplqvkvqgp kglvepvdvv  13
   1501 dnadgtqtvn yvpsregpys isvlygdeev prspfkvkvl pthdaskvka sgpglnttgv  14
   1561 paslpvefti dakdagegll avqitdpegk pkkthiqdnh dgtytvayvp dvtgrytili
   1621 kyggdeipfs pyrvravptg daskctvtvs igghglgagi gptiqigeet vitvdtkaag  15
   1681 kgkvtctvct pdgsevdvdv venedgtfdi fytapqpgky vicvrfggeh vpnspfqvta
   1741 lagdqpsvqp plrsqqlapq ytyaqgggqt waperplvgv ngldvtslrp fdlvipftik  16
   1801 kgeitgevrm psgkvaqpti tdnkdgtvtv ryapseaglh emdirydnmh ipgsplqfyv
   1861 dyvncghvta ygpglthgvv nkpatftvnt kdagegglsl aiegpskaei sctdnqdgtc  17
   1921 svsylpvlpg dysilvkyne qhvpgspfta rvtgddsmrm shlkvgsaad ipinisetdl  18
   1981 slltatvvpp sgreepcllk rlrnghvgis fvpketgehl vhvkkngqhv asspipvvis  19
   2041 qseigdasrv rvsgqglheg htfepaefii dtrdagyggl slsiegpskv dintedledg
   2101 tcrvtycpte pgnyiinikf adqhvpgspf svkvtgegrv kesitrrrra psvanvgshc  20
   2161 dlslkipeis iqdmtaqvts psgktheaei vegenhtyci rfvpaemgth tvsvkykgqh
   2221 vpgspfqftv gplgeggahk vraggpgler aeagvpaefs iwtreagagg laiavegpsk  21
   2281 aeisfedrkd gscgvayvvq epgdyevsvk fneehipdsp fvvpvaspsg darrltvssl  22
   2341 qesglkvnqp asfavslnga kgaidakvhs psgaleecyv teidqdkyav rfiprengvy
   2401 lidvkfngth ipgspfkirv gepghggdpg lvsaygagle ggvtgnpaef vvntsnagag  23
   2461 alsvtidgps kvkmdcqecp egyrvtytpm apgsylisik yggpyhiggs pfkakvtgpr
   2521 lvsnhslhet ssvfvdsltk atcapqhgap gpgpadaskv vakglglska yvgqkssftv  24
   2581 dcskagnnml lvgvhgprtp ceeilvkhvg srlysvsyll kdkgeytlvv kwgdehipgs
   2641 pyrvvvp
C
```

Figure 2.5 The complete amino acid sequence of filamin A, starting at the N-terminus. The residues are divided into 24 repeats, alternating in blue and green and numbered on the right of the chart. The 275 aa Actin Binding Domain and the hinge insertions are colored red. The 65 aa self-association site within repeat 24 is bold.

Actin-binding domain

The N-terminal 275 aa actin-binding domain (ABD) is "α-actinin-like" and conserved across multiple families of cytoskeletal proteins [148, 149]. α-actinin-like ABDs are composed of two 110 aa calponin homology (CH) domains: CH1 and CH2 [150], as shown in Figure 2.6.

Analysis of deletions and point mutations combined with peptide binding studies of various α-actinin-like ABD family members has led to the identification of three potential actin-binding sites (ABS1, 2 and 3). Most of the available data suggest that a conserved hydrophobic region (ABS2), corresponding to the last α-helix of the CH1 domain, is crucial for binding. This region consists of amino acids 121-147 of filamin, or the homologous residues in α-actinin or gelation factor, residues 108-134 and 89-115, respectively [151-153]. The first α-helix of the CH2 domain (ABS3) contributes to actin binding in such a way that the CH1 and CH2 domains in concert bind to F-actin with a higher affinity than the CH1 domain alone. Filamin binds all actin isoforms and the binding sites on actin reside at residues 105-120 and 360-372 in actin subdomain-1 [154].

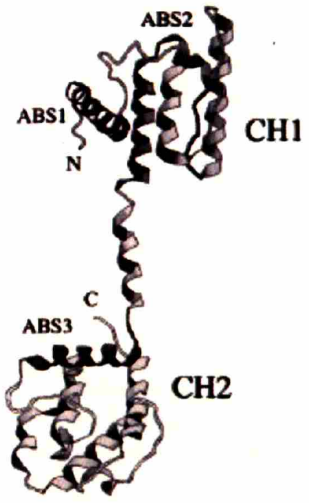

Figure 2.6 The actin binding domain of dystrophin. Indicated are the two calponin homology domains (CH1 and CH2) and the three actin-binding sites (ABS1, 2 and 3). The structure was taken from the Protein Database and the ribbon drawing was generated using MolView1.5. (Figure 1a from [137])

The fact that filamin truncated by the first 254 aa does not cross-link actin [155] demonstrates that the ABD is necessary for actin-binding. However, there is no indication whether it is sufficient or if there are additional secondary binding sites.

Cosedimentation studies of filamin and actin indicate that the maximum bound molar ratio is 1:10 [71-73]. Filamin may bind to several adjacent actin monomers, or it may sterically interfere with other filamin molecules binding F-actin near its attachment.

Filamin competes with myosin [156, 157], tropomyosin [158, 159], and caldesmon [160], but may not compete with α-actinin [158, 161]. Filamin likely binds the helical groove of an actin filament as evidenced by binding competition with tropomysosin as well as optical diffraction analysis of the bound structure. Differences in the binding characteristics of these actin-binding proteins could be due to amino acid substitutions, variations in the relative orientation of two CH domains, or differences in intermolecular interactions. Variations observed in the relative orientation of the individual CH domains within the ABDs suggest a mechanism in which both the ABD and actin undergo structural rearrangements upon binding to each other [162, 163].

While the binding strength of filamin to actin has not been measured, proteins with similar CH actin-binding domains have been studied. The force required to break the bond between actin and α-actinin, for example, was measured with an optical trapping technique [164]. The unbinding force averages 18 pN, with a wide range from 1.4 to 44 pN. The unbinding time is classifiable into two major groups: one group having a time value of 1 sec or less and the other having a time value ranging from several to 20 seconds. This suggests the existence of at least two classes of the α-actinin bonds. Single myosin events can be measured at ionic strengths that disrupt weak binding actomyosin interactions [165], further supporting the postulate of distinct weak and strong binding states of single proteins.

The affinity of filamin for F-actin is of the same order as that of α-actinin. The dissociation equilibrium constant chicken α-actinin is 0.6 μM [87, 166], filamin is 1 μM [136] and amoeba α-actinin is 5 μM [87].

Repeats

Filamin's repeats are β-sheet secondary structures interspersed with turns [136], as illustrated in Figure 2.7. Repeats 1-15 have intrachain hydrophobic interactions that may affect monomer stiffness. Even-numbered repeats beyond the first hinge (16, 18, 20, 22, 24) diverge slightly from the consensus repeat [136].

Figure 2.7 Repeat 4 of ddFLN. The structure was taken from the Protein Database and the ribbon drawing was generated using MolView1.5. (Figure 1B from [137])

The strength of the repeats has been measured with atomic force microscopy [167]. When filamin is pulled between a probe and a substrate, the individual repeats are drawn out. As shown in Figure 2.8, the unfolding force ranges from 50 to 220 pN. The contour length stretch per unfolding event is 31 nm, giving the molecule an approximate Hookean stiffness of 2-5 pN/nm. Point mutations affect the mechanical stability of Ig-like repeats significantly [168] so it is not surprising that each Ig-like domain of filamin has a unique unfolding strength due to distinct amino acid composition.

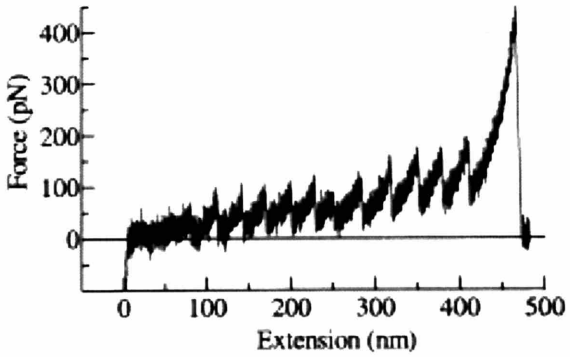

Figure 2.8 A force-extension curve of filamin A molecule in aqueous solution measured by AFM at room temperature. Filamin A was stretched at a pulling speed of 0.37 μm/s. (Figure 1a from [167])

The six-repeat *Dictyostelium* analog of filamin has also been studied in this manner [169]. In this molecule, the contour length change per unfolded repeat is also 31 nm and the force for unfolding is on the order of 50-100 pN. At 200 pN the system yields, so either that represents the self-association strength or that represents the molecule detaching from its substrates. Titin, a 3000 kDa actin-binding protein with similar repeat structure to filamin, has been reported to unfold at 30 pN, 100 pN, or 250 pN [170-172], similar to the range for filamin. Spectrin, on the other hand, reversibly unfolds at lower forces, 25 to 35 pN [173]. Spectrin, α-actinin, and fodrin repeats fold into triple helical coiled-coils, whereas filamin and titin repeats are Ig-like β-barrels [174].

Hinges

Before repeat 16 there is a 24 residue sequence that interrupts the pattern of β-sheets; before repeat 24 there is a 33 residue interruption [136]. The original report of this sequence speculated that these interruptions were "hinges." The interruptions have a biochemical purpose as targets for protease cleavage, but recent rheological experiments comparing networks with filamin to those with filamin lacking hinge 1 suggest that the hinge serves a mechanical purpose stiffening cells [32].

Self-association domain

Repeat 24 represents the C-terminus of the molecule. Electron micrographs show this end of the molecule is the self-association section of the dimer. At high ionic strength (0.6 M KCl), 80-90% of the total filamin population reversibly alternates between monomers and dimers, while the remainder form irreversible tetramer structures [175]. In physiological conditions (0.1 M NaCl) nearly all filamin molecules form dimers [176].

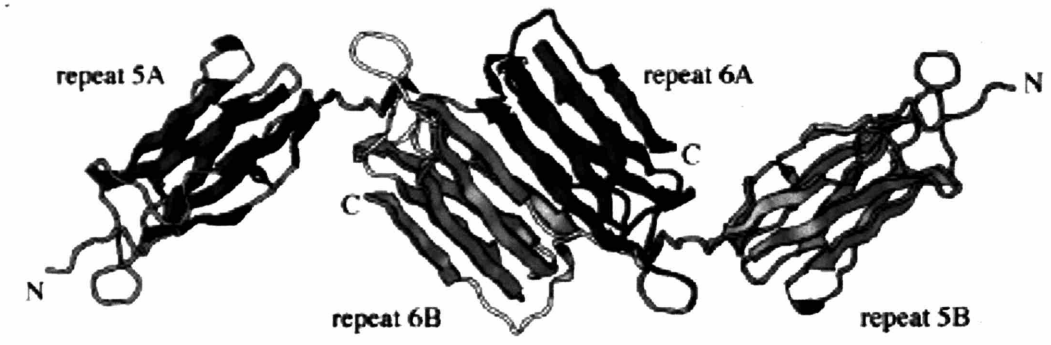

Figure 2.9 Repeats 5 and 6 of two molecules of ddFLN. Dimerization is mediated by the carboxy-terminal filamin repeat 6. The structure was taken from the Protein Database and the ribbon drawing was generated using MolView1.5. (Figure 1C from [137])

The angular stiffness of the filamin dimer is calculated for the first time in this thesis. F-actin junctions presumed cross-linked by a different actin-binding protein, Arp2/3, were observed fluctuating in time and the stiffness of Arp2/3 was determined to be 10^{-19} J/rad^2 [177]. In personal communication, the authors indicated that there were no corrections for three dimensional effects or attachment to glass.

2.4 The efficacy of filamin A: a hypothesis on binding mechanism

Filamin's structure is ideal for an actin-binding protein. The first requirement for cross-linking is the ability bind to multiple actin filaments. While each subunit only has one binding domain, dimerization provides multi-valency.

The large size of filamin also aids cross-linking. With binding domains separated by 150 nm of protein chain, filamin's reach is great and it has the ability to sample a large volume of space. The probability of two actin filaments coming close enough to be bound simultaneously by a short cross-linker is much smaller, especially considering hydrodynamic interference between the actin filaments.

Filamin's binding efficacy is demonstrated by its low gel point, 10^{-8} M in 20 μM F-actin[77]. One molecule of filamin per 6 μm of F-actin is sufficient to transform an entangled actin network into a cohesive gel with pore size 2 μm. *In vivo*, the filamin:actin molar ratio is 1:10, far exceeding the gel point, and the pore size is only 100-200 nm [26, 178].

The mechanism by which filamin cross-links actin is unknown. The simplest model for any cross-link is a tether. In this case, filamin merely constrains the motion of F-actin. While this seems simplistic, rheologically a tether has a tremendous impact on the stiffness of an entangled polymer network. Coupling the motion of the elements dissipates energy and reduces entropy constraints.

However, two lines of experiments contradict the tether hypothesis for filamin. As discussed at length in Section 1.3, there is wide disparity among the efficacy of cross-linkers, even between the same protein with a slight mutation. If filamin serves as a tether, a deletion of 20 amino acids (less than 1% of the aa sequence) from the middle of the molecule should have little effect on network stiffness, yet it alters the stiffness considerably [32].

Second, it has been observed that filamin consistently cross-links F-actin into large-angle junctions when compared to uncross-linked F-actin [179]. This implies some structural role for the cross-linker. If filamin was a tether, there should be no preferential angle for junctions it regulates.

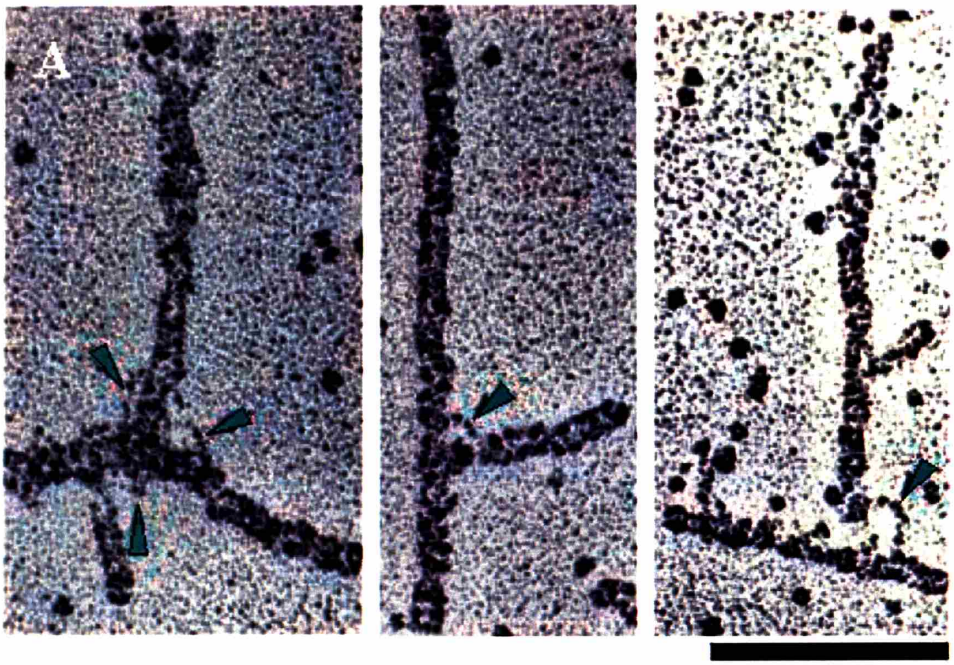

Figure 2.10 Micrographs of orthogonal actin filament junctions with possible binding proteins highlighted by arrowheads. Bar 200 nm. (Figure from [179])

The current model of filamin cannot explain large angles. Filamin reportedly has two actin-binding domains separated by four rod-like domains, each connected by flexible hinges (Figure 2.3). A serial assemblage of components is only as strong or stiff as its weakest member, and a molecule with so many flexible hinges could not be anything but a tether, barring a massive reorganization of the molecule upon binding.

This thesis proposes a model for filamin that provides a mechanism for large-angle, high-efficacy actin cross-linking. The model is predicated on the following hypotheses:

1. The structure of filamin is not truly "rod-like" but rather flexible.

2. Filamin is not uniformly flexible, but rather has a flexible region near the amino terminus and a stiff region near the carboxy terminus. The long, flexible arms enable filamin to ensnare actin quickly.

3. Filamin binds its entire length along F-actin such that the stiff region can impart structure to the actin junction in spite of the flexible arms.

To evaluate filamin's role in network architecture and cytoskeletal mechanics, two key pieces of information are needed:

1. The three-dimensional geometry of filamin-actin junctions must be established. The foundational paper cited for the orthogonality of filamin-regulated junctions has a couple caveats. One, the actin junctions are sprayed onto mica, dried, and shadowed. It is unclear how accurately these junctions resemble *in vivo* junctions in three-dimensional space. Two, the junctions are not labeled for filamin. While compiling statistics for large numbers of junctions is a reasonable approach, there is no certainty how many, if any, junctions actually have filamin. The filamin may have aggregated the majority of the actin and left only unregulated short F-actin segments, for example. Only by labeling filamin can there be certainty that the right junctions are being measured. Measuring junction angles in three dimensions from a two-dimensional image may seem impossible, but the technique is described in the next chapter.

2. The orientation of filamin at cross-links must be determined. If filamin binds along actin filaments, it may serve as a brace strengthening the junction. If filamin binds as a tether, the distance between cross-linked actin filaments could be greater than the pore-size. The dynamics of the junction in these two scenarios is different, and determining which is correct will illuminate junction, and network, stiffness. Observing the thin filamin molecule *in situ* in an actin network is challenging, and a novel labeling approach is described next.

Chapter 3 Experimental Methods

3.1 Experimental design

The question of how to best gold-label filamin *in situ* is a challenging one which consumed this project for a number of years. Immunogold labeling is most often used to determine protein spatial distribution in cells or to determine whether a protein has been expressed. As such, heavy labeling is best, and high concentrations of polyclonal antibodies can be used. To determine a protein's structure, more precision is needed. To achieve this goal, cell cytoskeletons are labeled with a cocktail of monoclonal anti-filamin antibodies with known epitopes, as shown in Figure 3.1. These primary antibodies are then labeled with secondary anti-mouse antibodies conjugated to 10 nm gold spheres. This produces a trace of filamin, and the appropriate pattern of gold-labeling can analyzed.

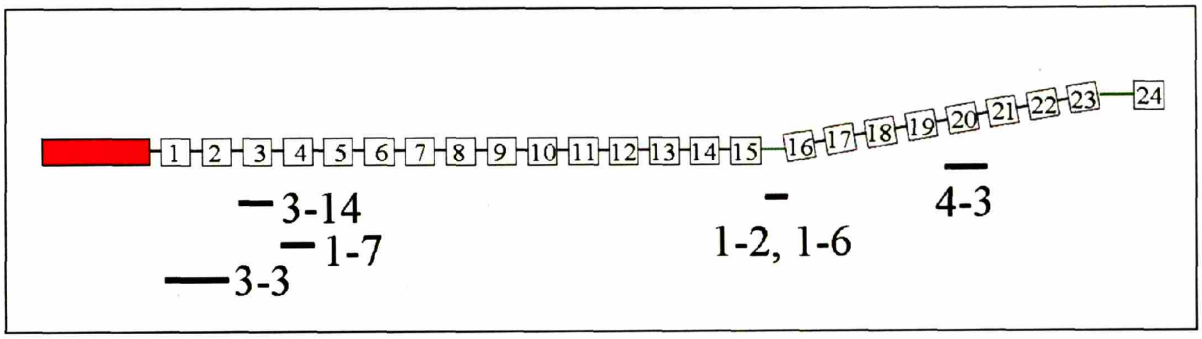

Figure 3.1 The epitopes for the six anti-filamin monoclonals used to trace filamin contours at actin junctions. The red domain is the actin-binding domain at the N-terminus of filamin, and the 24 repeats are numbered.

Many other techniques were used to varying degrees of success. Filamin was biotinylated and labeled with streptavidin-conjugated gold or anti-biotin-conjugated gold, a GpIb peptide was used as a marker for Repeat 17, 1.4 nm Nanogold was conjugated to filamin and to the GpIb peptide, 1.8 nm Nanogold conjugated to nickel was used to bind His-FLN, immunogold conjugated to proteins A or G was used as secondary markers, several mutants of filamin with different advantages were tested (Figure 3.2), and monoclonal anti-filamin antibodies were directly conjugated to gold. However, none of these methods produced satisfactory results.

The method was used to label A7 cells – melanoma cells with filamin – in order to provide a control system without filamin (M2 cells). Cell cytoskeletons are more robust than purified actin networks and survive EM preparation better. Table 3.1 provides a summary of the various techniques investigated before settling on the final preparation, which is described in detail following.

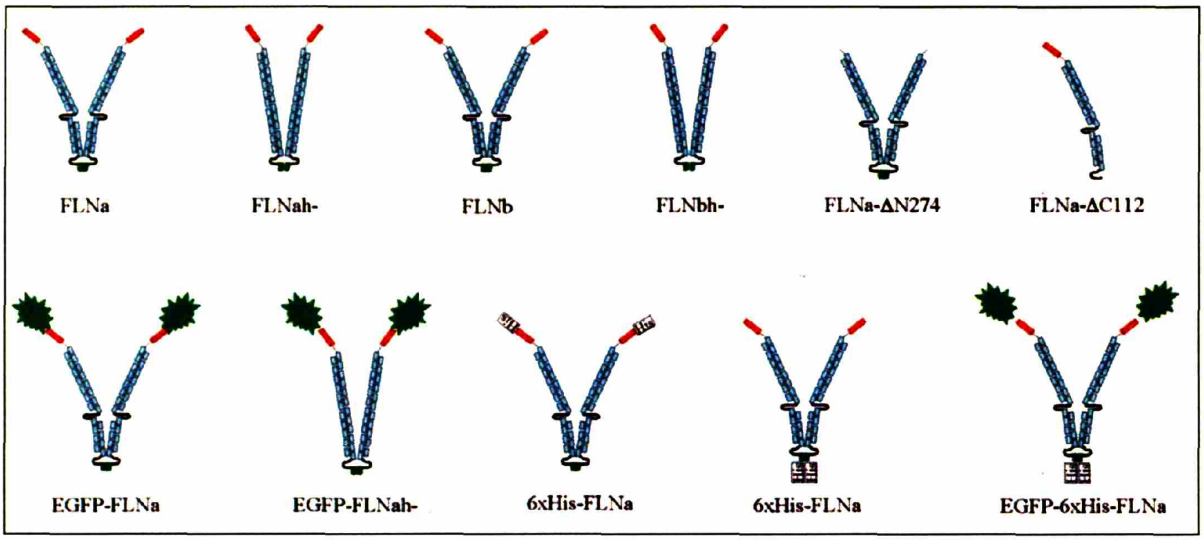

Figure 3.2 Several of the mutant forms of filamin tested in this thesis. Because all the anti-filamin antibodies are from mice, the bottom row of EGFP and 6xHis tagged filamin molecules offer an alternate target site for primary antibodies of alternate species. This enables the use of different anti-species secondary antibodies, which can be bound to different sizes of gold.

Table 3.1 Methods that were attempted in order to generate a gold-particle trace of filamin bound to two F-actin filaments. The check marks indicate that the antibodies were tested in that manner, not that the tests were successful.

		Gold labeling					
		Primary	Anti-species	Protein A	Protein G		
ANTIBODIES	mAb1	√	√			**NANO·AU**	nanogold-GpIb
	mAb2	√	√				nanogold-FLN
	mAb3	√	√				nanogold-nickel
	mAb4	√	√				
	mAb5	√	√			**ENHANCE**	GoldEnhance
	mAb6	√	√				gold chloride
	Chemicon	√	√				
	Glogauer	√	√				
						CELLS	human platelets
	Fumi 1.10	√	√				M2
	Fumi 1.2	√	√	√	√		M2-His-FLN
	Fumi 1.6	√	√	√	√		M2-EGFP-FLN
	Fumi 1.7		√	√	√		M2-EGFP-His-FLN

Table 3.1 Cont'd. Methods that were attempted in order to generate a gold-particle trace of filamin bound to two F-actin filaments. The check marks indicate that the antibodies were tested in that manner, not that the tests were successful.

		Primary	Gold labeling Anti-species	Protein A	Protein G		
	Fumi 3.14	√	√	√	√	**CELLS**	A7
	Fumi 3.3	√	√	√	√		A7-His-FLN
	Fumi 4.3	√	√	√	√		A7-EGFP-FLN
	Fumi 4.4		√				A7-EGFP-His-FLN
	Fumi 7.5		√				
						BLOCK/	BSA
	anti-His 1		√			**WASH**	tween
	anti-His 2		√				serum
	anti-His 3		√				milk
	anti-His 4		√				gelatin
							n-ethylmaleimide
	anti-GFP		√				imidazole
							sodium
	GpIb	√				**QUENCH**	borohydride
	GST-GpIb	√					ammonium chloride
							glycine
		Streptavidin	Anti-biotin				
	biotin 1	√	√			**BUFFER**	PBS
	biotin 2	√	√				Tris-NaCl
							Buffer B
FILAMIN	FLNa						
	FLNaH1-					**pH**	6
	FLNaΔN						7.4
	FLNaΔC						7.6
	FLNa-His						8.2
	FLNa-EGFP						
	FLNb					**FIX**	none
	FLNbH1-						4% formaldehyde
							1% glutaraldehyde
							4% FA/.05% GA
							4% FA/0.1% GA
							0.1% GA

3.2 Protein preparation

Actin was purified from rabbit muscle as described previously [180], frozen in liquid nitrogen at a concentration of 110 μM (~5 mg/ml), and stored at -80 °C. At least 12 hours before experiments, the actin was thawed, diluted in buffer A (2 mM HEPES, 0.5 mM ATP, 0.5 mM DTT, 0.5 mM $CaCl_2$, microfiltered, pH 7.4), kept overnight on ice, and then centrifuged at 300,000 × *g* for 40 min at 4 °C to remove aggregates. After the absorbance of the supernatant was measured at 280 nm to determine concentration, the supernatant was further diluted in buffer A at a final concentration of 50 μM and stored in the depolymerized form at 4 °C.

Recombinant FLNa was purified from Sf9 cell lysates by several chromatographic steps performed at 4 °C. During each step, fractions containing recombinant FLNa protein were identified by immunoblotting with polyclonal antibodies against the hinge 1 region of FLNa or by Coomassie Brilliant Blue staining. Either freshly prepared or thawed cell lysates were centrifuged at 20,000×*g* at 4 °C and the supernatant fluid was loaded onto a HiTrap Q column (three connections of 5-ml columns) pre-equilibrated with buffer solution QA8.5 (10 mM Tris-HCl, pH 8.5, 1 mM EDTA, 1 mM EGTA, 5 mM 2-mercaptoethanol, 0.02% Triton X-100). The column was washed with 50 ml of QA8.5 solution containing 200 mM NaCl and eluted with a 300-ml linear gradient of 200–400 mM NaCl in the equilibrating buffer at a flow rate of 4 ml/min. Fractions containing recombinant FLNa (eluting around 300 mM NaCl) were pooled and diluted 1:2 with QA8.5 solution containing the protease inhibitor mixture. Proteins in the pooled fractions were absorbed again onto a Hi- Trap Q column (three connections of 5-ml columns), and the column was washed with QA6.5 solution (10 mM PIPES-NaOH, pH 6.5, 1 mM EDTA, 1 mM EGTA, 5 mM 2-mercaptoethanol, 0.02% Triton X-100) containing 100 mM NaCl. Recombinant FLNa was eluted with a linear salt gradient (300 ml) from 100 to 400 mM NaCl in buffer QA6.5 at a flow rate of 4 ml/min. Fractions containing FLNa (eluting around 200 mM NaCl) were pooled and concentrated using Ultrafree-15 (Biomax-50K). FLNa was further purified by Superose 6 column chromatography with S6 solution (10 mM Tris-HCl, pH 7.4, 120 mM NaCl, 0.5 mM EGTA, 1 mM dithiothreitol). Isolated FLNa was concentrated using Ultrafree-15, frozen in liquid nitrogen, and stored at -80°C.

To generate monoclonal antibodies, approximately 15-20 μg of purified recombinant FLNa dissolved in PBS were mixed with complete Freund adjuvant and injected intraperitoneally to female BALB/c mice. Three boost injections with the same amount of antigen in incomplete adjuvant were given in 2-wk intervals. Ten days after the last boost, the sera of the immunized mice were tested by enzyme-linked immunosorbent assay (ELISA) and immunoblotting to detect antibodies against hsFLNa proteins. The mouse that gave the strongest response received an intravenous injection of antigen in PBS without adjuvant. Three days after the last injection, the spleen of the immunized mouse was macerated, and the spleen cells were fused with mouse myeloma Sp20 cells in the presence of Hybrimax poly-ethylene-glycol solution. The fused cells were plated onto 96-well plates and cultured in Optimum medium. The standard hypoxanthine-aminopterin-thymidine (HAT) selection procedure was applied to select the hybridoma clones

[181]. After 10 days, hybridoma supernatants were tested for reactivity with full-length and various deletion mutant of FLNa by ELISA to narrow epitope down and with recombinant FLNb to exclude antibodies that cross react FLNb. To further select antibodies, the media were tested by immunoblotting and immunostaining. Cells from the positive wells were cloned at least three times by limiting dilution and adapted to serum-free media, Hybridoma-SFM. The antibody subtypes were determined using a kit. Monoclonal IgG or IgM antibodies were purified from hybridoma supernatant by the methods shown in Table 3.2.

Table 3.2 Confirmation of the functionality of the anti-filamin monoclonal antibodies using a variety of techniques. + indicates positive signal, - indicates negative signal.

mAb	Isotype	Purification	EM (A7)	EM (M2)	IF (A7)	WB (FLNa)	WB (A7)	WB (FLNb)	ELISA (FLNa)
1-2	IgG2b	Protein A	+	-	+	+	+	-	+
1-6	IgG2a	Protein A	+	-	+	+	+	-	+
1-7	IgG1	Protein L	+	-	+	+	+	-	+
3-14	IgG1	GammaG	+	-	+	+	+	-	+
3-3	IgM	CAPTIV-M	+	-	+	weak	weak	-	+
4-3	IgG1	GammaG	+	-	+	+	+	-	+

3.3 Cell preparation

A7 cells are filamin-lacking M2 human melanoma cells that have been rescued with filamin cDNA. They are cultured in Dulbecco's Modified Eagle Medium, containing 8% Newborn Calf Serum/ 2% Fetal Calf Serum, 1% penicillin-streptococcus, 10 mM HEPES, and 0.15% sodium bicarbonate, augmented with 0.5 mg/ml G418 antibiotic to select for cells that have been rescued. M2 cells are cultured in the same media without G418.

Cells are incubated in 10 ml of media for 48 hours or until confluent. They are washed twice in PBS and detached with tryspin. After 5 minutes, the free cells are diluted in media and collected by centrifugation. The cell pellet is suspended in buffer in Petri dishes containing glow-discharged 5 mm glass coverslips and allowed to incubate at 37°C until the cells spread to 50% confluence.

In order to prepare cells for electron microscopy, the membranes are stripped and the cytoskeletons fixed. Cell-coated 5 mm coverslips are washed twice in PHEM buffer and incubated for 5 minutes in PHEM buffer containing 0.75% Triton-X to permeabilize lipid membranes, containing phalloidin, protease inhibitors, and 0.36% formaldehyde to protect the cytoskeleton. Without intermediate washing, the permeabilization buffer is removed and coverslips are incubated for ten minutes in PHEM buffer containing 3.6% formaldehyde. Because formaldehyde is used for fixation, all subsequent buffers contain 2 μM phalloidin to stabilize the actin filaments. After fixation, the cells and coverslips are blocked for at least 2 hours with PBS (pH 7.6) containing 1% BSA to prevent non-specific binding of protein labels.

3.4 Antibody labeling

After blocking, samples are incubated with 10 µl of monoclonal antibody diluted to 10 µg/ml, for 2 hours at 37°C. The incubation is followed by three washes of blocking buffer to remove unbound antibody. Incubation with a secondary anti-mouse gold-conjugated antibody for 2 hours at 37°C provides the label.

After the final antibody incubation, the coverslips are washed three times in blocking buffer to remove unbound secondary, and five times in PBS to remove BSA before fixation. After the coverslips are post-fixed by immersion in 1% glutaraldehyde in deionized, microfiltered water for 10 minutes, they are washed three times with distilled, deionized, microfiltered water and stored in the same at 4°C until they are freeze-fractured.

3.5 Freeze-fracturing

A metal tab with a 3 mm × 3 mm square of 1% agar is mounted on a spring-loaded stage and serves as the coverslip support.

A copper block with a thin layer of polished gold is placed over a spout of liquid helium and cooled to -220°C. When the block is cold, a coverslip containing labeled, fixed calls is removed from water and placed on the agar square. An extra drop of water is added to the sample to prevent evaporation and is removed immediately prior to freezing.

The spring-loaded stage with the coverslip is mounted upside-down on an arm 18 inches above the block, and dropped on the cold gold surface, simultaneously freezing the sample and bonding the coverslip to the agar. The sample tab with the frozen cell-coated coverslip is removed from the stage and quickly placed in liquid nitrogen.

(a detailed, illustrated protocol for EM preparation is available in the Appendix)

3.6 Metal coating samples

While submerged in liquid nitrogen, four metal tabs with their coverslips are mounted onto a + shaped copper stage. The stage is quickly inserted into a Cressington 308R vacuum evaporating chamber and warmed to -90°C to dry for an hour.

When the sample is dry and the vacuum has returned to full strength, the sample is shadowed with metal. For cells on coverslips, 1-2 nm of platinum or tantalum are applied at a 45° angle to the rotating sample (rotary shadowing). For bare molecules on mica, the metals are applied at a 5° angle to the rotating sample (low angle rotary shadowing). For both sample types, 5-10 nm of carbon are applied from 90° overhead to strengthen the metal replica.

The sample is removed from the chamber and allowed to thaw.

(a detailed, illustrated protocol for EM preparation is available in the Appendix)

3.7 Mounting replicas on grids

For samples on glass coverslips, the metal replicas are floated off on 24% hydrofluoric acid that contains a trace of Photo-Flo to disrupt surface tension. A glass wand is used to immediately transfer each replica to a waiting water dish treated with Photo-Flo. After three water baths, the replica is picked up on a copper grid (Ted Pella) that has a thin layer of formvar under a thinner layer of carbon, and the grid is viewed with a JEOL JEM-1200EX electron microscope at 100 kV.

For samples on freshly-cleaved mica, the replica is floated off in untreated Milli-Q water and picked up on carbon-coated formvar-copper grids. The grids are viewed with a JEOL JEM-1200EX electron microscope at 80 kV.

(a detailed, illustrated protocol for EM preparation is available in the Appendix)

3.8 Glycerol spraying onto mica

The ideal concentration of protein for this technique is 5-10 μg/ml, suspended in a buffer with 50% glycerol. 100% glycerol is difficult to measure and manipulate, so in practice stocks of glycerol are prepared at weaker concentrations in water, from 67-95%, and then diluted accordingly with buffer and protein for a final concentration near 50%.

When spraying filamin alone, 1 μl of 3.6 μM filamin is diluted in 49 μl of PBS, vortexed, mixed with 50 μl of 93% glycerol, and vortexed again. When spraying filamin and actin together, 7 μl of 40 μM actin is diluted in 43 μl of Buffer B containing 3 μl of 3.6 μM filamin and 0.5 μl of 1 mM phallacidin. This yields a final concentration of 6 μM actin, 0.1 μM filamin for a 1:100 molar ratio with actin, and 10 μM phallacidin for a 1:1 molar ratio with actin. After 1 hour at room temperature, the sample is diluted in 50 μl of 93% glycerol for a final concentration.

The 50% glycerol protein solution is sprayed onto freshly cleaved mica as described previously [182].

The mica sample is metal coated as described in Section 3.6 and mounted on grids and viewed as described in Section 3.7.

3.9 Mabuchi shadowing

Another method for the direct visualization of molecules combines the methods of uranyl staining, glycerol drying, and rotary shadowing [183]. Proteins are diluted to nanomolar concentration in a buffer of 0.1 M ammonium acetate, 0.5 mM $MgCl_2$, and 30% glycerol. A piece of freshly cleaved mica is floated on the protein solution for 45 seconds, then three drops of buffer, three drops of 2% uranyl acetate in 30% glycerol, pH 6, for 45 seconds, and three drops of buffer. The mica is placed against another piece of mica, sandwiched between pieces of filter paper, and pressed together to remove excess buffer. The mica is dried in a vacuum chamber and the protein is low-angle rotary-shadowed with 1 nm of platinum and coated with 8 nm of carbon.

The replicas are picked up on uncoated 200 mesh copper grids and observed in a JEOL 1200EX transmission electron microscope at 60 kV.

3.10 Image Processing

Quantification of protein contours is performed with MATLAB. The contours are traced using the GETLINE routine by clicking points along each molecule from one N terminus to the second. Because the points are joined by straight lines, the distances between clicked points are kept small.

Trace points are processed by MATLAB:

1. Contour length, L_c, is calculated by adding the segments for each molecule.
2. End-to-end distance, R, is calculated as the straight-line distance between the end points of the trace.
3. Radius of gyration, R_g, is calculated from the end-to-end measurements as
$$R_g^2 = < R^2 > / 6$$
4. Persistence length, L_p, is calculated from the end-to-end measurements as
$$L_p = < R^2 > /(2L_c)$$

Chapter 4 Computerized Reconstruction of 3-D Networks

Difficulty in determining three-dimensional information is the chief obstacle in meaningful cytoskeletal structural analysis. Angles, lengths, and even qualitative visual patterns all depend on a full three dimensional representation of the entangled, cross-linked network. Given a two-dimensional picture of a network, there is no way to differentiate the infinite number of structures that would project this same image.

Computerized three-dimensional reconstruction of actin networks implements the same method used by humans to see depth, namely measuring the disparity between images taken at slightly different angles (stereo pairs). Objects near the observer shift significantly between stereo pairs, whereas objects farther away shift less.

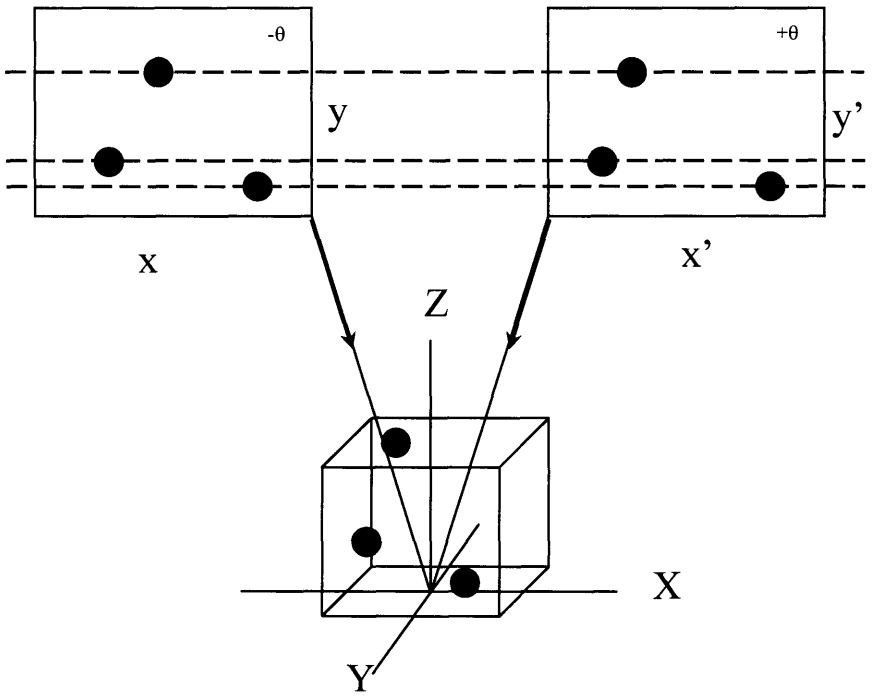

Figure 4.1 An illustration of the differences between two images taken of an object from different angles. The slight disparity of the points in the *x* direction is a result of depth.

For each point, the (x,y) coordinates are given by

$$\begin{bmatrix} x \\ y \end{bmatrix} = \begin{bmatrix} X\cos\theta + Z\sin\theta \\ Y \end{bmatrix}$$

(4.1)

$$\begin{bmatrix} x' \\ y' \end{bmatrix} = \begin{bmatrix} X\cos\theta - Z\sin\theta \\ Y \end{bmatrix}$$

From the above equations, Z can be isolated and related the x disparity according to the relationship:

(4.2) $$Z = \Delta x/(2\sin\theta)$$

The x disparity increases linearly with height. When θ is 10 degrees, Z is approximately 3 times Δx.

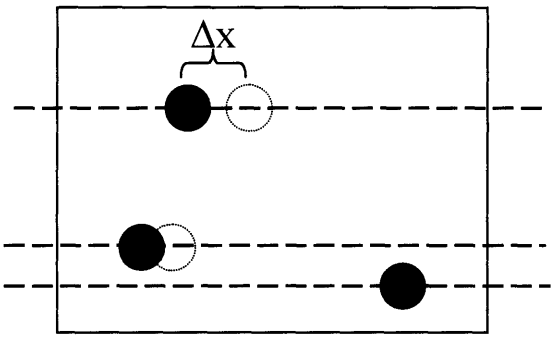

Figure 4.2 When the stereo pairs are superimposed, the x disparity becomes clear. The depth of each point can be calculated from Equation (4.2). There is no y disparity in perfectly aligned images. The gray points are from one stereo image and black points are from the second (the bottom right point is identical in each image).

This well-known geometric principle has been used by others to make quantitative observations about actin networks [184]. The method has been automated here, using a Java applet for computer-assisted coordinate mapping on side-by-side stereo pairs. The third dimension is calculated from the disparity, and MATLAB routines calculate geometric information about the network.

4.1 Java

A java applet provides an interactive interface for the mapping of the network from stereo images. The user views both images simultaneously and selects corresponding filaments in the images. The applet has an additional feature that animates the image for easier comprehension of filaments' spatial relationships. The user can add or subtract filaments, as well as alter the location of any points already mapped. From Equation (4.2) above, the program calculates the z coordinate for each point in real time, and produces a virtual three dimensional structure that can be rotated, moved, or zoomed.

When the user is satisfied with the reconstruction, the three-dimensional filament endpoints are exported to a file that can be re-opened by the applet or read by other processing tools, such as MATLAB as discussed below.

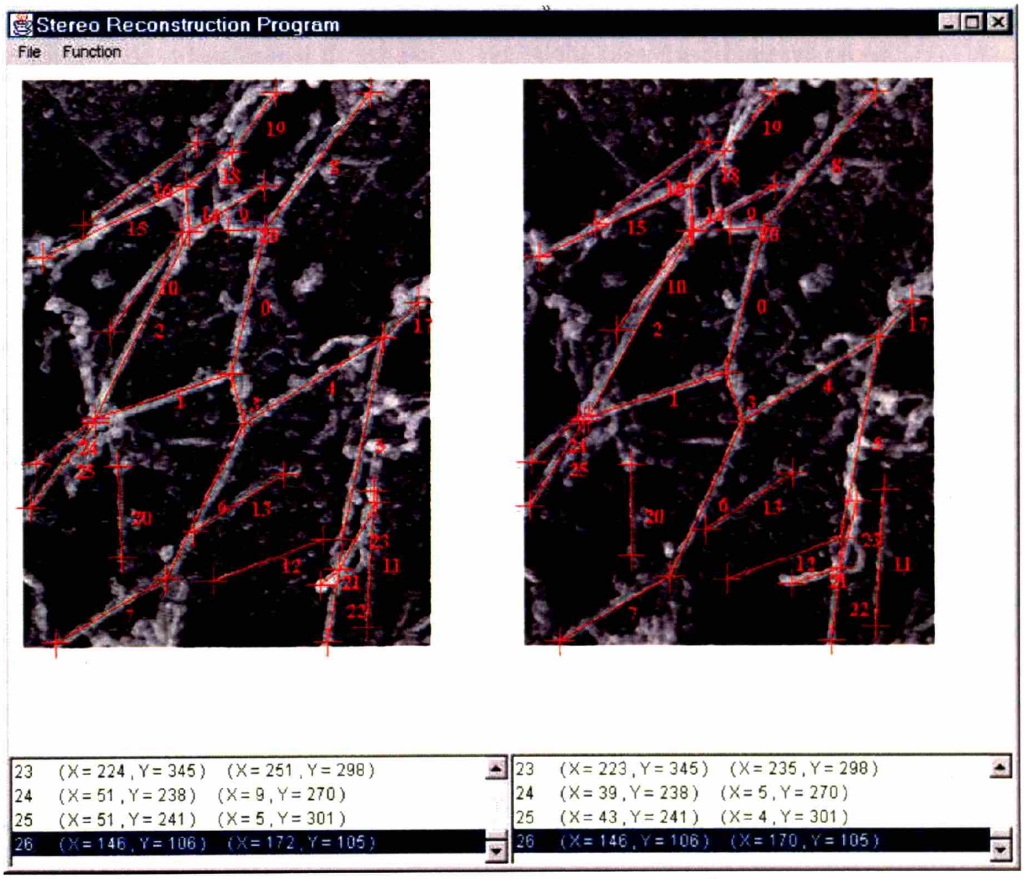

Figure 4.3 The GUI of the Java applet for filament selection. The user views both images side by side and selects corresponding filament endpoints in the images. The xy coordinates for each filament are displayed in the table below, and the z coordinate is calculated from the x disparity with Equation (4.2) . As shown, the y disparity of each point in properly aligned images is zero.

4.2 MATLAB

With the data from the Java applet, MATLAB computes geometric information about the network.

The program calculates the filament lengths and the distances between points of interest, such as junctions, according to the well-known formula:

$$d = \sqrt{(x_1 - x_2)^2 + (y_1 - y_2)^2 + (z_1 - z_2)^2} \tag{4.3}$$

Where (x_1,y_1,z_1) represents point one; likewise for point two.

For each intersection of interest, the program calculates the junction angle, θ, according to the vectors $\vec{A}$ and $\vec{B}$ of the two filaments composing it:

$$\theta = \cos^{-1}\left(\frac{\vec{A}\cdot\vec{B}}{\left|\vec{A}\right|\left|\vec{B}\right|}\right) \tag{4.4}$$

A key new feature of a computerized system is the determination of the closest distance between two filaments that potentially intersect somewhere other than their endpoints. Filamin cross-links are not limited to filament endpoints, yet manual methods work solely with endpoints. A computerized method works with the line segment between those endpoints just as easily.

The challenging problem of determining the magnitude and location of the shortest distance between two line segments is solved by first calculating the shortest distance between two vectors. The projection of any line segment connecting the two filaments onto the mutual normal vector between the filaments represents the shortest distance between the filaments.

The mutual normal vector, $\vec{N}$, between two filaments represented by vectors $\vec{A}$ and $\vec{B}$ is calculated from the cross-product:

$$\vec{N} = \vec{A}\times\vec{B} = \begin{vmatrix} \hat{x} & \hat{y} & \hat{z} \\ A_x & A_y & A_z \\ B_x & B_y & B_z \end{vmatrix} \tag{4.5}$$

where (A_x, A_y, A_z) represents any point on filament $\vec{A}$; likewise for $\vec{B}$.

The most convenient vector between $\vec{A}$ and $\vec{B}$ is one of the eight that connect the endpoints:

(4.6) $$\vec{D} = \vec{A} - \vec{B} = ((A_x - B_x),(A_y - B_y),(A_z - B_z))$$

where (A_x, A_y, A_z) represents any point on filament $\vec{A}$; likewise for $\vec{B}$. $\vec{D}$ can also be calculated as $\vec{B} - \vec{A}$.

Thus, the shortest distance, Δ, between $\vec{A}$ and $\vec{B}$ is the projection of $\vec{A} - \vec{B}$ onto $\vec{A} \times \vec{B}$, where the projection is calculated from the dot product

(4.7) $$\begin{aligned}\Delta &= (\vec{A} - \vec{B}) \cdot (\vec{A} \times \vec{B}) = \\ &= (A_x - B_x)(A_y B_z - A_z B_y) + (A_y - B_y)(A_z B_x - A_x B_z) + (A_z - B_z)(A_x B_y - A_y B_x)\end{aligned}$$

Again, (A_x, A_y, A_z) represents any point on filament $\vec{A}$; likewise for $\vec{B}$.

If the proximity, Δ, is less than a threshold, ε, set by the user the filaments cross.

Δ represents the shortest distance, but there are two limitations. One, the location of the crossing is unknown, and therefore the program cannot create the steric junction. Two, Δ is the shortest distance between two vectors $\vec{A}$ and $\vec{B}$, of infinite length, whereas actin filaments are finite segments of these vectors. Two short filaments which are far apart may, if extended to infinite length, pass near each other; this is a false positive.

Computationally, the problem is refined using the following algorithm:

1. Determine Δ as above, denoted $\Delta_{infinite}$.
2. If $\Delta_{infinite} > \varepsilon$, the filaments do not cross.
3. If $\Delta_{infinite} < \varepsilon$, the filaments do cross somewhere; the program needs to determine if the closest points lie on the physical filaments or somewhere meaningless.

If the filaments cross somewhere, the closest distance between the physical filaments is computed by moving parametrically along each filament and calculating the distances. If the minimum physical distance is less than ε, a junction is created at those points. This method provides not only the minimum distance (which could be calculated from a formula) but also the location of that crossing.

4.3 Validation

The model must be validated by testing its analysis of a known structure. The ideal calibration would be a physical structure that is placed in the electron microscope, photographed in stereo, and processed computationally. This would test every segment of the process, from the EM tilt

accuracy to the point selection in alignment. Unfortunately, the design, manufacture, calibration, and mounting of a micrometer-scale structure for electron microscopy is beyond the scope of this thesis. A second validation method would be a physical macroscopic structure that is built, photographed in stereo, and processed computationally. A set of children's tinker toys would be one option, or thin sticks connected by small balls of clay another. The chief disadvantage to this method is the difficulty in photographing a structure from precise ±10 degree perspectives with the camera rotated about a single axis. In addition, the known geometry has to be exact to calibrate the method. A third validation method is the one used here: the creation of a virtual 3-D structure that can be rotated arbitrarily, tilted in stereo, and projected (photographed) with great precision. All angles and distances are known. The only manner in which this structure differs from a physical model is the nuance of texture and shading; however, this difference could equally help or hinder the user so it does not represent systemic bias. This difference could be removed by rendering the structure in software such as Maya or 3DS Max to add texture, light, perspective, and shading, but limited time and resources prevent this excursion.

The structure chosen for calibration is a unit cube. This provides a test for the algorithm measuring the projections of large angles. The structure could be arbitrarily complicated or large, but this does not test the mathematics or implementation any more rigorously. To define the structure, the program is given a set of points in 3-space and a "connectivity" matrix. The connectivity matrix contains a 1 where two points are connected and a 0 where two points are not connected. So if point 4 and point 7 are connected, the matrix contains a 1 at row 4, column 7. The matrix is a triangular matrix since connectivity is symmetric, i.e., (4,7) is the same as (7,4). Based on these relationships the structure is drawn in 3-space. This is a much simpler data scheme than storage of a set of lines defined by their endpoints. Such a scheme would be difficult to alter, and it stores each point multiple times.

To prevent any oversimplification, the virtual structure is rotated about the x-, y- and z-axis an arbitrary amount. An equivalent alternative would be to tilt about an arbitrary axis rather than about the y-axis. If neither of the perturbations is applied to the neat case of a unit cube, the mathematics for reconstruction become trivial and the visual interpretation becomes impossible (lines project on top of each other).

From this rotated structure, the left and right stereo images are created by tilting the structure -10 ° and +10°, respectively, about the y-axis and then projecting each point onto the xy-plane. The lines are given width in order to simulate real filaments.

These two images are loaded into the Java point selection applet. Each corresponding line in each image is selected point by point. The magnification of the images was about double what is shown below in Figure 4.6. To provide a more challenging reconstruction test, the points were carefully selected with a small, single-button, mechanical mouse to create imprecision. An additional difficulty results from the structure's points being obscured by Java lines and cross-hairs (these can be toggled off if desired). The coordinate windows below the images indicate

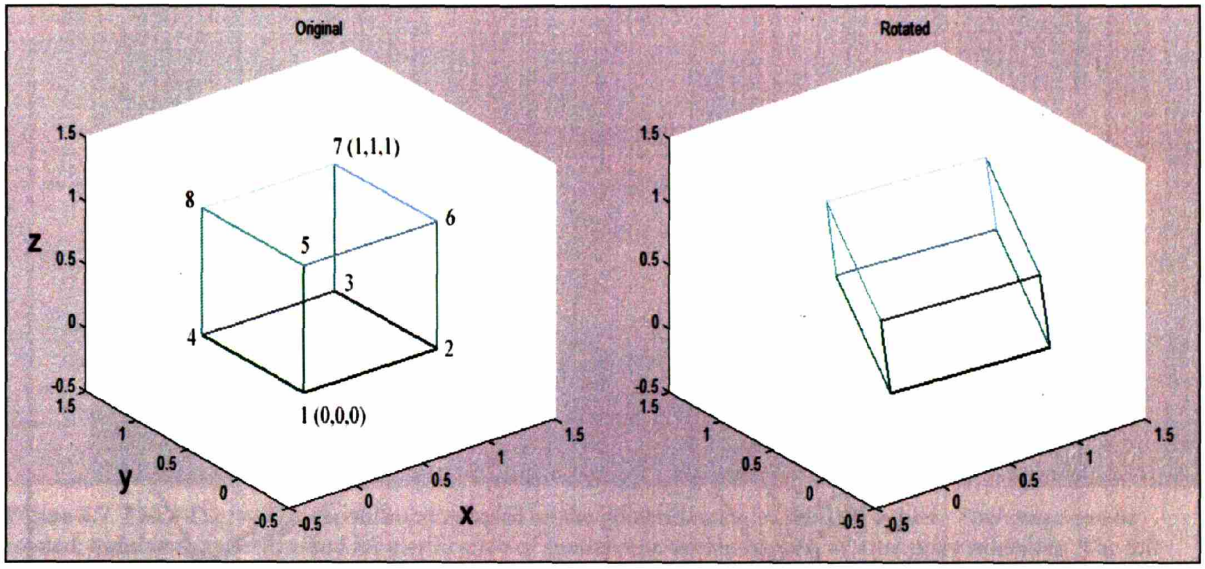

Figure 4.4 The test structure for validation of the reconstruction algorithm. Left, the original structure constructed from a set of points and a matrix of point connectivities. Right, the same structure rotated an arbitrary amount about all three axes.

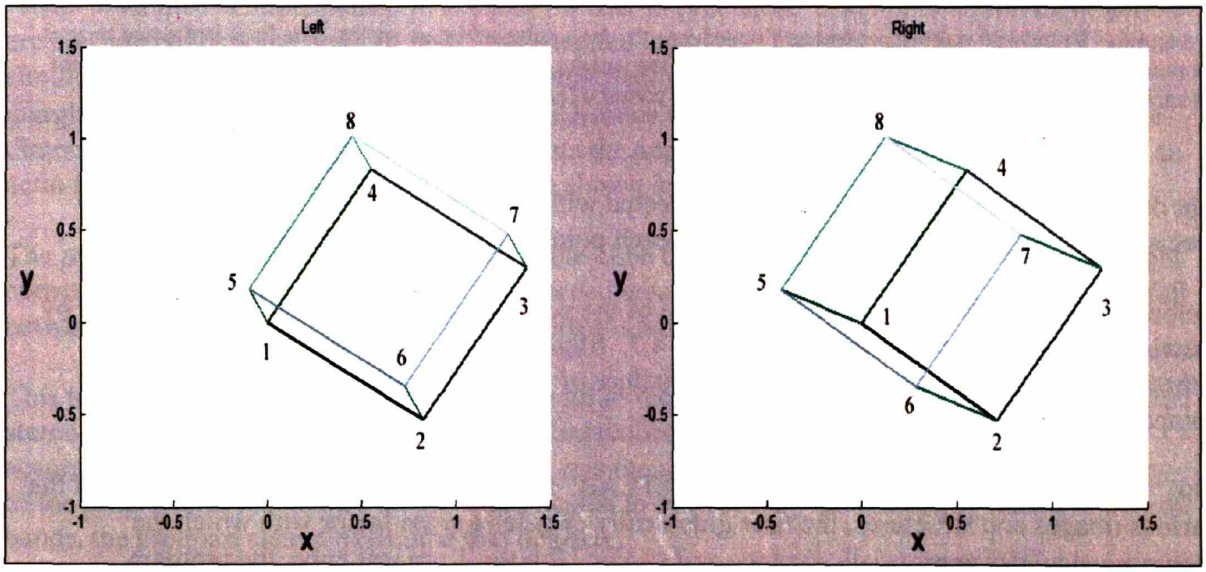

Figure 4.5 The projected left and right stereo images of the rotated structure, ready for reconstruction.

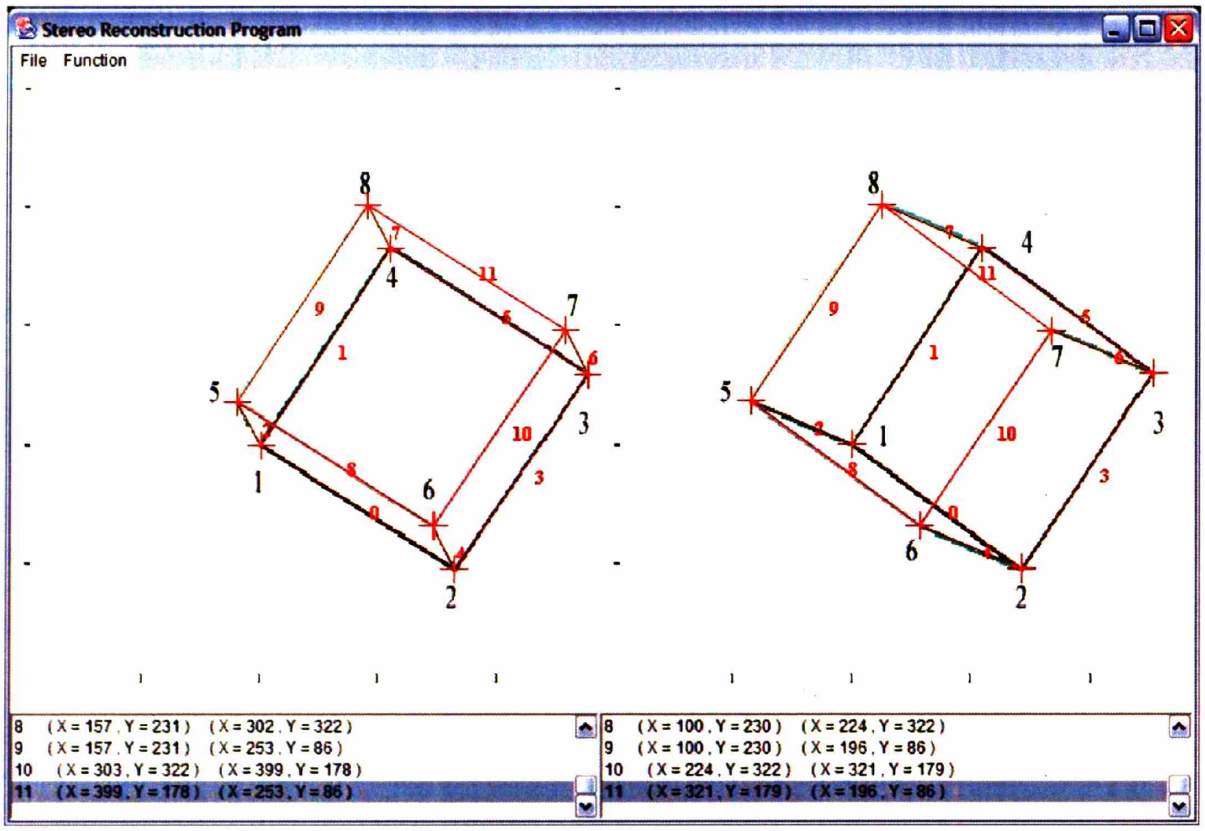

Figure 4.6 The left and right stereo images loaded into the Java point selection applet. The lines in the two images are numbered 0-11 in each image. In the table below the images, the x and y coordinates of the start and end point for each line are given. The origin is at the upper left corner of each image with $+y$ down and $+x$ to the right.

that despite these challenges, points were selected with a maximum error of 1 pixel (with full precision, the y-coordinates are identical for each point as described in Section 4.4).

Before processing the data, an approximation of the point selection accuracy can be obtained by viewing the reconstruction, shown in Figure 4.7. Slight flaws are visible in the structure, although in the general case the "correct" structure of the actin network is not available for comparison.

This virtual structure is then analyzed by MATLAB. Because of the different pixel ranges of the various images and structures, the user graphically chooses a scale factor with which the program calculates appropriate distance and angles. For the 1 μm test cube, the program produced the following results for the distribution of filament lengths (Figure 4.8). The accuracy is within 3%.

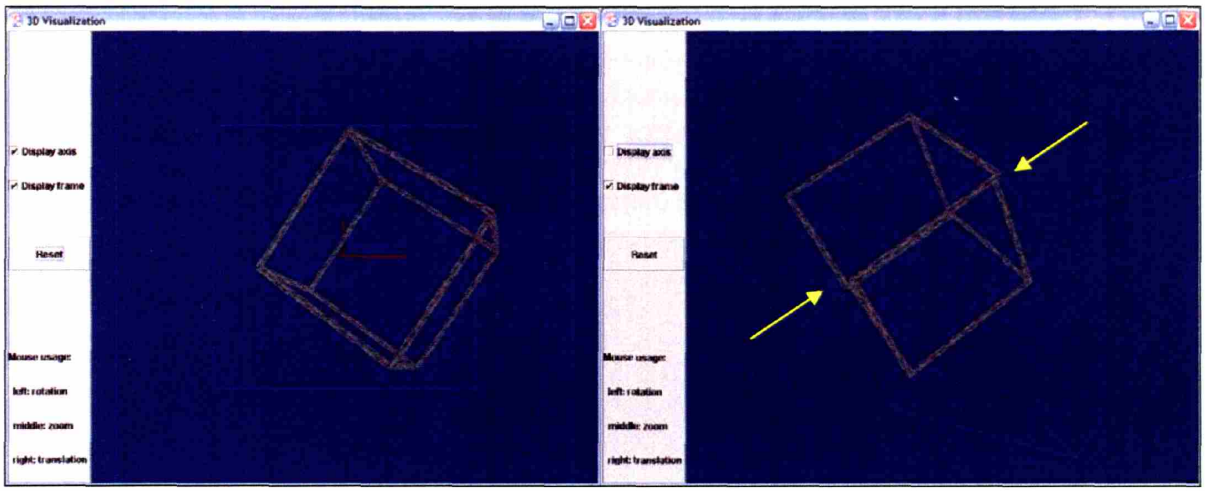

Figure 4.7 The 3-D graphical reconstruction based on the point selection of the Java applet. The image can be rotated, translated, and magnified for clarification of spatial relationships during or after point selection. The left panel shows the cube looking down the *z*-axis, which hides errors in the depth calculation. The right panel shows the structure rotated a few degrees, revealing slight flaws (yellow arrows) in the cube's geometry due to errors in precise point selection.

Without further input from the user regarding connectivity, the program determines which filaments produce junctions, whether due to adjoining endpoints or due to steric crossings. A "snap" tolerance is implemented to account for user imprecision. Endpoints within this tolerance are considered the same point in space and snapped together. The program considers all points simultaneously to prevent one adjustment from affecting the relationship between two other marginal points. For this example, the snap tolerance was 20 nm, or 2% of the 1 μm unit cube dimension. This distance physically represents the approximate metal-shadowed diameter of an actin filament. The junction angle results are shown in Figure 4.9.

The program found all 24 junction angles in the cube despite user imprecision (each of the eight corners contains three right angles). The returned results are accurate: all but 5 of the angles fall between 89 and 90 degrees. The maximum error is less than 3%.

This test confirms that the program is successful in reconstructing a structure from two projected stereo pair images of it. It accounts for user imprecision and returns geometric information accurate within a couple percent. Ultimately it is the user and the image that limit the accuracy of the program. If the images are too complicated to be precisely interpreted by human eyes and hands, the program cannot overcome that obstacle.

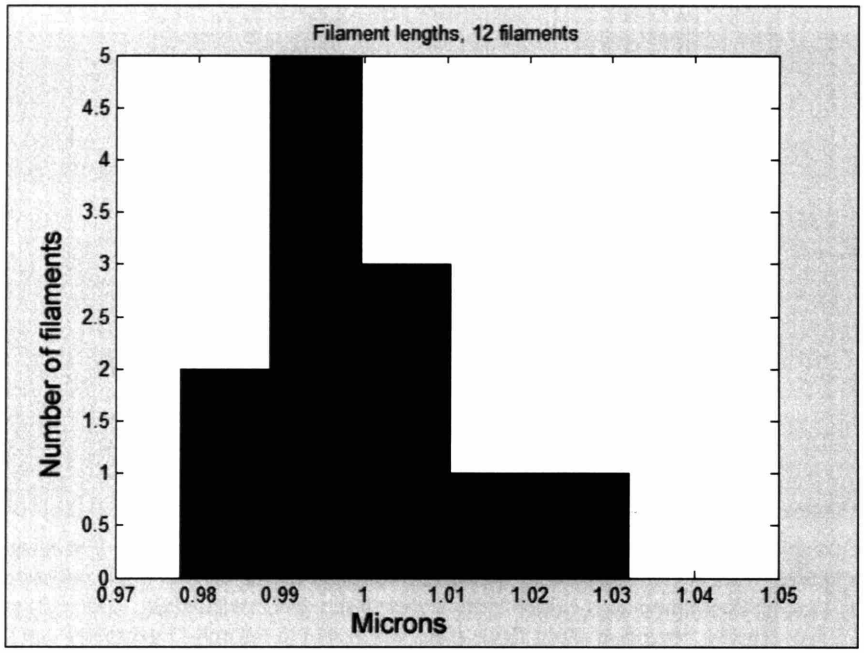

Figure 4.8 The MATLAB summary of the length distributions for the structure. The filaments all fall within 3% of their true length.

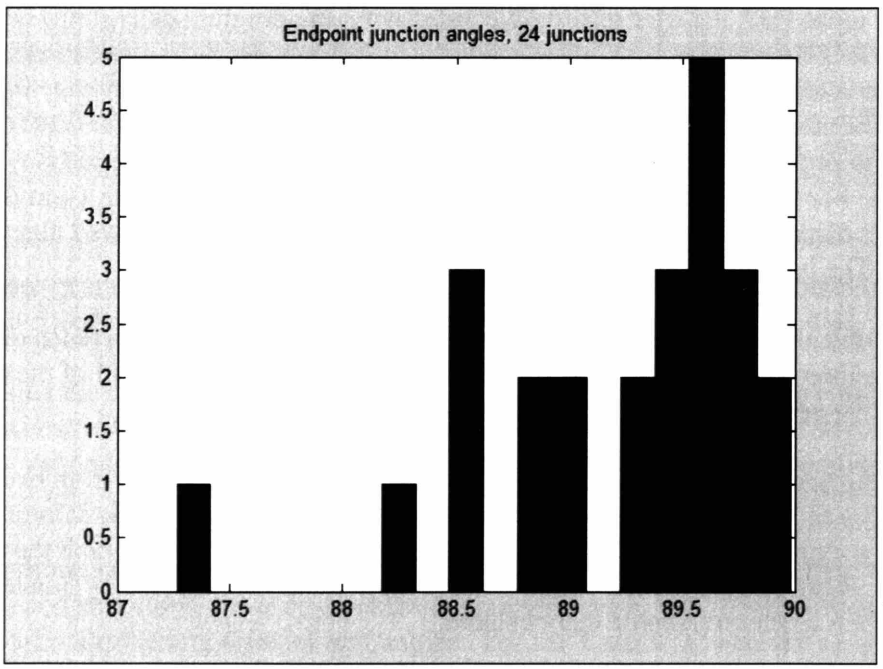

Figure 4.9 The MATLAB distribution of the junction angle calculation for the calibration test: a unit cube with 24 right angles. All angles are calculated within 3 degrees of their true value.

4.4 Image pre-processing

The usage of the Java applet is straightforward: the user selects points and the program stores the coordinates of those selected points. The images themselves, incidentally, are not used by the program itself; they are merely visual cues for the user to choose the correct coordinates. As such, the image quality is irrelevant to the functioning of the program. Ultimately the Java applet uses a single formula to calculate the z-coordinate of each point.

The MATLAB portion of the program, while rigorous under the hood, is also straightforward to use. It imports the three-dimensional coordinates from the Java applet and performs a variety of geometric manipulations and measurements on the table of coordinates.

However, both steps are based on a fundamental assumption: the images are aligned. In fact, raw digital images are always misaligned. A new algorithm has been developed to align images; its accuracy is orders of magnitude higher than previous methods and it is more efficient computationally.

Challenge

Perfect alignment of both images is necessary for the reconstruction algorithm to be performed correctly. The algorithm measures differences in x to calculate z, and if there is imprecise alignment, the measured x will be incorrect and the algorithm will return incorrect results.

Aligning two identical images is a trivial task: the user need only select two points in each image and rotate and translate the lines connecting the points until they coincide. There are an infinite number of aligned orientations since there is no external reference. Typically, one image is considered "correct" and the second image is adjusted to match the first. However, stereo pairs are not identical images; each point in one image shifts an unknown amount in the other, so relative distances and angles vary and point matching is impossible. Additionally, there is only one orientation in which both images are aligned with each other and with the tilt axis. Neither image is "correct;" both must be assumed incorrect.

Misalignment comes from three primary sources:
1. Camera rotation misalignment
2. Misalignment of negatives
3. Misalignment during digitalization

In the first situation, the camera's axis of rotation, rather than coinciding perfectly along the y-axis also has a perpendicular x-axis component. As a result, there is a y-shift in the images as well.

In the second situation, nothing has changed physically in the sample, but due to imprecision in the negative holder within the camera, the images will be rotated relative to each other even when the physical negatives are aligned perfectly next to each other for digitization.

In the third situation, the physical negative is rotated when being digitized. All internal geometric relationships in the negative are maintained, but they are distorted relative to the other negative. Again, this discrepancy, if not corrected, feeds invalid *x,y* data to the reconstruction algorithm.

All three sources of error are variants of the same type: solid-body rotation and translation of the image itself, and not any distortion of the underlying science. Fortunately none of these three sources of error are insoluble. In case (1), no matter how misaligned the camera is, as long as it rotates about a single axis, the pair of images is a proper stereo pair with depth information. The axis of rotation is no longer "up" in the images, and the disparity is no longer horizontal, which the program requires. Thus the axis of rotation needs to be determined and both images rotated so that the axes are vertical. In cases (2) and (3), the images are rotated out of position, and need to be realigned. In all three cases, the axis is unknown but needs to be rotated until vertical in the stereo images.

An additional obstacle in the process is that both images are misaligned. Some previous alignment standards exist to realign a single misaligned image with its aligned partner. In the case at hand, there is no standard; both axes need to be determined.

Assumptions

The only assumption for alignment is:

- There is one axis of rotation and thus that there is a single direction defining all point motion between aligned images.

Due to isotropic symmetry of the sample, for alignment it is not necessary to assume:

- The axis of rotation is in the *xy* plane (parallel to the "bottom" of the sample)
- The axis of rotation is oriented in any particular direction relative to the *x* or *y* axes.

This differentiates our solution from the previous alignment algorithms of Cheng [185], Lawrence [186], and Luther [187].

In addition, this solution does not assume knowledge about the tilt angle of the original stereo projection. It aligns the images based on information on the images alone, other methods solve

for a corresponding set of 3-D points which can only be determined if the tilt is recorded and known.

Solution

The alignment algorithm is successful if it produces an orientation of both images such that the only relative motion between any two corresponding points in the images is entirely horizontal. Rather than try to solve a larger, more abstract problem (recreate a set of 3-D points that would project a set of selected points from a certain angle in a manner that properly rotates about the y-axis) as others have done, the solution presented here attacks the problem at hand: remove the rotational and translation discrepancy between the stereo images. This solution is faster, more accurate (linearization is not necessary), more general (small angle assumption is not necessary), and requires less information (tilt angle need not be known).

After the user selects a set of at least three "control points" in each image that register identical shared features, the solution implemented is to project this set of control points in each image onto the vertical y-axis, measure the distance distribution of the points along the y-axis, and rotate the images independently until a solution is found in which the distribution of the y-projections of points is identical, as illustrated in Figure 4.10.

This solution is necessary, sufficient, and in all non-trivial cases, unique. Assuming the points are located at different depths, z, the x-disparity in the aligned images will be different for each control point according to Equation (4.2) and the y disparity will be zero; i.e., the disparity vectors are purely horizontal but have different magnitudes. After misalignment, the disparity vectors are no longer horizontal; they have gained a y component. Because the vectors are of different magnitudes, the amount of (errant) y-disparity differs for each point.

The only unique solution for which the projections in the images will have identical vertical disparity is when the vertical disparity is zero and the images are properly aligned with the vertical axis and with each other.

In practice, rather than rotate the control points, the program rotates the axes.

There are two limitations of this solution. One, a second solution exists in (180,360) in which the images are upside down and perfectly aligned. Two, if the control points are all selected at an identical depth, the disparity vectors for each point will be identical, and there are an infinite number of solutions.

Because the alignment is performed in MATLAB, additional features can assist in point selection that are unavailable in the Java applet. The image can be magnified for precision, for example, and optional subroutines can optimize point selection by measuring properties of the image

(brightness gradients, edge contrast, etc.) at the corresponding control points and adjusting the user's pixel selection accordingly.

Validation

This alignment algorithm was tested by generating five random control points (CPs) within a 400 pixel square centered at the origin, representing the CPs in one image (termed the "left" image). To simulate stereo shift, each point was shifted horizontally a random distance on [-10,10] in order to create CPs in a second ("right") image. These are precise stereo pair data.

In order to simulate imprecision, the entire set of right CPs was shifted a random distance on [-50,50] in both the x and y directions. After shifting them, a random rotation was applied to both sets of CPs. This angle could be arbitrarily high and the algorithm does not fail. In order to simulate realistic situations, the angular rotation was limited to 20 degrees (reasonable care bounds this well within 5 degrees in practice), and the rotational search algorithm limited to [-90, 90] for each image. Alternatively, the algorithm can be easily tweaked to solve for larger than 90 degree rotations, which could most easily result if the operator is not aware which axis represents the tilt axis in the images and digitizes both images with 90 degree rotation.

Using these settings, tens of thousands of simulations were run. The assignment was to rotate both images independently until the geometric relationships between the CPs was the same in each image. The metric we used was the relative distribution of the y coordinates of the CPs. A perfect solution would yield a difference of zero of the distance between any two CPs between the two images. In the solutions our algorithm produced, the average y shift between the aligned images is 10^{-6} pixels, and the random angle is recovered with a mean error less than 10^{-4} degrees. This is in comparison to the method of Cheng which uses 4-5 iterations to achieve a precision of 10^{-2} degrees.

In addition to the artificial stereo images created above, other simulations were run using projections from randomly generated 3-D points. Using the matrix methods elaborated by Lawrence and Cheng, the projected CP $a(x,y)$ resulting from the actual 3-D location of $A(x,y,z)$ is $a = PTA$, where P is the xy projection matrix and T is the tilt matrix (assuming tilt angle is known). Rotational and translational imprecision are added with the same bounds as above, such that $a = RPTA + d$ and solution results are identical.

The main benefit of the previous algorithm is that the physical 3-D points that project the CPs are calculated. However, while z is greatly important for 3-D reconstruction, it is unnecessary for image alignment and thus represents inefficiency.

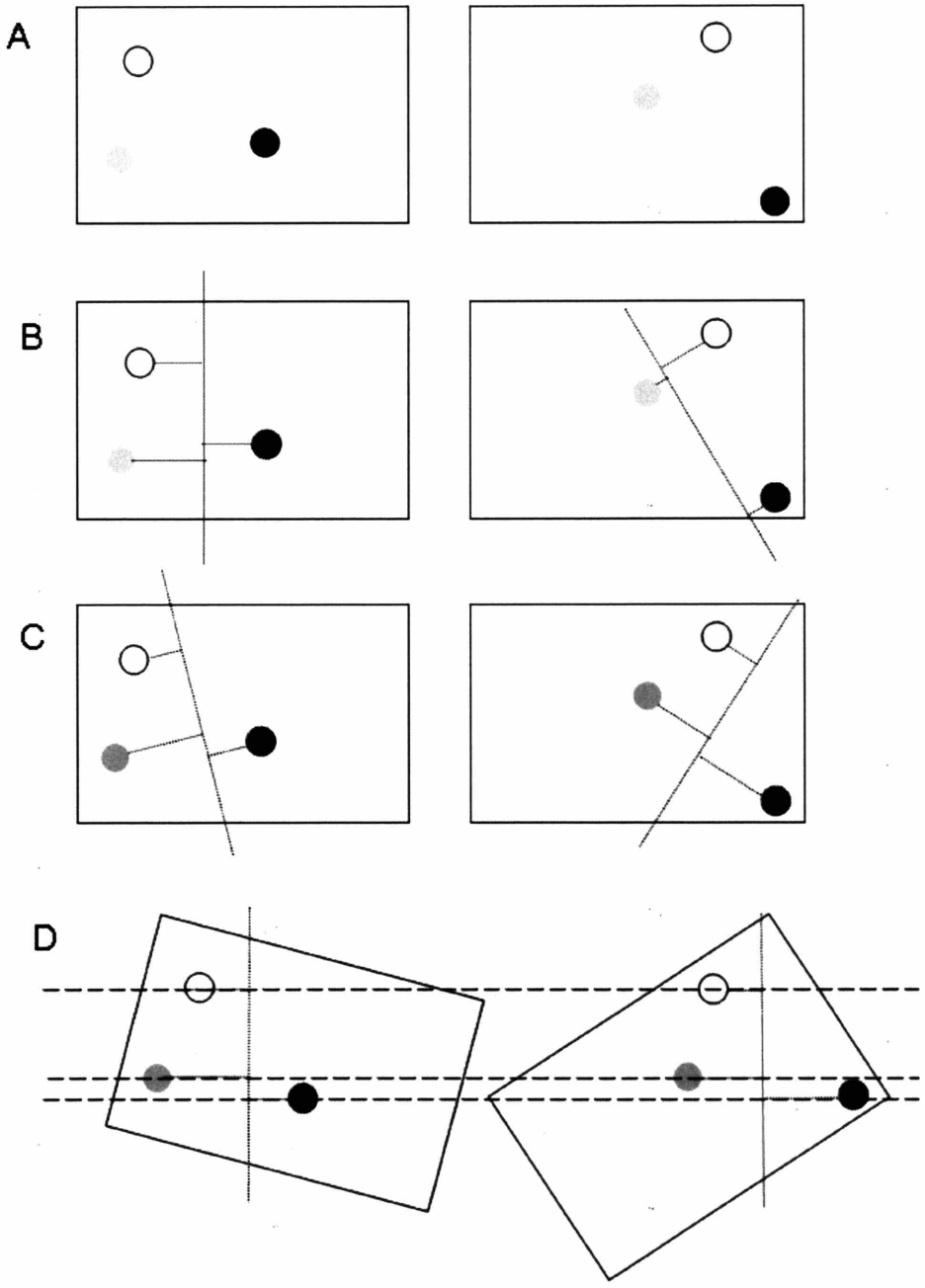

Figure 4.10 Illustration of the problem and solution of stereo image alignment. A, both images have inadvertently been translated and rotated out of alignment. B, to find the proper alignment, the points in each image are projected onto independent axes and the relative distances measured. The axes shown are not solutions since the point spread differs. C, the solution with identical point projections. D, the two images rotated into alignment and ready for reconstruction.

Chapter 5 Results

5.1 Filamin structure

From glycerol sprayed filamin molecules (described in Section 3.8), it is easy to find molecules that are deposited by the receding droplets, as seen in Figure 5.1. Thousands of molecules have been observed in the electron microscope and several observations have been made that differ from the original and current views of the structure of filamin. The images were processed in MATLAB as described in Section 3.10 .

Result 1: Filamin is flexible.

Initially described as "rod-like" and a "leaf-spring" (a structure composed of staggered metal plates), from the contour it can be seen that there is a great deal of curvature, bending, and change of direction. While the two-subunit schematic for the filamin homodimer is still accurate, rarely is seen a stiff V or Y shaped molecule. The persistence length, L_p, of the molecule was measured to be 13.8 ± 8.2 nm (using the method of Section 3.10), which is approximately 1000× more flexible than actin. This value is calculated from the mean squared end-to-end distance and the contour length of each filamin molecule.

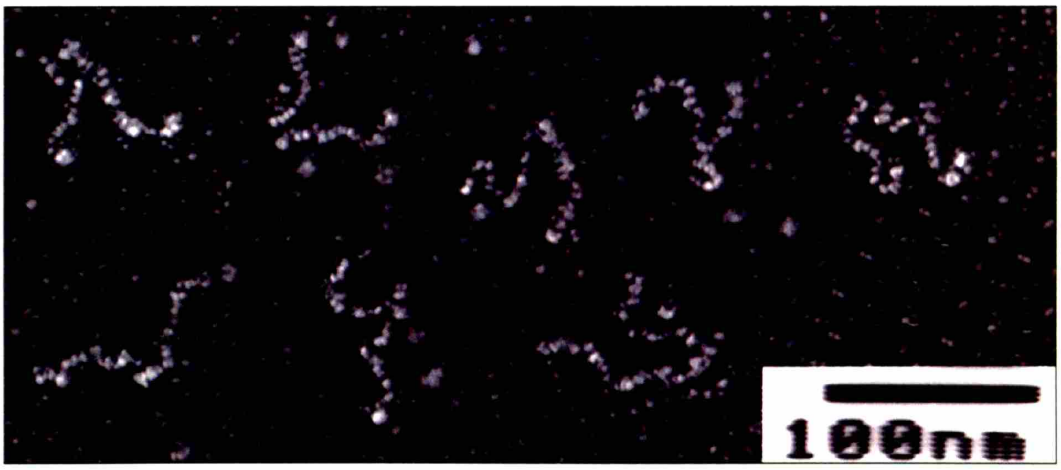

Figure 5.1 Representative images of filamin obtained by the glycerol spraying method described in Section 3.8. The molecules are approximately 150 nm long (145.6 ± 11.5 nm) and have a persistence length of 13.8 ± 8.2 nm (N=17).

Result 2: Filamin's curvature is continuous.

Rarely is seen a discontinuity in the curvature as would be expected from rod-like domains joined by small hinges. The actin-binding domain frequently turns sharply from the filamin

subunit, and a sharper-than-normal curvature is frequently seen around the position of hinge 1, but the hinge does not seem to allow two sections of the molecule to spin freely about each other like a ball joint. There is no evidence that hinge 1 is a hinge, per se, but rather the transition point between two sections of the peptide chain.

Result 3: Filamin's self-association region is stiffer than its N-terminal domains

Individual molecules do not lie as a straight line, nor do they cross themselves often as flexible polymers would. At the center of the contour, near the self-association site, there is always a kink: a U-shaped bend (Figure 5.2). While the N-terminal domains of molecule are flexible, the self-association region is not. This is a great advantage for network structure, as described in Chapter 6.

Standard persistence length analysis is not suitable for quantifying rigidity, as the persistence length is a measure of curvature, and not a measure of variability. A C-shaped curve, for example, can be very rigid and yet have a small persistence length due to its small end-to-end distance. The persistence length assumes a flexible polymer, the shape of which inherently has great variability, and quantifies that flexibility.

Variance is a better measure of how much a curve varies from specimen to specimen. Examining the intramolecular distances of 24 filamin contours, the standard deviation of the mean end-to-end distance of the approximately 50 nm segments from the N-terminus to hinge 1 was 17.9 nm. The standard deviation of the mean end-to-end distance of the approximately 60 nm segments from hinge 1 on one subunit through the self-association site to hinge 1 on the second subunit was 10.3 nm. The segments were chosen visually rather than mathematically because the contour length and orientation of each molecule varies. Thus, the location of hinge 1 on each subunit was assigned.

This result is supported by the findings that repeats 1-15 have intrachain hydrophobic interactions whereas even-numbered repeats beyond the first hinge (16, 18, 20, 22, 24) diverge slightly from the consensus repeat [136]. These structural differences may well explain the difference in stiffness.

Result 4: Dimerization weakens filamin stiffness

The persistence length of the subunits is compared to that of the entire molecule. The subunits have L_p = 22 nm whereas L_p for the entire molecule is 14 nm (Result 1). Not only is L_p 50% greater for the subunits, but since they are also half the length, the effective stiffness of the subunits, L_p/L_c, is three times higher than that of the entire molecule. Both values of L_p/L_c are less than 1, so neither the subunit nor the molecule are "stiff," but each subunit is more stiff than the molecule.

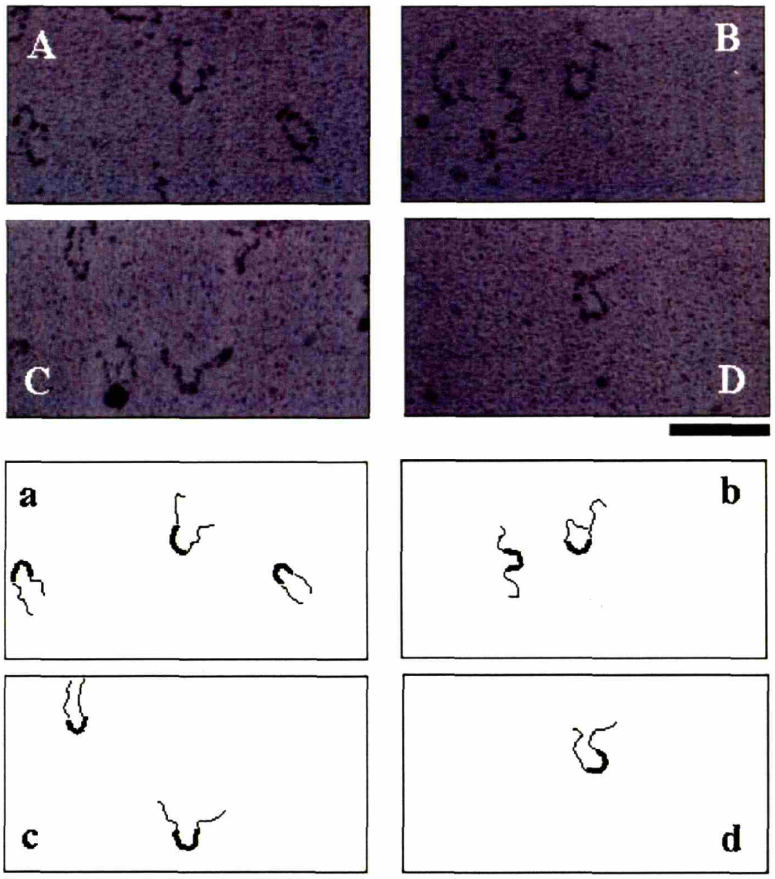

Figure 5.2 Micrographs of filamin molecules illustrating the consistent shape, highlighted in corresponding graphics below. Each molecule seems to have a U-shaped self-association region and two flexible N-terminal domains. Bar 100 nm.

Due to the differing domains within the subunit, this result is hard to interpret. The self-association site could be a hinge, but this is unlikely given Result 3. The ends of the self-association region are separated by 30 nm, so perhaps the additional end-to-end distance of the molecule comes from the distance between the start of flexible arms.

5.2 Filamin binding

For the first time, filamin has been observed *in situ* in actin networks. As described in Section 3.1, the molecules were decorated with a cocktail of six monoclonal antibodies, three near the N-terminus, two near hinge 1, and one near the self-association site.

Result 5: Filamin binds along actin (immunogold labeling)

With roughly 90% of gold particles bound to F-actin, as shown in Figure 5.3, the entire length of filamin must bind F-actin. There may be other interpretations of the labeling, but none are more plausible. Filamin might be too small to see as a standalone tether, but comparably-sized spectrin is preserved with this method. It could be a non-specific actin interaction, or an aldehyde interaction, but there is no labeling in M2 cells. The filamin could be on a different plane and merely projecting through the filaments, but stereo three-dimensional viewing confirms that these filamin are in the same plane as conjoined actin.

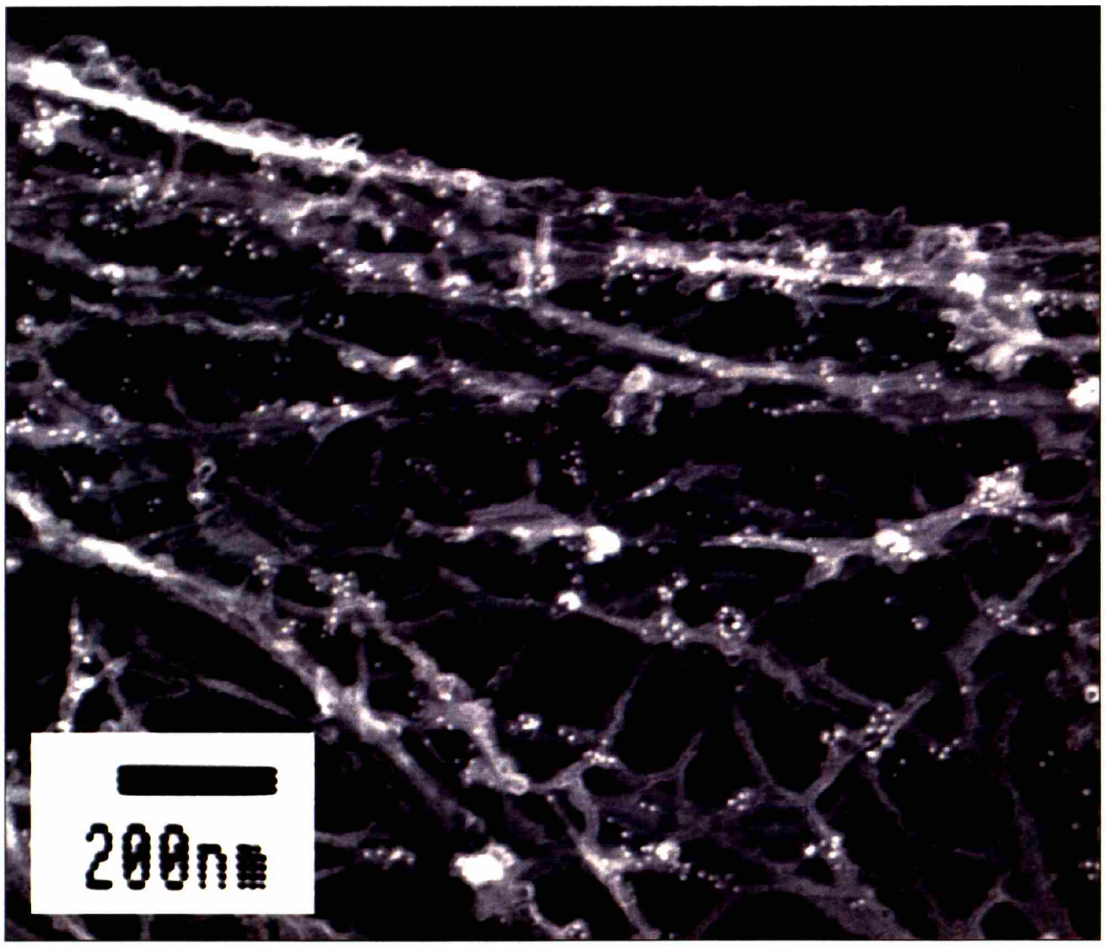

Figure 5.3 The cytoskeleton of an A7 human melanoma cell stained with 10 nm immunogold targeted against six monoclonal antibodies against filamin A. The gold particles are seen along F-actin in linear arrays and clusters, predominately near junctions.

Because the specific epitope of each monoclonal is known, a fully labeled filamin subunit should appear as shown in Figure 5.4.

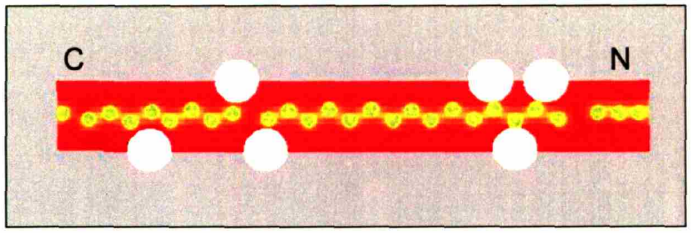

Figure 5.4 The approximate layout of the monoclonal antibodies on a filamin subunit (yellow). The N-terminus is at the right of the figure. The ABD is shown with a length of three repeats, gaps are included for insertions, and the 24 repeats are yellow circles. The total molecule length is 80 nm, and the repeats are shown in staggered linear layout. There are three gold particles targeting repeats 1-2, 3, and 4, respectively. There are two gold particles near hinge 1, and one near the C-terminus at repeat 20. The red box enhances visibility on micrographs.

However, the anti-species conjugated immunogold can amplify the signal non-uniformly by attaching an unknown number of gold particles to each monoclonal. With this caveat, and the unknown effective distance of two antibodies bridging each gold particle and its filamin A epitope, patterns were observed in the gold labeling.

Not every filamin molecule is necessarily labeled, and those that are labeled are not necessarily labeled with all six monoclonals. The location of filamin molecules was determined by identifying regularly spaced clustering within 80 nm segments. In some cases, there were alternate configurations that would also satisfy filamin's geometric constraints. Several junctions are shown in a three-dimensional anaglyph in Figure 5.6, which is best viewed with red/blue glasses.

Result 6: Filamin cross-links F-actin into large angles

For the first time, the angles of filamin-regulated F-actin junctions were measured in three-dimensions and analyzed. Junctions with gold labeling were chosen, and the participating actin filaments were traced in stereo pairs. Figure 5.7 shows the angles are biased toward 90 degrees, but not as sharply as previously reported [179]. The mean is 74.8 degrees and the standard deviation is 12.9 degrees. The previous report analyzed junctions bound to glass, without filamin labeling.

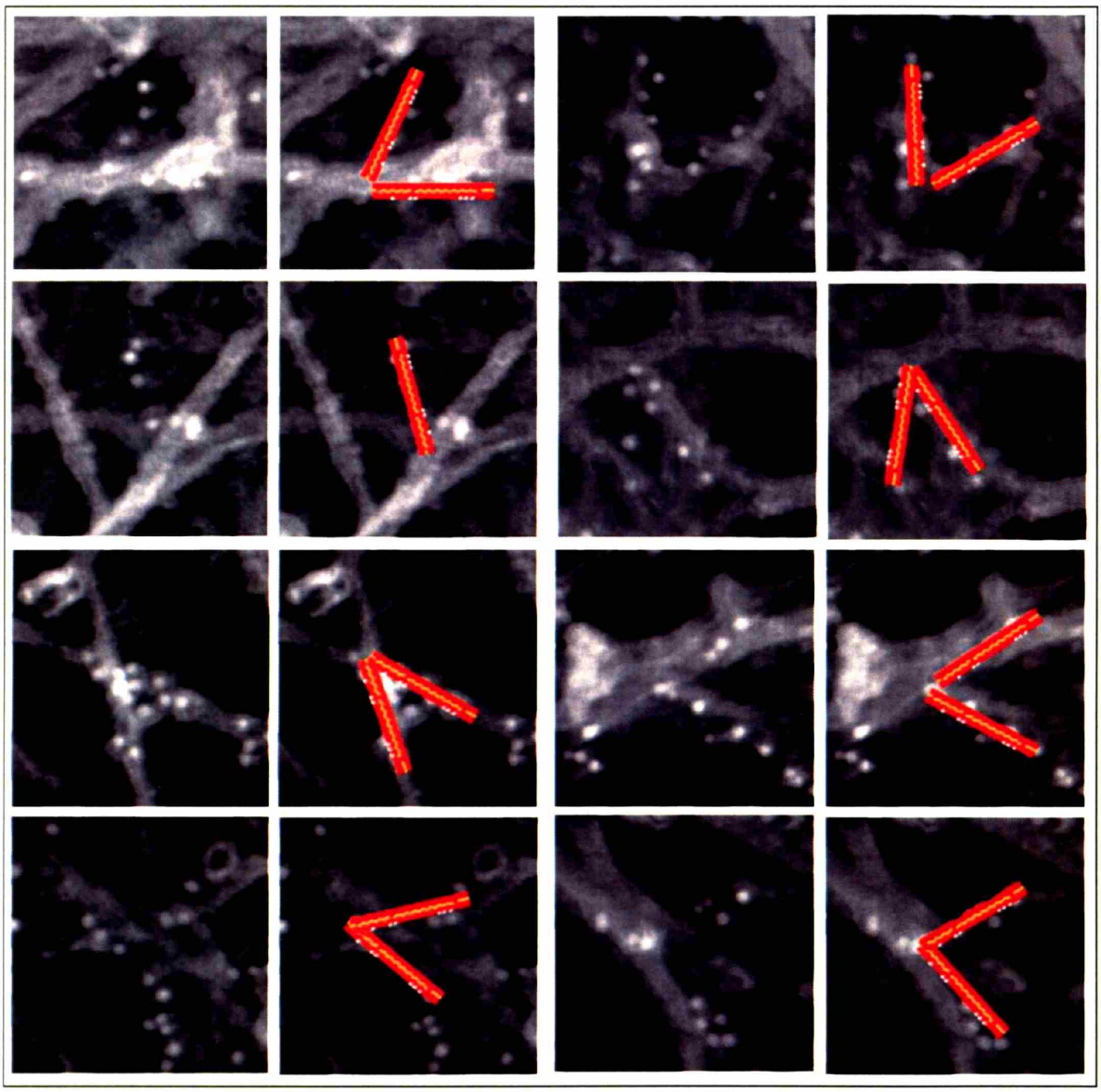

Figure 5.5 Individual filamin molecules at actin junctions. The columns are paired: the left column in each pair shows original images while the right shows the images with schematic gold-labeled filamin subunits superimposed. The red subunits each measure 80 nm and have been placed following stereo three-dimensional analysis.

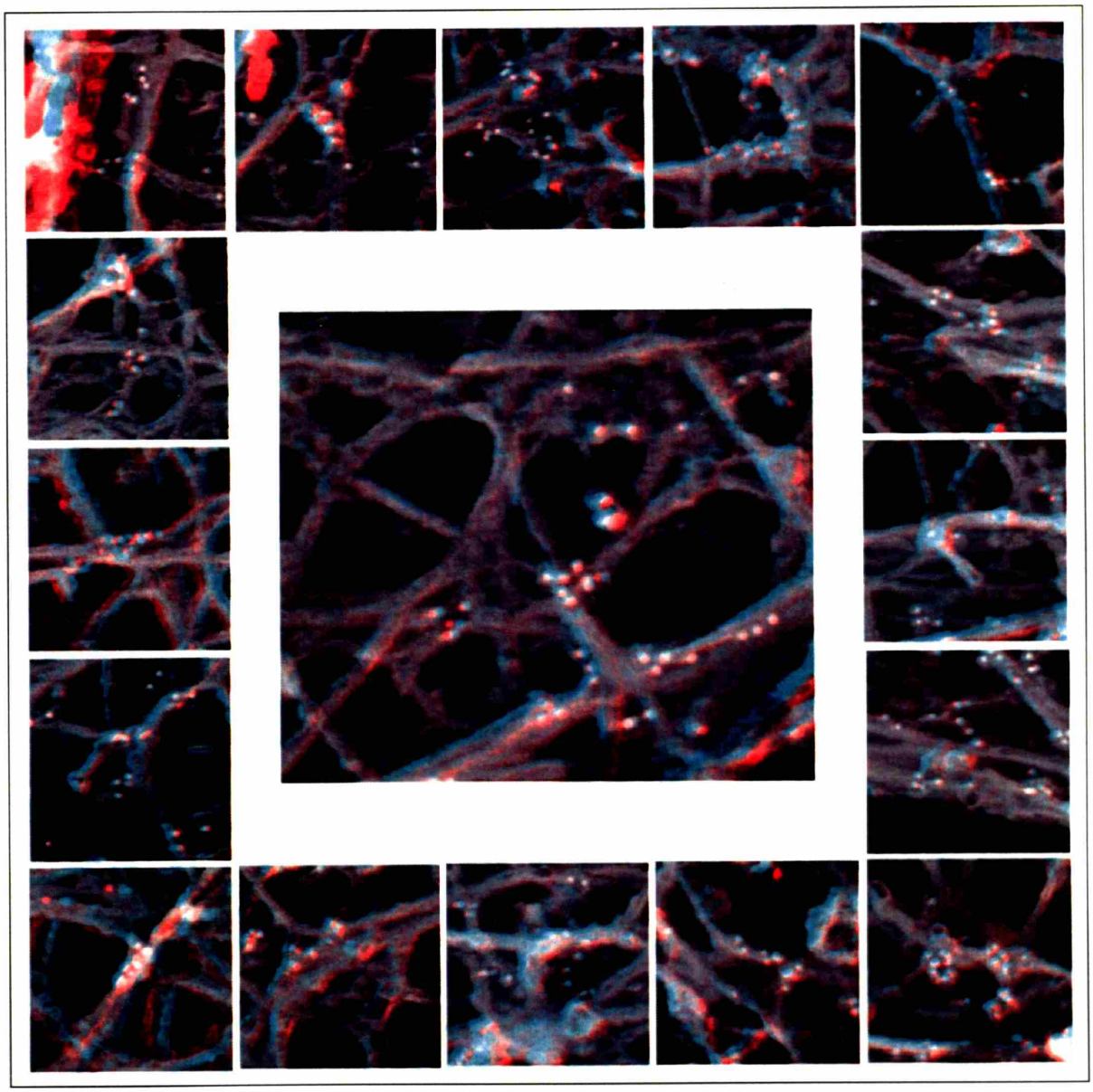

Figure 5.6 A three-dimensional anaglyph of selection F-actin junctions with linear, clustered immunogold labeling. The image can be viewed with red (left) blue (right) glasses. The center panel shows an orthogonal junction braced by two L-shaped filamin molecules.

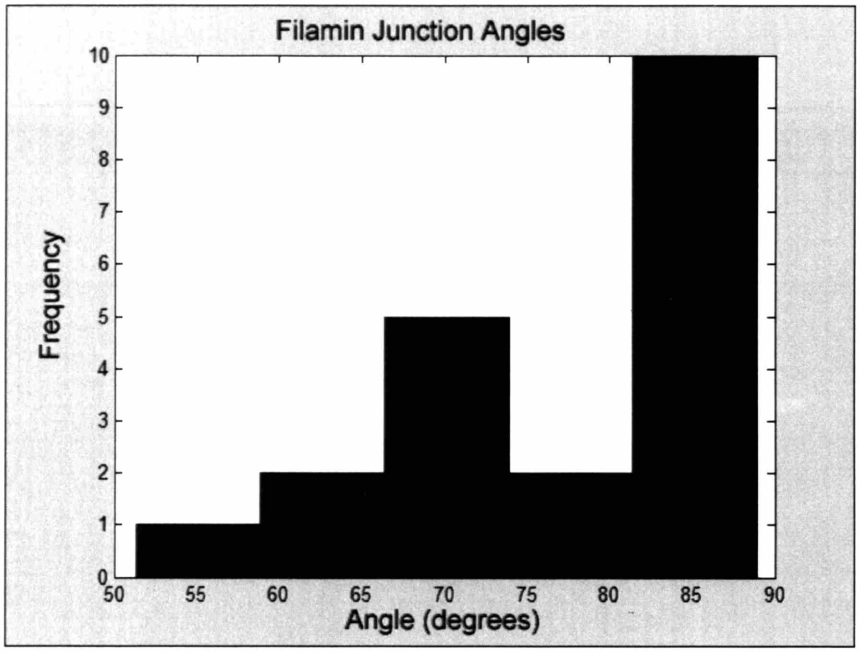

Figure 5.7 The distribution of three-dimensional angles of F-actin junctions regulated by filamin. N= 20, mean = 74.8 degrees, SD = 12.9 degrees.

Result 7: Filamin binds along actin (direct visualization)

Result 5 was confirmed by visualization of filamin molecules in dilute solution. Filamin molecules have been directly observed hanging off F-actin, as shown in Figure 5.8. A couple strand-like lines were visible near actin junctions in an earlier paper [179], but without labeling they could be contaminating proteins or glycerol drying lines.

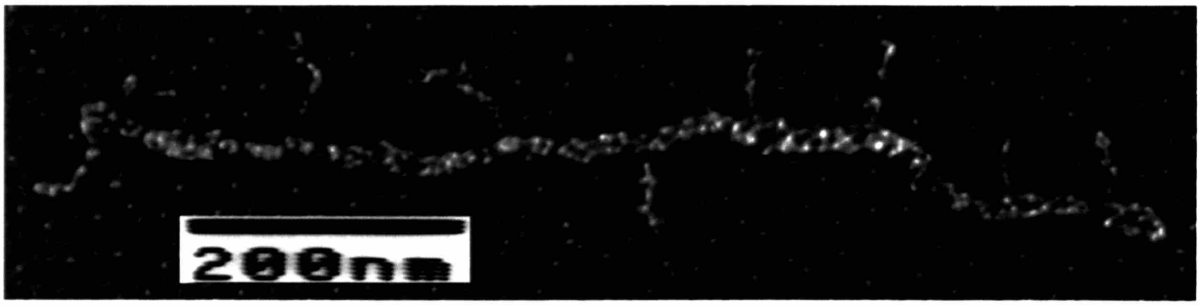

Figure 5.8 Composite of filamin molecules projecting from actin filaments observed by electron microscopy. The molecules are thinner than actin filaments and vary in length from 50-80 nm, which supports the hypothesis that each of these projections is a single subunit of filamin.

Result 8: The protrusions are single subunits, not entire molecules

Seventy of these protrusions were measured to determine what portion of the molecule was hanging from the actin filament. If the filamin molecule only binds at its ABDs, there would be complete (~150 nm) filamin molecules attached to F-actin at one end, in addition to occasional U's where both ABDs bind. If the molecule binds along its subunit as hypothesized, the projection should be on the order of 70-80 nm. The distribution favors this latter interpretation as shown in Figure 5.9.

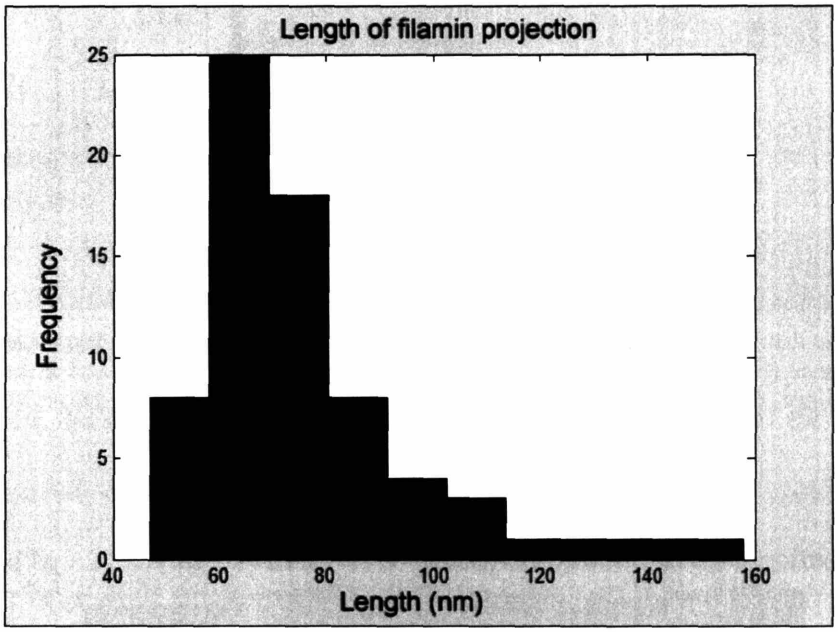

Figure 5.9 The length distribution of the projecting segment of filamin has a mean of 66.3 nm and standard deviation of 20.6 nm (N=70) which agrees well with one subunit hanging free from the filamin.

Result 9: Single filamin subunits do not hang off actin.

Another interpretation of these results is that the protrusions represent a subunit of filamin, but as a single subunit attached at the ABD with the C-terminus distal (Figure 5.11). However, identical experiments with single filamin subunits do not reveal these same protrusions as would be expected. In fact, the absence of free arms when single subunits bind to F-actin supports the hypothesis that subunits bind along F-actin rather than just at the ABD.

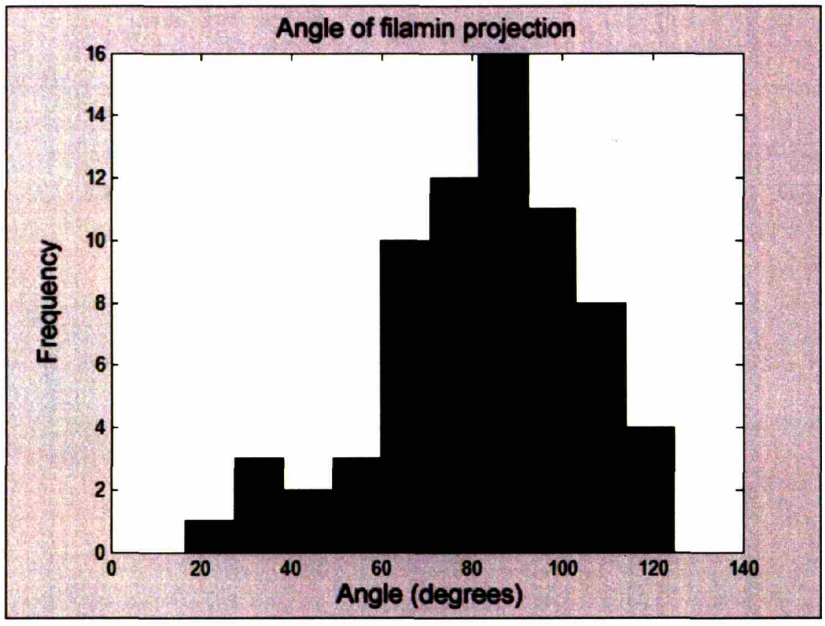

Figure 5.10 The angle distribution of the projecting segment of filamin has a mean of 71.8 degrees and standard deviation of 15.5 degrees (N=70). For these statistics, angles A above 90 degrees are measured as their acute angle (180-A) due to symmetry. Future work could examine the filamin angle for the full 180 degrees relative to the polarity of actin.

Figure 5.11 Schematic representation of two interpretations of the data in Figure 5.8. The yellow filamin molecule on the left is attached along one subunit and projects the second subunit from the F-actin (red). The single filamin subunit on the right is attached at its ABD (green) to F-actin and has a similar projection.

5.3 The rotational stiffness of filamin

The variation of the angle between the two filamin subunits gives an indication of the stiffness of molecule. If filamin is a rigid molecule, it should retain the same shape from molecule to molecule. If, on the other hand, filamin's subunit angle varies greatly, then there is little resistance to deformation and the rotational or torsional stiffness, k_T, is low.

Measurements are made on filamin molecules in dilute solution, bound to a single actin filament. If the filamin molecules are incorporated into an actin network, their motion is constrained and their variability does not reflect the stiffness of single filamin molecules.

Result 10: Filamin's stiffness is comparable to other binding proteins

From the equipartition theorem, the torsional stiffness, k_T, is related to the variance in the junction angle, θ, according to

$$(5.1) \qquad <\theta^2> = \frac{k_B T}{k_T}$$

where T is the temperature and k_B is Boltzmann's constant.

From Figure 5.10, the variance of the angle is measured to be $(15.5°)^2$ or $0.07\ \text{rad}^2$, which yields

$$(5.2) \qquad k_T = 0.6 \times 10^{-19}\ \text{N·m}$$

if $T = 300\text{K}$ and $k_B = 1.38 \times 10^{-23}$ N·m/K. This value is comparable to the reported value for Arp2/3, another large-angle structural actin-cross-linker, 0.8×10^{-19} N·m[177].

5.4 Hingeless filamin

Actin networks cross-linked by hingeless filamin, FLNa(ΔH1), are less stiff than networks cross-linked by hinged filamin. In addition, in contrast to hinged filamin actin networks, hingeless filamin actin networks exhibit no strain hardening, have a strong frequency dependence, exhibit significant creep, and do not recover from strain[32]. Molecules of hingeless filamin (in the presence and absence of F-actin) were observed in the electron microscope to determine if there are differences between hingeless and hinged filamin in structure or binding.

Result 11: Hinge 1 deletion does not affect filamin contour

The term "hinge" has been used to describe the amino acid interruption between repeats 15 and 16. Removing this insertion has significant impact decreasing the stiffness of actin networks under stress [32]. Removal of a hinge would seem to strengthen the molecule making it a better

cross-linker; however, if the molecule loses compliance, it may detach or break more quickly. In order to assist the interpretation of these hypotheses, the hingeless molecule was examined directly. As can be seen in Figure 5.12, the contour shape is indistinguishable from that of hinged filamin shown in Figure 5.1, while the length is somewhat lower (130.6 ± 23.1 nm). The persistence length of hingeless filamin is 10.6 ± 7.4 nm, which is certainly not more stiff than hinged filamin.

Visual inspection of these molecules shows that the subunit is not straighter than in the wild-type molecule, as might be expected after deletion of a hinge. However, the molecules are unperturbed in this experiment, and they might respond differently from wild-type filamin when placed under stress or strain or incorporated into a network. Static, *in vitro* actin networks cross-linked by either of the two variants of filamin have similar morphologies when examined in the electron microscope (data not shown), so the impact of the hinge might be relevant only when the networks are under stress.

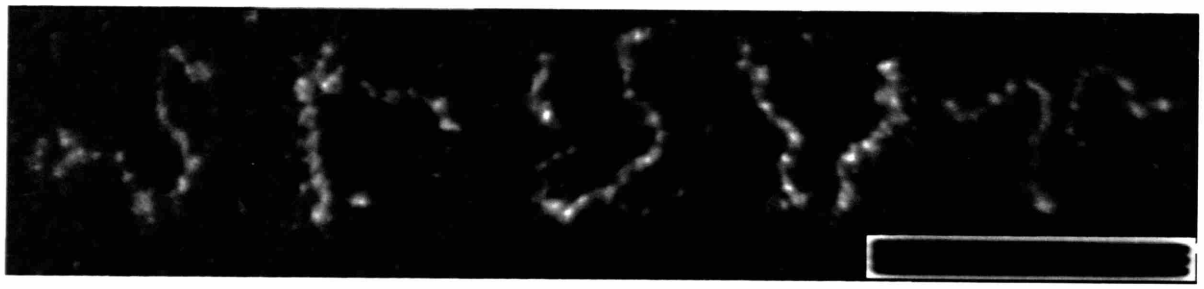

Figure 5.12 Representative images of hingeless filamin obtained by the glycerol spraying method described in Chapter 3. The molecules are approximately 130 nm long (130.6 ± 23.1 nm) and have a persistence length of 10.6 ± 7.4 nm (N=17). Bar, 100 nm.

Result 12: Hinge 1 deletion does not affect filamin hang

One possible mechanism for filamin's binding to actin that would explain full-subunit binding and explain a purpose for the insertion is that the insertion binds actin. There is precedent for this mechanism in the protein titin, which has a repeat structure similar to filamin's and contains an insertion that binds actin. To test this mechanism, hingeless filamin was mixed with actin and examined. If the insertion provides a second attachment point for each subunit, filamin lacking this insertion should have its entire contour project from F-actin. As seen below in Figure 5.13, this is not the case: the hingeless filamin extends 50-80 nm just as wild-type filamin does.

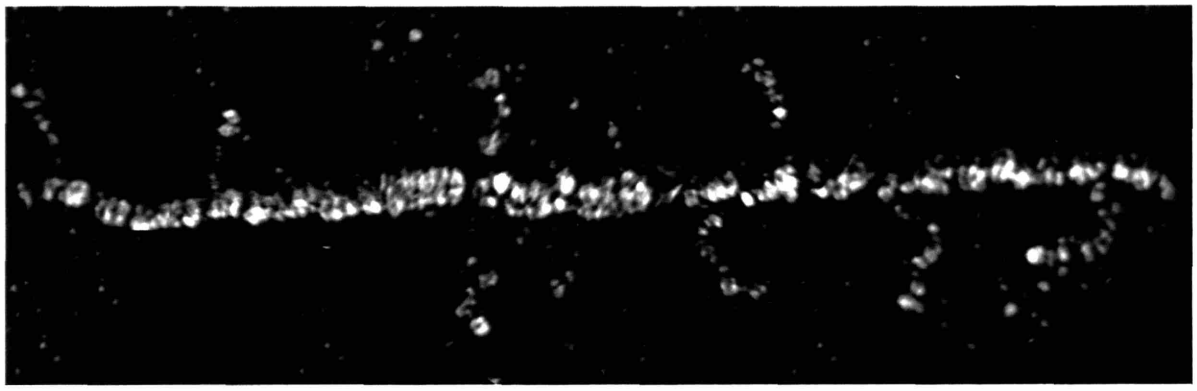

Figure 5.13 Composite of hingeless filamin molecules projecting from actin filaments observed by electron microscopy. The molecules are thinner than actin filaments and vary in length from 50-80 nm, which supports the hypothesis that each of these projections is a single subunit of filamin. There is no noticeable difference between wild-type and hingeless filamin.

5.5 Controls

A control system with the target protein knocked out simultaneously tests primary antibody specificity, secondary antibody specificity, and each step of the protocol. For filamin, the A7 and M2 cell lines are used as controls. As described in Chapter 2, the M2 cell line is a human melanoma line that naturally lacks filamin A. The A7 cell line is the same line rescued with filamin A. As such, the two lines are identical except for filamin A expression.

As shown in Figure 5.14, immunofluorescence analysis reveals that the anti-filamin monoclonals label A7 cells specifically. The standard protocol for immunofluorescence uses formaldehyde as a fixative, whereas electron microscopy, which requires preservation of the fine cytoskeletal structure, traditionally uses the stronger glutaraldehyde. A disadvantage of stronger fixative is that it has the potential to cover and mask the target epitopes, glutaraldehyding them, as it were. For this reason, formaldehyde was used for this thesis, as described in Chapter 3.

To confirm that the antibodies were binding to filamin specifically, the antibodies were tested with a Western blot against filamin A as well as against A7 lysate. As shown in Figure 5.15, the antibodies are specific to filamin A.

Each control protocol is unique and may produce different results. Filamin passed through an SDS-PAGE gel may provide a different target for antibodies than filamin fixed to the cytoskeleton. Also, each system uses different secondary antibodies, each of which has a different label. Immunofluorescence secondaries are conjugated to fluorophores, Western Blot

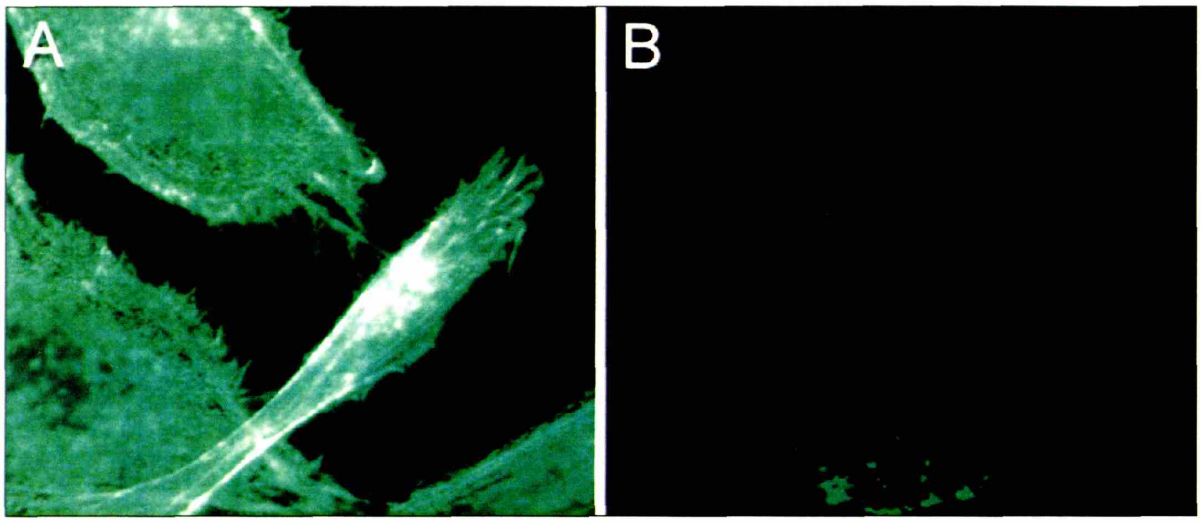

Figure 5.14 Immunofluorescent confirmation of antibody specificity. A, Formaldehyde-fixed A7 cells incubated with anti-filamin mAb 1.2 and then with secondary anti-mouse antibodies attached to a fluorescent dye. Cells are labeled brightly when the dye is excited. B, M2 cells with the same treatment. Only a small amount of background noise is visible.

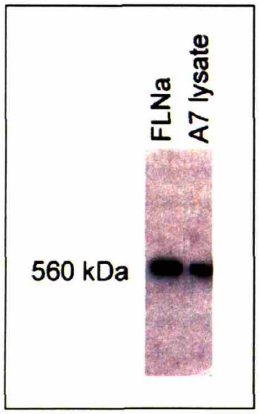

Figure 5.15 Western blot confirmation that the monoclonal antibodies bind filamin A, and only filamin A, in cells. The samples were run down an 8% SDS-PAGE gel and transferred to a PVDF membrane. The membranes were blocked with 3% BSA, incubated with the monoclonal antibodies, blocked again, and incubated with secondary anti-mouse antibodies conjugated to horseradish peroxidase. The peroxidase was activated and film was exposed to the signal. Shown is mAb 1.2.

secondaries are conjugated to horseradish peroxidase, and EM secondaries are conjugated to gold particles. While immunofluorescence confirms that the primary antibodies are specific, it does not confirm that the gold-conjugated secondary antibodies are functional. To confirm that the EM protocol in its entirety, including fixation, blocking, and washing, is successful, the antibodies are tested in A7 and M2 cells prepared in parallel for EM.

Figure 5.16 illustrates that the EM immunogold protocol is specific for filamin. A7 cells contain disperse labeling throughout the cytoskeleton, whereas M2 cells lack labeling entirely. The labeling in A7 cells is situated along F-actin and near junctions, with no background gold on the coverslip.

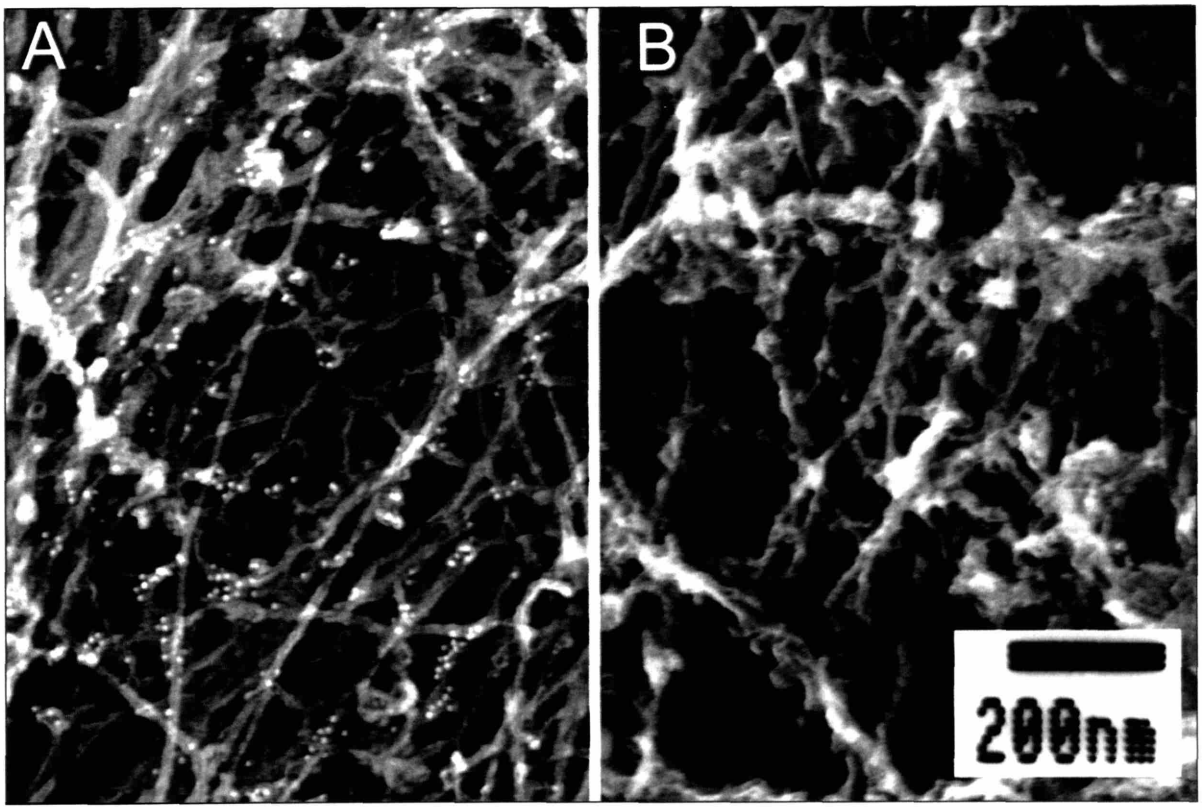

Figure 5.16 Confirmation that the labeling protocol is specific for filamin A. A, An A7 cell (containing filamin A) shows widespread gold labeling along F-actin and near junctions. B, An M2 cell (lacking filamin A) shows no gold labeling. Both cells were extracted with Triton-X100, fixed with 4% formaldehyde, and blocked with 1% BSA.

Chapter 6 Discussion

A structural F-actin cross-linking protein should efficiently organize network structure. Filamin converts actin into gels at a lower concentration than other binding proteins do [77, 85]. This thesis demonstrates that filamin has a unique combination of physical characteristics that have not been reported in other actin-binding proteins. Filamin is a long flexible molecule, yet it forms consistent, orthogonal junctions. It has only two known actin-binding sites, yet images consistently show it to bind along distances of 80 nm which would bring F-actin into close arrangement. In this chapter, interpretations of the physical findings of the previous chapter explain the potency of filamin as an actin-cross-linker.

6.1 The structure of filamin

Long arms can increase filamin on-rate

A first requirement of a cross-linker is that it has two or more binding sites for its target protein. The distance between the binding sites of the cross-linker determines how frequently it encounters its target protein, particularly if the target protein has low mobility like entangled F-actin. Filamin molecules, with 80 nm arms terminating in high affinity actin-binding sites [136], can sample a greater space for F-actin than a shorter molecule like α-actinin. This may be more important with large target molecules like actin filaments which sterically interfere with and exclude each other.

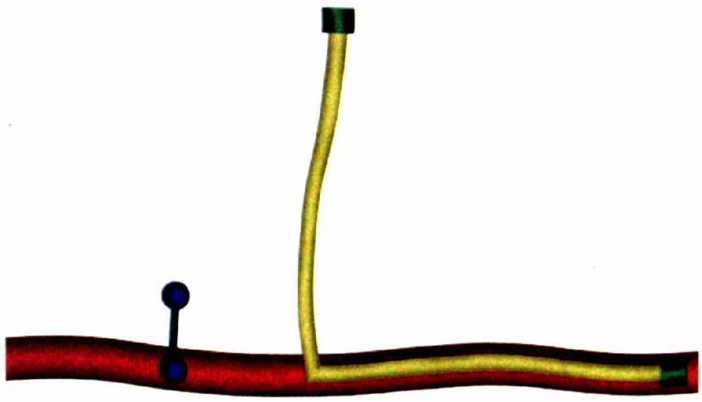

Figure 6.1 The lengthy, flexible filamin subunit (yellow) is advantageous for locating and binding actin filaments. Compared to a short, stiff molecule like α-actinin (blue) the filamin subunit can sample a greater volume and is more likely to encounter its target.

Flexible subunits can increase filamin on-rate

The flexibility of a cross-linker enhances its on-rate. A rigid cross-linker subunit at a rigid angle can only sample one spot relative to the actin filament to which it is attached. By comparison, a long rigid subunit extending from a flexible joint can sample the locus of points one subunit-length away from its attachment point. This spherical shell is an improvement over a single point. A long flexible subunit offers the greatest advantage: it can sample the entire volume of the sphere, as shown in Figure 6.1. Hence the flexibility of an unbound filamin subunit contributes to its gelation efficacy.

A completely flexible cross-linker should act as a tether (a translational constraint). However, filamin organizes F-actin in perpendicular junctions, which is inconsistent with a translational constraint. A potential non-structural explanation of actin perpendicularity is electrostatic repulsion: if like-charged actin filaments repel each other but are bound together, an orthogonal orientation is a low-energy configuration. However, in physiological buffers free ions negate electric fields at a distance greater than 1 nm [188] (the Debye length) so this effect is not plausible at typical F-actin separations (10-1000 nm).

Rigid self-association region imparts large angle to F-actin junction

The rigid self-association region with a defined geometry is a key component of the molecule. Barring a major conformation change in filamin upon attachment to F-actin, the self-association region appears to be the likely mechanism by which filamin can cross-link actin into large-angle junctions. A consequence of this finding is that N-terminal ABDs are not sufficient for junction orthogonality. The flexible filamin subunit between each actin filament and the stiff self-association region decouples the filamin stiffness from the junction stiffness. For this structured domain of the filamin molecule to impart its rigidity to an actin junction, the actin must bind near the C-terminal self-association region. This is strong indirect evidence that actin must bind along the length of the filamin.

6.2 Advantages of multiple-site binding

These findings suggest that filamin does not bind to F-actin solely at N-terminal ABDs, as is currently believed, but rather has other domains that bind along an actin filament. Contours of filamin molecules indicate that the molecule is too flexible to impart rigidity if only bound at the N-termini. Moreover, filamin molecules bound along a single actin filament are rarely observed with 160 nm contour length as would be expected if only N-terminal ABDs bind to F-actin, and instead are frequently hanging off the filaments as flexible chains having 80 nm contour length – as would be expected if one subunit of filamin bound at multiple sites to F-actin. This suggests the rods have affinity for F-actin. Filamin likely binds like a zipper, attaching at its N-terminus first, and then binding along its subunit while the actin is constrained from moving away. As

such, the primary N-terminal ABD is a critical binding site which needs to bind actin alone without assistance from neighboring secondary binding sites. Sites near the rigid self-association domain also need to be strong, as F-actin will pull against filamin most strongly at the junction.

Stronger binding

There are several ramifications for full-subunit finding. There is an additive effect in which each additional bond would increase the separation force required to remove filamin. This effect is a cooperative. In order to separate the molecules, each bond must be broken simultaneously. For forces that that are small and random, like thermal undulations, an occasional bond breakage will not release the filamin. It is likely that the unbound site will reattach, especially when held in position by the other binding sites, before all other sites also encounter a significant random force simultaneously and unbinding. This may explain the finding of Wachsstock [87, 88] that filamin has a lower disassociation constant than some forms of α-actinin, despite the noted similarity of their primary ABDs.

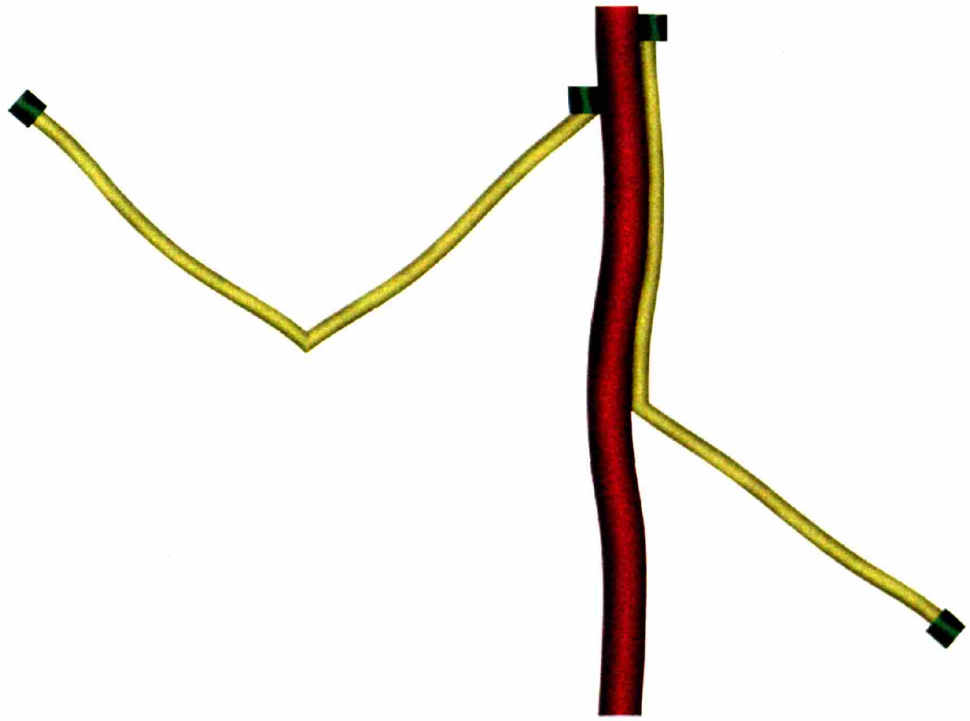

Figure 6.2 There is a tradeoff between sampling volume and binding stability. The molecule which only binds its N terminus (left) samples a great space, but the molecule that binds fully along its subunit (right) is more stably bound to actin. Not only do more binding sites indicate a greater strength by direct addition, they also reduce the probability of chance detachment: the molecule will not disassociate unless all sites detach simultaneously which is increasing unlikely as the number of sites increases. The pore size of actin filament networks in cells is on the order of one subunit length, so one free subunit should be sufficient for locating actin.

Tight junctions increase stiffness

As discussed in Chapter 1, the stiffness of networks is a function of constraint. Steel beams are quite stiff, but a structure of steel beams bound by long pieces of slack rope is not rigid. The ropes do not constrain the relative motion of the beams. If the beams are instead held together by tight steel bolts which prevent the beams from sliding or rotating relative to each other, the structure is rigid. For an enthalpic structure of beams, this dependence is intuitive.

For entropic structures, the same principles hold. Even in the absence of cross-linking, networks of long semi-flexible polymers achieve stiffness through entanglements because these entanglements constrain the motion of the polymers. Current entropic models of semi-flexible polymers (bending and straightening) are based on the physical constraints polymers place on each other. If the motion of adjacent polymers is coupled, the polymers not only resist deformation themselves, but their interactions also resist deformation. The degree of steric coupling determines the network stiffness.

One drawback of elongated cross-linkers such as filamin, then, is loose network formation. A tether constrains motion by preventing filaments from moving away from one another, preventing filaments from sliding past one another, and if sufficiently large, a tether can get entangled itself, adding another polymer species to the network. However, the shorter the tether, the greater each of these constraints becomes. The closer two polymers are to another, the more coupled their behavior.

Thus, filamin, as a long flexible molecule, would be at a disadvantage to short molecules like α-actinin in strengthening actin networks. However, filamin removes this disadvantage by binding along its subunit such that the actin is bound near the self-association region. Like a zipper, it pulls the two pieces together, and produces a junction that is more tightly constrained, as shown in Figure 6.3. The two binding modalities would likely form very different networks, but as a first estimate of the effect on network stiffness, the loose junction shown on the left can be modeled as adding a ~100 nm distance between "entangled" actin filaments, increasing the entanglement length, ξ, from ~100 nm to ~200 nm. In an entropic bending model in which polymers get pulled straight by applied forces, the network stiffness is proportional to ξ^{-2} to ξ^{-5} depending on junction architecture [81], so the network stiffness could drop by a factor of 30. The effect could be more dramatic due to the impact on other modes of deformation, such as the complete elimination of reptation in the right side of Figure 6.3.

Large junction angles create disperse networks

An intuitive mechanism by which the self-association region will increase network stiffness is by direct reinforcement of junctions, enthalpically. Similar to the manner in which metal braces reinforce roof trusses, the filamin molecule can brace the actin junction and add additional torsional resistance to deformation. As forces are applied to the lattice, the intersections begin to

deform but the filamin resists this deformation. This network deformation can be calculated directly by constructing a model of a structure of F-actin elements with torsional springs at each junction. The torsional stiffness of filamin was calculated in Section 5.3 to be 0.6×10^{-19} N·m, and such a model[188] predicts a cytoskeletal stiffness of 300 Pa when the concentration of actin is 10 mg/ml.

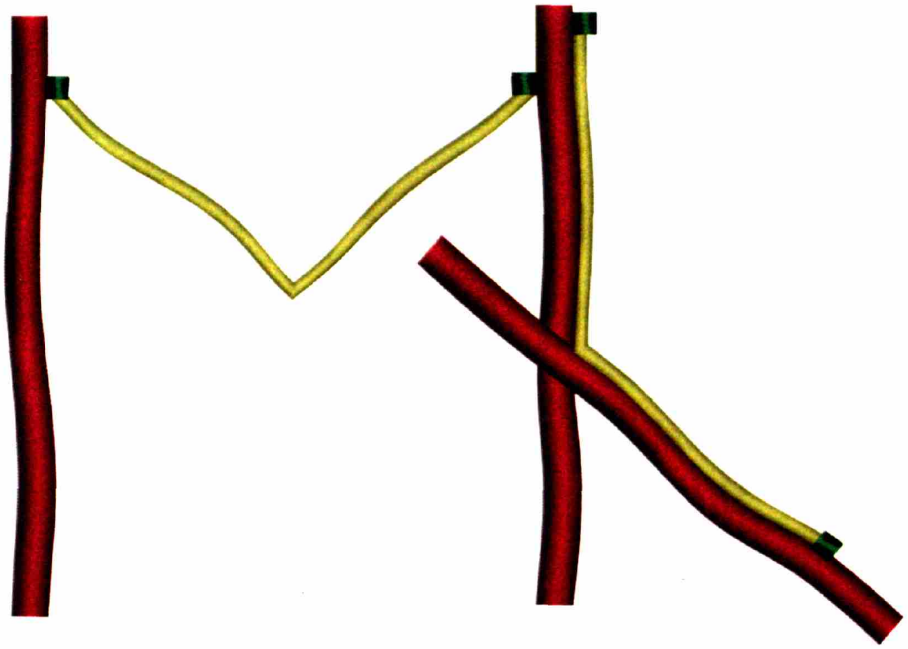

Figure 6.3 The stiffness of a polymer network is related to the proximity of its elements. Because energy is distributed by thermal undulations and reptation of filaments, widely spaced junctions (left) will produce a less-stiff network. The filaments are essentially uncoupled. Tight junctions (right), on the other hand, more tightly pin the filaments together, requiring greater force to deform the network by displacing filaments relative to one another.

In an entropic model, the geometry of filamin can also have a significant impact on network stiffness by altering the formation of the network itself. A closely packed group of long elements will orient themselves in a parallel array to satisfy energy and entropy constraints, explaining why short binding proteins such as α-actinin serve as bundling proteins. This leads to a tradeoff: tight junctions advantageously make a distributed polymer network stiffer, but the short binding proteins with the ability to form these tight junctions will create dense bundles.

The stiff self-association region of filamin circumvents this tradeoff, as shown in Figure 6.4. When filamin cross-links two actin filaments tightly, the large-angle self-association region prevents them from aligning in parallel. In so doing, it initiates a homogeneous network that is

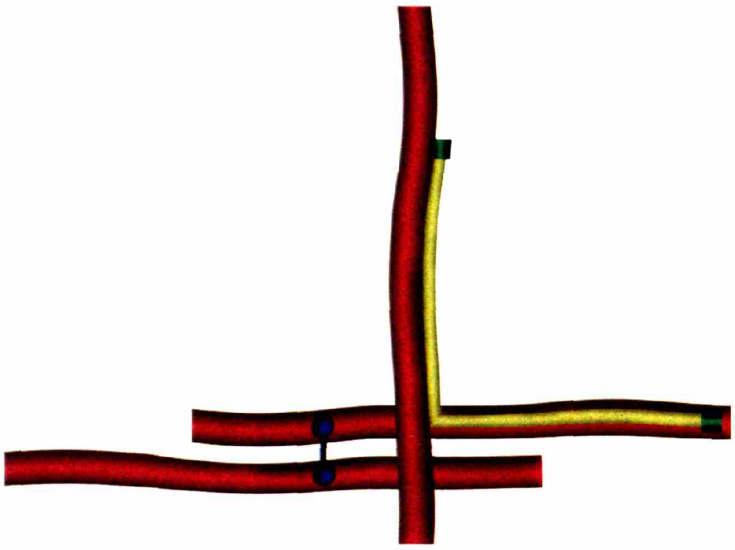

Figure 6.4 Long-subunit orthogonality prevents the bundling that results from tight junctions. For a molecule like α-actinin (blue) the close proximity of actin filaments thermodynamically forces them into parallel arrays. A molecule with a large angle like filamin (yellow) prevents this bundling while still permitting a tight junction.

three-dimensionally disperse, fills a great volume with low protein concentrations, and is permeable to molecules in the cell. The "bundling concentration" of F-actin is 2.5 mg/ml [189], while the concentration of actin in cells is 10-20 mg/ml [26], so this bundle prevention is critical for the creation of distributed networks evident in cells at such high concentrations of actin.

By branching off from actin at a large angle, filamin also reduces the chances its second N-terminal binding sites attaches to the same actin filamin. Clearly, a filamin molecule bound twice to the same filament does not contribute to network stiffness. The percentage of filamin molecules completely bound to a single actin filament is not known, but can be determined with the gold labeling system described in Chapter 3.

6.3 The environment of an actin junction

In order to understand the influence of filamin on a junction, and by extension the network, the relevant forces acting on the junction must be examined.

Cytoskeletal proteins are constantly colliding with water molecules. This thermal agitation, termed Brownian motion, causes the filaments to diffuse and fluctuate. Even though the net force is zero, over short time and length scales large forces are imparted.

Motor proteins generate force on cytoskeletal proteins by propelling proteins and organelles along filaments, or by propelling filaments themselves [190].

Forces are transmitted from the environment. Blood flow shears endothelial cells. The pulsatile nature of blood flow stretches endothelial cells lining arteries every second [191]. Hydrostatic force is transmitted to endothelial cells from blood pressure [192].

Examining Brownian, cellular, and shear forces in more detail provides a conceptual framework for understanding the environment of a single actin junction.

Brownian force

Let *F(t)* be the thermal force acting on a molecule due to collisions with surrounding solvent molecules, comprising brief impulses with random direction, occurring at random times. The equation of motion of the molecule in response to this force is

$$m\frac{d^2x}{dt^2}(t)+\gamma\frac{dx}{dt}(t)+\kappa x(t)=F(t) \tag{6.1}$$

known as the Langevin equation [193] and reviewed in [92]. m is the mass of the molecule, γ is the drag coefficient of the molecule, and k is the spring constant of the system. Because the thermal force is random, the solution is a description of the statistical properties of the resulting motion. These properties are described by the auto-correlation function, $R_x(\tau)$, of the position $x(t)$ of a molecule, which is defined by

$$R_x(\tau)=\langle x(t)\cdot x(t-\tau)\rangle \equiv \lim_{T\to\infty}\left\{\frac{1}{T}\int_{-T/2}^{T/2} x(t)x(t-\tau)\cdot dt\right\} \tag{6.2}$$

The autocorrelation at delay τ is calculated by multiplying the position at a given time t by the position at time τ earlier, and averaging over all times t.

This autocorrelation function satisfies the equation of motion because it can be shown [92] that

$$m\frac{d^2R_x}{d\tau^2}(\tau)+\gamma\frac{dR_x}{d\tau}(\tau)+\kappa R_x(\tau)=0\ ; \qquad \tau>0 \tag{6.3}$$

In the case of overdamped motion appropriate for protein dynamics, this equation yields an autocorrelation function that is the sum of two exponentials, a fast, small-amplitude one with time constant m/γ and a slow, large-amplitude one with a time constant γ/κ [92]. Figure 6.5 shows

a globular protein suspended in aqueous media, driven only by Brownian forces and obeying the Langevin equation.

Monomeric actin (42 kDa) has mass per monomer

(6.4) $$m = 70 \times 10^{-24} \text{ kg}$$

so the root-mean-square speed of this molecule in 37°C solution is

(6.5) $$v_{rms} = \sqrt{3kT/m} \approx 13 \text{ m/s}$$

In 37°C water (η=0.7 mPa·s), the damping for a globular protein with radius 3 nm is

(6.6) $$\gamma = 6\pi\eta r \approx 30 \text{ pN} \cdot \text{s/m}$$

Thus,

(6.7) $$F_{rms} = \gamma v_{rms} \approx 420 \text{ pN}$$

From the Langevin equation, the time constant for Brownian motion is

(6.8) $$\tau_{inertial} = m/\gamma \approx 2 \text{ ps}$$

This represents the correlation, or persistence, time of the velocity – the approximate length of time between changes in direction due to bombardment. Given the seemingly high velocity 13 m/s, in this time the monomer travels only a distance

(6.9) $$d = vt \approx 0.03 \text{ nm}$$

which is 1% of the radius of the actin monomer. Even though the speed of the monomer is great relative to its size, the high degree of damping from the surrounding water molecules means that inertia carries the monomer only short distances before the monomer changes direction.

If an actin monomer is bound by a molecular spring as shown in Figure 6.6, the Langevin equation yields the rms position of the molecule

(6.10) $$x_{rms} = \sqrt{\langle x^2 \rangle} = \sqrt{kT/\kappa}$$

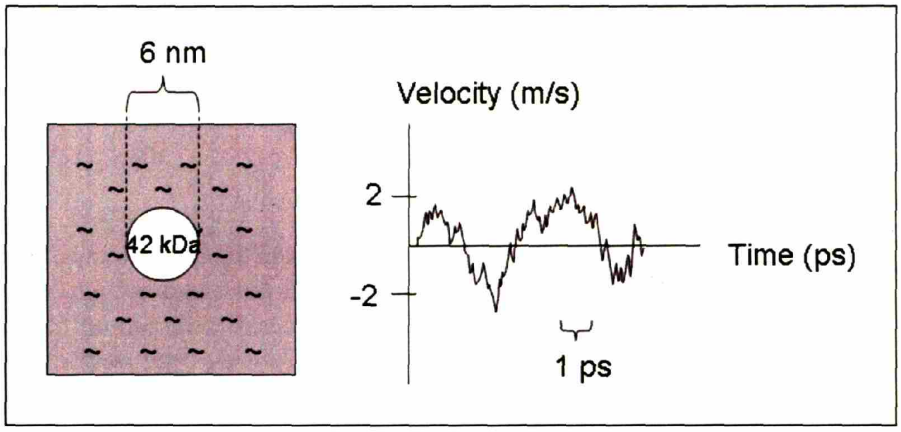

Figure 6.5 Schematic representation of a globular protein in solution (left) and its speed plotted against time (right)

This spring is a representation of a tethering protein. When one particular such protein, filamin, is stretched by a force of 100-200 pN, the repeat structure yields 30 nm [167]. The Hookean stiffness, κ, of the weaker repeats of filamin is approximately 3 pN/nm, producing

(6.11) $$x_{rms} \approx 1 \text{ nm}$$

which is independent of mass and shape.

The persistence time for this motion is

(6.12) $$\tau_{elastic} = \gamma / \kappa \approx 10 \text{ ns}$$

which is ~5,000 times longer than the inertial time constant. For times less than 10 ns, the actin molecule will be near where it started. For times >> 10 ns, the particle's position is uncorrelated.

If the actin monomer is replaced by an actin filament, the mass and drag coefficient change, but the equation of motion remains the same. In particular, a 1 μm actin filament (370 monomers, diameter 7 nm) has mass

(6.13) $$m = 26400 \times 10^{-24} \text{ kg}$$

and drag coefficients

(6.14)
$$\gamma_{\parallel} = \frac{2\pi\eta L}{\ln(L/2r) - 0.20} \approx 1300 \text{ pN}\cdot\text{s/m}$$
$$\gamma_{\perp} = \frac{4\pi\eta L}{\ln(L/2r) + 0.84} \approx 1900 \text{ pN}\cdot\text{s/m}$$

which are approximately 50 times the drag on a monomer.

With these values, the motion parameters for a freely moving rod-like filament are

(6.15)
$$v_{rms} = \sqrt{3kT/m} \approx 0.7 \text{ m/s}$$
$$F_{rms} = \gamma v_{rms} \approx 1100 \text{ pN}$$
$$\tau_{inertial} = m/\gamma \approx 15 \text{ ps}$$

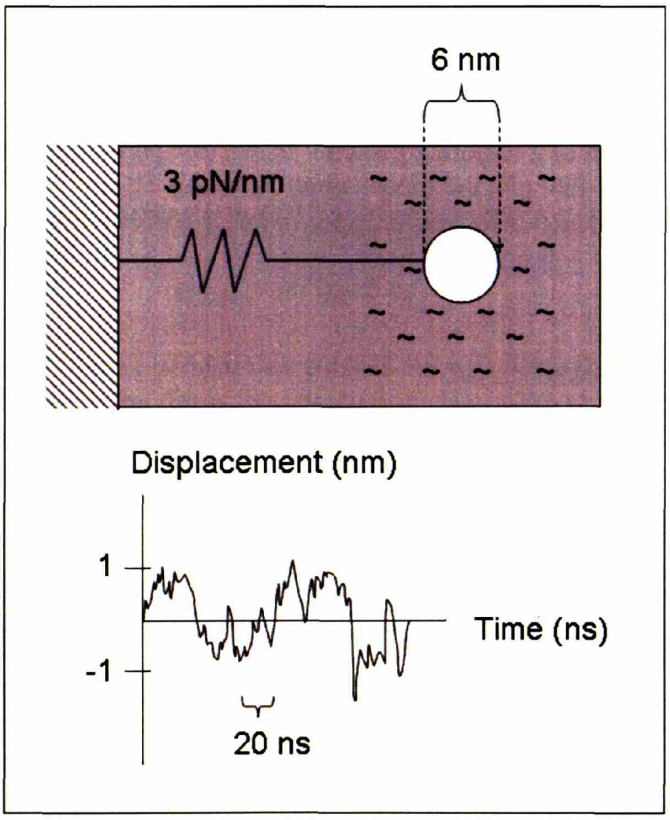

Figure 6.6 Schematic representation of a globular protein bound to a tether protein (top) and its displacement plotted against time (bottom).

Examining a filament bound by filamin, shown in Figure 6.7, the motion parameters are

(6.16)
$$x_{rms} = \sqrt{kT/\kappa} \approx 1 \text{ nm}$$
$$\tau_{elastic} = \gamma/\kappa \approx 500 \text{ ns}$$

So while the force exerted on an actin filament is large, the distance it moves while tethered is small. The effective force exerted by the buffeted F-actin on filamin to stretch it 1 nm, i.e. the "Brownian force" on the cross-linker, is 1-3 pN. Considering the separate motion of both actin filaments in a junction, the forces on the cross-linker could be two-fold higher at times.

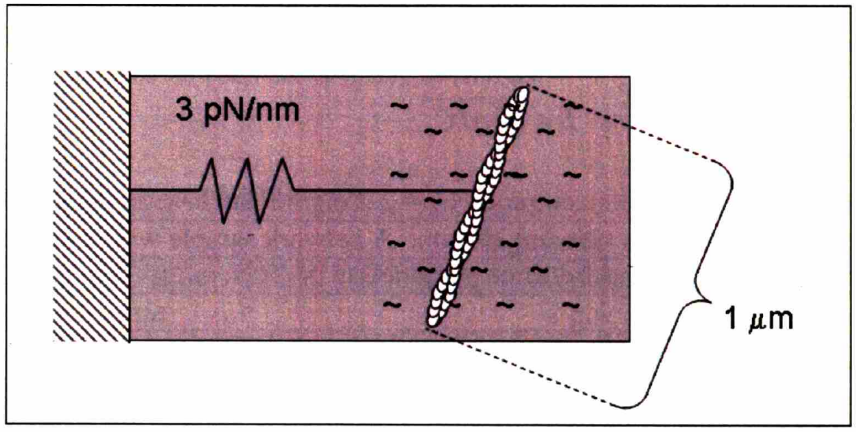

Figure 6.7 Schematic representation of an actin filament bound to a tether protein. System not drawn to scale.

Cellular force

The actin-myosin system provides a model of cellular force magnitudes. A laser trap assay measures force and displacement produced by single myosin molecules interacting with an actin filament suspended in solution [194] and the average force is 4 pN [195].

Actin generates force while it polymerizes. This force is partially responsible for the protrusion of the membrane at the leading edge of a motile cell and it propels some bacteria via their actin-based "comet" tail. In sea cucumbers, actin polymerization extends the sperm acrosome 90 microns in just 10 seconds [196]. The maximum force for a polymerizing filament is dependent

on the monomer size and the ratio of monomer concentration to critical concentration. For actin, where the latter ratio is 100, the polymerizing force can be as high as 7 pN [92], enough to buckle a filament longer than 300 nm. Microtubules have been measured to push on a barrier at 4 pN [197].

Shear force

Blood passing over the endothelial lining of vessels exposes the cellular network to approximately 10 dynes/cm^2 (1 Pa) shear force [4]. Assuming a pore size of 100 nm, this shear corresponds to a uniformly distributed force of 0.01 pN per junction, which is about 3 orders of magnitude below the binding strength of actin cross-linkers. This assumes that every junction is regulated by one filamin molecule. While not every filamin molecule is bound at a given time, unbound junctions contribute to force dissipation through entanglements and steric interactions.

For *in vitro* experiments, imposed shear stresses are higher than physiological, on the order of 20 Pa [33]. The pore size is related to the concentration according to

$$L = \sqrt{3\rho / C_a} \tag{6.17}$$

Using a lower-than-physiological concentration C_a = 2.2 mg/ml and F-actin linear mass density $\rho = 2.64 \times 10^{-14}$ kg/m yields a pore size L = 200 nm. A network sample with these parameters and the higher shear force experiences a force per junction of 1 pN.

An alternate estimate of the force per filamin molecule can be determined from the concentration of filamin rather than the network geometry. For an experimental shear chamber 50 mm × 10 mm × 1 mm, the volume, V, is 500 µl and the area, A, exposed to shear is 5×10^{-10} m^2. For filamin concentration, C_f, 0.25 µM, the number of filamin in the volume ($C_f \times$ Avogadro's number × V) is 7.5×10^{13} molecules, and the total shear force ($\tau \times A$) is 0.01 N, assuming shear stress τ = 20 Pa. The average force per filamin is 0.1 fN. This is orders lower than the above estimates because it assumes all filamin in the sample act in parallel to offset the force; the estimates above assume there are many planes of junctions that act in series such that each junction experiences force $F = \tau L^2$.

• • •

From these calculations, summarized in Table 6.1, and the filamin biophysical data reported in Section 2.3, a number of findings are suggested.

Filamin will detach before it completely unfolds. The binding strength is only about 20 pN whereas the unfolding force is about 100 pN. For forces lower than 20 pN, filamin will stretch

like a spring with k ~ 3 pN/nm as its weakest repeats start to pull out. At forces greater than 20 pN, the ABDs will release.

The shear force exerted on junctions in the cell is negligible compared to the other forces in the cell and to the protein strengths. However, the lack of network compliance indicates this force will be transmitted all the way to the base of the cell and important signaling molecules there.

Occasionally the Brownian motion of actin filaments will be sufficient to detach cross- linking proteins. Additionally, due to its random direction, the Brownian force can either add to or subtract from applied forces on junctions, thereby reducing or increasing the energy well of binding, alternately weakening and strengthening cross-links.

The protein forces generated within the cell are strong enough to occasionally disrupt cross-links. The force of a single myosin motor or a single polymerizing actin filament is equivalent to the weaker binding states of actin-binding proteins. If multiple motors are bound to a single filament, the force on the cross-linker increases, while if the F-actin in tension is cross-linked in several locations, the force on each cross-linker decreases.

Table 6.1 Summary of relevant force scales in cells.

Force	Magnitude	Reference
Brownian, cross-linked F-actin	3 pN	Here
Tension, myosin on F-actin	4 pN	[195]
Compression, actin or microtubule polymerization	7 pN	[92]
Shear, per junction	0.1 pN	Here
Breakage, actin in tension	100 – 200 pN	[198]
Unfolding, filamin	50 – 200 pN	[167]
Binding, α-actinin to F-actin	1-50 pN	[164]

6.4 Junction ramifications

The results of this thesis imply filamin can serve two roles as a cross-linker. It functions as a brace that strengthens junctions, or it serves as a pin that constrains junctions, or both. A role as a 150 nm flexible tether is ruled out. The variation in the junctional angle implies filamin serves primarily as a pin. It may serve an additional stabilizing role, but the chief purpose seems to be binding two filaments in close proximity, correlating their motion.

Translational deformation of a filamin pin

No physical material can be an idealized zero-deformation pin, including filamin. Filamin is elastic and deforms under force. The extent of this deformation provides insight into the dynamics of cross-linked junctions.

The flexibility of the weakest filamin repeats is approximately $k_{filamin}$ = 3 pN/nm [167]. This is a conservative estimate, as contour analysis indicates that the self-association domain of filamin is more rigid than the N-terminal repeats (see Section 5.1). The scale of forces at junctions, including shear, Brownian motion, and protein interactions, is on the order of 5 pN (see Section 6.3). This indicates that a filamin molecule under tension at an actin junction (Figure 6.8) will yield about 2-3 nm under forces in the cell – a distance smaller than the diameter of an actin filament. Filamin may also detach if the bond is a weak bond, on the order of single pN, or if Brownian motion augments the applied force with another 5 pN.

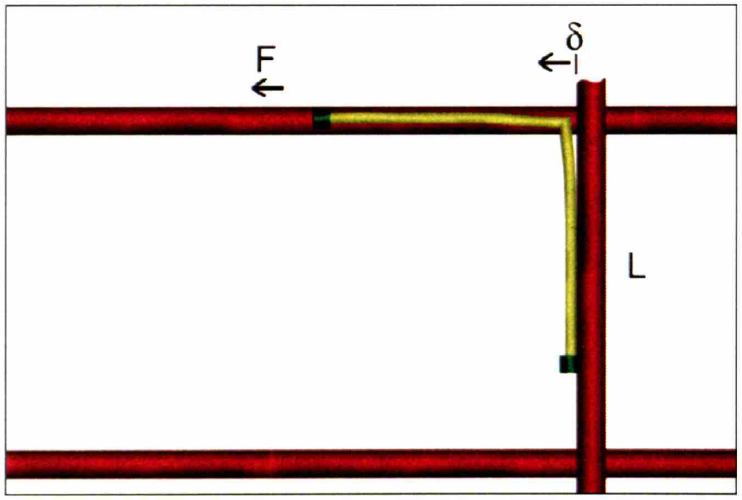

Figure 6.8 Schematic representation of a force acting on a filamin-regulated actin junction. The vertical filament is anchored to the network below, and the filamin extends 2 nm when F = 5 pN and L = 100 nm. The effective extension of filamin is shown at the self-association region for easier visualization. The extension is likely to occur within a repeat, which would not be visually perceptible in this graphic.

In order to determine whether junction deformation is limited by filamin or actin, the bending deflection of an actin filament participating in the same junction is calculated (Figure 6.9). For the free end of an actin rod, the bending flexibility is given by

(6.18) $$k = \frac{F}{\delta} = \frac{3EI}{L^3}$$

where EI represents the flexural rigidity and L represents the length. If L = 100 nm, the lower limit of pore size in the literature, and $EI = 7.3\times10^{-26}$ N·m^2 [60], k_{actin} = 0.2 pN/nm, which is an order of magnitude weaker than filamin. For forces of the order 5 pN, the actin will bend 25 nm while the filamin yields only 2 nm. For a pore size of 200 nm, the upper limit of values in the literature, the actin flexibility increases another order and the deformation is not linear.

If, instead of having a free end at the junction, the actin filament being deflected is constrained at junctions above as well as below the junction being analyzed, the bending flexibility is given by

$$k = \frac{F}{\delta} = \frac{6EI}{L^3}$$

which differs only by a factor of 2 from the previous case. Filamin is strong enough to be considered translationally "non-compliant" with respect to the cross-linking of F-actin junctions.

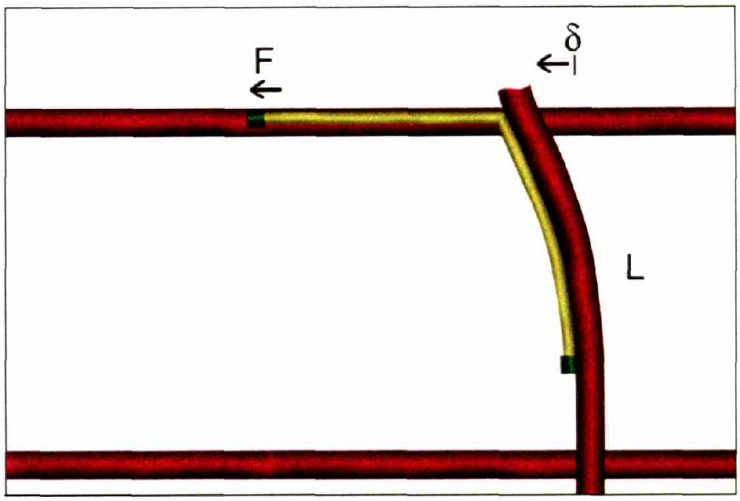

Figure 6.9 Schematic representation of a force acting on a filamin-regulated actin junction. The vertical filament is anchored to the network below and has a free top end. The actin filament bends 25 nm when F = 5 pN and L = 100 nm.

Angular deformation of a filamin brace

As determined with Brownian motion-induced angle variation analysis, the torsional stiffness of filamin is $k_T \sim 10^{-19}$ N·m, from Equation (5.2). With this spring in place as the lower constraint on an actin filament (Figure 6.10), the angular rotation of the filament as a result of an applied force can be determined. For the system,

(6.19) $$T = k_T \theta$$

where T ($= F \cdot L$) is the torque applied by the force and θ is the angle of deflection. Using a torque of $T = 5$ pN × 100 nm = 5×10^{-19} N·m and $k_T = 10^{-19}$ N·m, the angular deflection equals 5 rad, which is physically impossible. This indicates that filamin in an isolated junction is not strong enough to resist angular deformation against the forces in cells. However, when incorporated into an actin structure that is largely constrained, filamin is strong enough to give the network stiffness comparable to that measured in cells (Section 5.3).

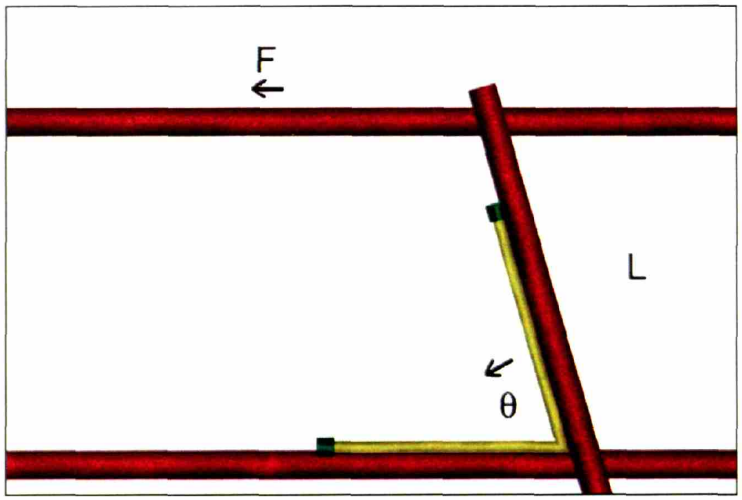

Figure 6.10 Schematic representation of a torque ($F \cdot L$) transmitted to a filamin-regulated actin junction. The rotation of the vertical filament is constrained only by the filamin, which deforms under the force.

6.5 Network ramifications

This finding that filamin is an effective pin joint supports two related models in the literature, the MacKintosh model [34] and the Gardel model [81]. The MacKintosh model is predicated on the assumption that filaments bend and writhe in solution, but that each junction binds two filaments together at a point preventing them from pulling apart, effectively a pin joint. This longitudinal constraint differs from the Isambert [63] and Morse model [53-56] for pure actin gels, which argues that lateral (tube) constraints of reptation and bending are the source of stiffness in an un-cross-linked gel. MacKintosh, et al., assume elastic restoring force is dominated by the resistance of single, fluctuating semi-flexible filaments to an applied tension that tends to straighten them. For a fully cross-linked network, the stiffness scales with actin concentration as

(6.20) $$G \sim C_a^{5/2}$$

This thesis also supports the experimental and theoretical findings of Gardel, et al., for actin networks cross-linked by scruin (see Table 1.1), a sperm-specific cross-linker which is small, "irreversible," and "non-compliant," effectively a pin joint. The stiffness of scruin-actin networks falls into two regimes. For high concentrations of actin and cross-linker, C_a and C_{XL}, respectively, thermal fluctuations give rise to stiffness with dependences

(6.21) $$G \sim C_a^{11/5} \quad \text{(theory)}$$

and

(6.22) $$G \sim C_{XL}^{2} \quad \text{(experiment)}$$

This represents an entropic origin for the network stress due to thermal fluctuations being pulled straight, rather than directed F-actin bending and cross-linker deformation. Early experiments on filamin cross-linked networks support this square-law cross-linker dependence [76, 77, 86] although the data points are few enough that curve fitting is open to interpretation.

At low protein concentrations, Gardel finds

(6.23) $$G \sim C_a^{2}$$

and the cross-linker dependence is small. The low-concentration C_a dependence mimics an enthalpic network, as discussed below.

The transition between the regimes is an inverse relationship between C_a and C_{XL}. The levels of actin and filamin typically used in *in vitro* experiments (C_a = 10-20 μM, C_f= 0.1-0.2 μM) fall along the boundary of these two regimes. It should be pointed out also that the cross-linking kinetics of filamin and scruin likely vary. Little cross-linking effect is seen at scruin concentrations below 1:100, whereas filamin has a strong effect at ratios as low as 1:1000. Filamin's extended length may position it more efficiently, as discussed above.

In addition to these two entropic models, the filamin pin constraint can be applied to a structural, enthalpic model of the cytoskeleton, such as the cellular solid model. The analysis of cellular solids is performed from a scaling perspective, such that the deflections due to bending in compression or shear are proportional to FL^3/EI.

(6.24) $$G = \frac{\tau}{\gamma} = \frac{F/A}{d/h} = \frac{F}{\delta}\frac{h}{A} \sim \frac{EI}{FL^3}\frac{1}{L} \sim \frac{1}{L^4}$$

This provides a scaling relationship

(6.25) $$G \sim C_a^2$$

No boundary conditions are specified, but the structure is strong enough to avoid collapse. If there are enough cross-links to maintain the pore size, and if there is enough irregularity in the geometry to prevent catastrophic collapse, a "pin" cross-linker is a satisfactory constraint in a beam-bending model. With more degrees of freedom than the orthogonal constraints in the original cellular solid model, pin joints may lower the stiffness of the network to physiological levels.

This model can also account for strain stiffening. While δ can be assumed to be linearly proportional to F for small deformations, the deformation of a beam quickly becomes non-linear as force increases, as shown in a computational simulation in Figure 6.11. As strain increases, stiffness increases.

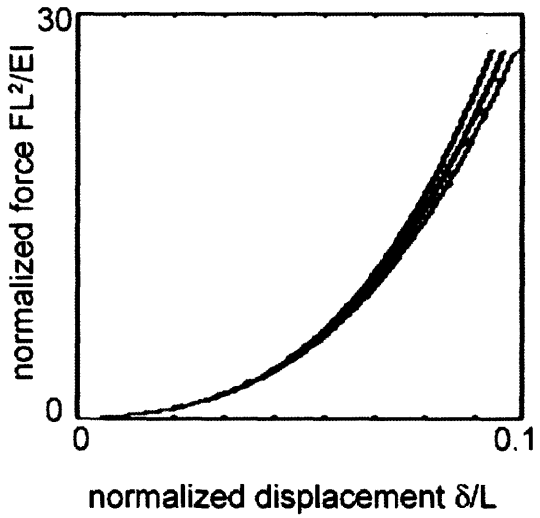

Figure 6.11 Computer simulations of the deflection of a cantilever beam. The three lines represent different computer programs. In all cases the F vs. δ relationship is non-linear and the stiffness (slope) increases with strain (adapted from [199])

A potential third model incorporating a pin junction is a geometrically-constrained network.

If a four-member truss such as the one shown in Figure 6.12 is constrained by pin joints, the structure has zero stiffness. Infinitesimal force will collapse the truss.

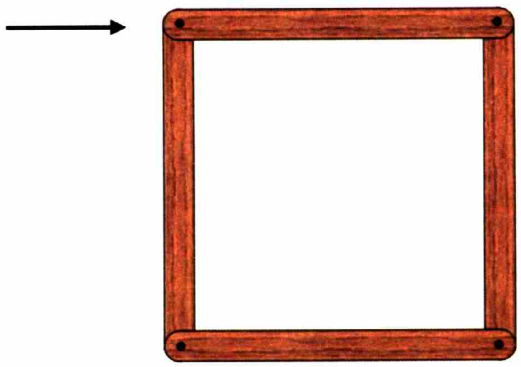

Figure 6.12 Schematic representation of a four-bar mechanism with pin joints. This structure has no in-plane stiffness; it will collapse catastrophically with the smallest horizontal force applied to the top member.

If this same structure is constrained by angle braces as shown in Figure 6.13, the structure gains stiffness. This structure can now resist deformation; the extent to which it does so is dependent on the relative stiffnesses of the elements. If the braces are weaker than the beams, the structure remains weak; if the braces are strong, the deformation of the structure depends on the stiffness of the beams bending.

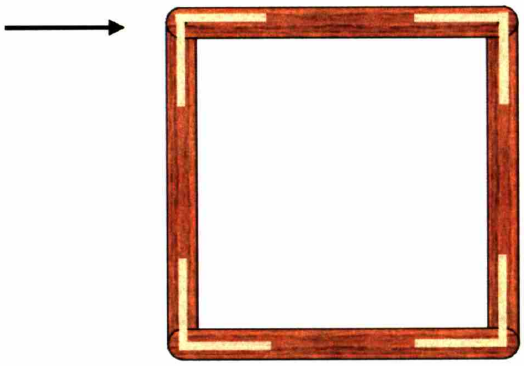

Figure 6.13 Schematic representation of a four-bar mechanism with angle braces. This structure has stiffness due to the resistance of the braces to deformation. Even a single brace would secure the structure.

However, if the structure is modified to be slightly less regular, by adding one more element as shown in Figure 6.14, the stiffness becomes much higher despite being constrained by pin joints. This stiffness increases significantly because the structure can only deform if the diagonal brace is stretched, and thin elements are much stronger in tension than in bending.

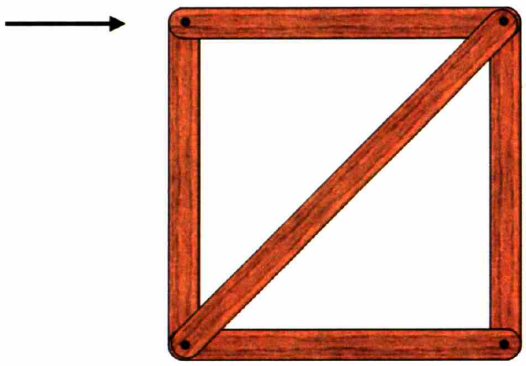

Figure 6.14 Schematic representation of a five-bar structure with pin joints. This structure has in-plane stiffness because it is over-constrained (i.e., statically indeterminate). This truss is a reasonable representation of a cytoskeletal pore; the network is complicated and has several junctions per filament and several filaments per junction.

The simplest such constrained unit is a triangle, shown in Figure 6.15:

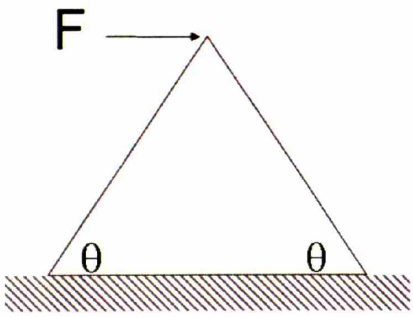

Figure 6.15 Schematic representation of a constrained structure with pin joints. A triangle is the only simple polygon which necessarily fits this class. The side elements are free to rotate, but the connection at the top prevents them from doing so freely.

For this structure, the horizontal deformation δ produced by a force F is given by

(6.26) $$\delta = \frac{FL}{4EA_c \cos^3(\theta)}$$

where L is the beam length, A_c is the beam cross-sectional area, E is the beam elastic modulus, and θ is the angle shown in the figure. Assuming the network comprises an assemblage of these units, the shear response of this unit will dictate the shear modulus of the network. The shear modulus of a structure is defined as

(6.27) $$G = \frac{\tau}{\gamma}$$

where τ represents the shear stress and γ represents the shear strain.

The force F on a junction experiencing shear stress τ is

(6.28) $$F = \tau A$$

where A is the approximate area per junction in the plane of the shear stress. If there are many junctions in a unit of area, the force on each will be smaller than if there are few junctions per unit area.

The shear strain γ is related to the horizontal deformation δ by

(6.29) $$\gamma = \frac{\delta}{h}$$

where h is the height of the structure.

Because $A \sim L^2$ and $h \sim L$, the shear response of the structure can be scaled as

(6.30) $$G = \frac{\tau}{\gamma} = \frac{F/A}{\delta/h} = \frac{F}{\delta}\frac{h}{A} \approx \frac{4EA\cos^3(\theta)}{L}\frac{1}{L} \sim \frac{1}{L^2}$$

The concentration of the beams, in this case actin, is related to the pore size, L, by

(6.31) $$C_a \sim 1/L^2$$

resulting in the relationship that

(6.32) $$G \sim C_a$$

This linear concentration dependence differs from the cellular solid model and other filament-bending models which vary as C_a^2, as well as entropic models that vary as $C_a^{2.2}$ - $C_a^{2.5}$. The mode of deformation for a structure of constrained pin joints is dependent on axial rigidity and extension rather than flexural rigidity and bending. Because bending is proportional to L^3 while extension is proportional to L, bending models are much more dependent on filament length, which is specified by pore size, which is specified by concentration.

Numerically,

$E = 2$ GPa
$A_c = 19$ nm^2
$\theta = 60°$
$L = 100$ nm
$\tau = 1$ Pa

The force on a single junction is $F = \tau L^2 = 0.01$ pN. From Equation (6.26) this produces a deformation of $\delta = 0.05$ pm, which yields an effective stiffness of $G \sim 10^6$ Pa, two orders of magnitude higher than enthalpic bending models, and several orders higher than entropic models and cell experimental data (see Figure 1.2).

This demonstrates that filamin acting as a "simple" pin constraint is more than sufficient to stabilize F-actin networks. In reality, however, the network will not be statically indeterminate. In the cell, filaments diffuse, bend, and turnover while cross-linkers attach and detach, producing a network with enough flexibility to accommodate stresses and strains.

Chapter 7 Future Work

While this thesis has provided an initial examination of how filamin binds to F-actin in the cytoskeleton and the effects of this system on cytoskeletal stiffness, a number of experiments could enhance this understanding.

7.1 Direct conjugation of anti-filamin monoclonals to gold

Conjugating the primary monoclonal antibodies to gold particles directly offers several advantages compared to using gold conjugated to anti-species secondary antibodies. First, direct conjugation shortens the physical distance between the gold marker and the target epitope. Second, direct conjugation allows for the use of differently-sized gold particles with each part of the molecule, enabling specific identification of the N- and C-termini, for example, or hinge 1 and hinge 2. Third, direct conjugation limits amplification. Anti-species antibodies can bind several times to the same primary antibody, obfuscating the filamin contour. Fourth, direct conjugation eliminates a step in the protocol, which not only saves time, but also removes an opportunity for sample loss, degradation, or contamination.

Direct conjugation was attempted with a variety of antibodies using a variety of protocols, but further investigation is warranted.

7.2 Dilute actin junction analysis

Studying filamin binding in dilute actin networks offers several advantages to using cells. One, the amount of filamin can be controlled. The abundance of filamin in cells makes it challenging to determine where one molecule may start and another end. Two, the amount of actin can be controlled. The abundance of actin in cells makes it difficult to separate junctions. Often there are 5 or 6 F-actin filaments passing near gold-labeled filamin, and making it difficult to determine which filaments are being regulated by filamin.

The challenge to studying actin networks is one of logistics. Cells adhere well to glass due to variety of adhesion molecules. F-actin binds to glass as most proteins do, but the attachment is far less strong than cells'. Strong attachment is necessary to retain the sample during the 20 buffer washes in an EM experiment. The glass is treated by glow-discharge and poly-lysine coating to increase protein adhesion, but the situation is complicated by the presence of several proteins in the protocol (actin, filamin, primary antibodies, secondary antibodies), of which only actin adhesion is desired. It is necessary to block the other proteins with BSA, but this compromises the actin adhesion too. Additionally, aldehyde fixation of the network is desired before any washes, but BSA cannot be in the solution during fixation, so there can be no blocking before fixation.

A second challenge to retaining purified actin networks is their volume. Cells are only 1 micron tall, which means they fill little of the 5 mm diameter sample droplet. Suctioning off the droplet

does not disturb the monolayer so close to the glass. Purified F-actin networks, on the other hand, fill the full volume of the 5 mm droplet. Suctioning off the droplet removes the entire network.

A third challenge is the aldehyde fixation. The network is fixed as early as possible to prevent deterioration, but if it is fixed before unbound proteins are washed away, free target proteins may adhere to the network due only to fixation and not due to natural protein binding.

Several attempts were made to study purified actin networks. These focused on three approaches to overcome the previous challenges. One, buffers were exchanged by diffusion rather than suction. A special chamber was designed to store a coverslip in a small well (0.05 ml) within a much larger well (1 ml). The buffer was exchanged in the large well without disturbing the shielded coverslip, and each exchange diluted the buffer 20-fold. Two, the coverslips were coated with molecules that would show preferential adhesion for F-actin, including anti-actin antibodies and G-actin. Other potential coatings include myosin, phalloidin, or avidin/anti-biotin (using biotinylated F-actin). Three, formaldehyde was used a fixative first, which results in short-length fixation of molecules already in close proximity. After free proteins were washed away, more rigorous glutaraldehyde fixation took place.

These approaches showed promise, but were ultimately not yet successful in simultaneously blocking background and retaining F-actin structures.

7.3 AFM filamin strength measurement

Another potential way to determine the cross-linking strength of filamin is to employ atomic force microscopy. Since attaching probes to the actin-binding domains of a single filamin molecule is likely difficult, and hard to interpret, attaching probes to the actin filaments in an individual junction may prove simpler, and easier to interpret.

7.4 Analysis of full networks

With the image processing tools described in Chapter 4 (Computerized Reconstruction of 3-D Networks) it is possible to reconstruct large networks. Using this method, one could analyze the effect of filamin concentration on network architecture. Because the networks need not be labeled before viewing, the sample can be frozen in place after formation and the glass-adhesion challenge is moot. This analysis would clarify how network parameters such as pore size or actin homogeneity change with cross-linker concentration.

Works Cited

1. Boal, D.H., *Mechanics of the cell.* 2002, Cambridge, UK ; New York: Cambridge University Press. xiv, 406 p.
2. Alberts, B., et al., *Molecular Biology of the Cell.* 4th ed. 2002, New York: Garland Science.
3. Davies, P.F., *Spatial hemodynamics, the endothelium, and focal atherogenesis: a cell cycle link?* Circ Res, 2000. **86**(2): p. 114-6.
4. Dewey, C.F., Jr., et al., *The dynamic response of vascular endothelial cells to fluid shear stress.* J Biomech Eng, 1981. **103**(3): p. 177-85.
5. Hubmayr, R.D., et al., *Pharmacological activation changes stiffness of cultured human airway smooth muscle cells.* Am J Physiol, 1996. **271**(5 Pt 1): p. C1660-8.
6. Potard, U.S., J.P. Butler, and N. Wang, *Cytoskeletal mechanics in confluent epithelial cells probed through integrins and E-cadherins.* Am J Physiol, 1997. **272**(5 Pt 1): p. C1654-63.
7. Wang, N. and D.E. Ingber, *Control of cytoskeletal mechanics by extracellular matrix, cell shape, and mechanical tension.* Biophys J, 1994. **66**(6): p. 2181-9.
8. Sato, M., et al., *Application of the micropipette technique to the measurement of cultured porcine aortic endothelial cell viscoelastic properties.* J Biomech Eng, 1990. **112**(3): p. 263-8.
9. Sato, M., N. Ohshima, and R.M. Nerem, *Viscoelastic properties of cultured porcine aortic endothelial cells exposed to shear stress.* J Biomech, 1996. **29**(4): p. 461-7.
10. Bausch, A.R., et al., *Local measurements of viscoelastic parameters of adherent cell surfaces by magnetic bead microrheometry.* Biophys J, 1998. **75**(4): p. 2038-49.
11. Thoumine, O. and A. Ott, *Time scale dependent viscoelastic and contractile regimes in fibroblasts probed by microplate manipulation.* J Cell Sci, 1997. **110**(Pt 17): p. 2109-16.
12. Hofmann, U.G., et al., *Investigating the cytoskeleton of chicken cardiocytes with the atomic force microscope.* J Struct Biol, 1997. **119**(2): p. 84-91.
13. Shroff, S.G., D.R. Saner, and R. Lal, *Dynamic micromechanical properties of cultured rat atrial myocytes measured by atomic force microscopy.* Am J Physiol, 1995. **269**(1 Pt 1): p. C286-92.
14. Satcher, R.L., Jr. and C.F. Dewey, Jr., *Theoretical estimates of mechanical properties of the endothelial cell cytoskeleton.* Biophys J, 1996. **71**(1): p. 109-18.
15. Gibson, L.J. and M.F. Ashby, *Cellular Solids: Structure & Properties.* 1st ed. ed. 1988, Oxford [England] ; New York: Pergamon Press. ix, 357.
16. Ingber, D.E., *The Architecture of Life.* Sci Amer, 1998. **278**: p. 48-57.
17. Coughlin, M.F. and D. Stamenovic, *A tensegrity model of the cytoskeleton in spread and round cells.* J Biomech Eng, 1998. **120**(6): p. 770-7.
18. Stamenovic, D. and M.F. Coughlin, *The role of prestress and architecture of the cytoskeleton and deformability of cytoskeletal filaments in mechanics of adherent cells: a quantitative analysis.* J Theor Biol, 1999. **201**(1): p. 63-74.
19. Stamenovic, D. and M.F. Coughlin, *A quantitative model of cellular elasticity based on tensegrity [In Process Citation].* J Biomech Eng, 2000. **122**(1): p. 39-43.

20. Elson, E.L., *Cellular mechanics as an indicator of cytoskeletal structure and function.* Annu Rev Biophys Biophys Chem, 1988. **17**: p. 397-430.
21. Felder, S. and E.L. Elson, *Mechanics of fibroblast locomotion: quantitative analysis of forces and motions at the leading lamellas of fibroblasts.* J Cell Biol, 1990. **111**(6 Pt 1): p. 2513-26.
22. Luby-Phelps, K., *Physical properties of cytoplasm.* Curr Opin Cell Biol, 1994. **6**(1): p. 3-9.
23. Stossel, T., *On the crawling of animal cells.* Science, 1993. **260**: p. 1086-1094.
24. Ogihara, S. and Y. Tonomura, *A novel 36,000-dalton actin-binding protein purified from microfilaments in Physarum plasmodia which aggregates actin filaments and blocks actin-myosin interaction.* J Cell Biol, 1982. **93**(3): p. 604-14.
25. Ogihara, S., *Calcium and ATP regulation of the oscillatory torsional movement in a triton model of Physarum plasmodial strands.* Exp Cell Res, 1982. **138**(2): p. 377-84.
26. Hartwig, J.H. and P. Shevlin, *The architecture of actin filaments and the ultrastructural location of actin-binding protein in the periphery of lung macrophages.* J Cell Biol, 1986. **103**(3): p. 1007-20.
27. Levine, A.J. and T.C. Lubensky, *One- and two-particle microrheology.* Phys Rev Lett, 2000. **85**(8): p. 1774-7.
28. Levine, A.J. and T.C. Lubensky, *Response function of a sphere in a viscoelastic two-fluid medium.* Phys Rev E Stat Nonlin Soft Matter Phys, 2001. **63**(4 Pt 1): p. 041510.
29. Levine, A.J. and T.C. Lubensky, *Two-point microrheology and the electrostatic analogy.* Phys Rev E Stat Nonlin Soft Matter Phys, 2002. **65**(1 Pt 1): p. 011501.
30. Levine, A.J. and F.C. MacKintosh, *Dynamics of viscoelastic membranes.* Physical Review E, 2002. **66**(6).
31. MacKintosh, F.C. and C.F. Schmidt, *Microrheology.* Current Opinion in Colloid & Interface Science, 1999. **4**(4): p. 300-307.
32. Gardel, M.L. and F. Nakamura, *Unpublished.* 2004.
33. Gardel, M.L., et al., *Microrheology of entangled F-actin solutions.* Phys Rev Lett, 2003. **91**(15): p. 158302.
34. MacKintosh, F.C., J. Kas, and P.A. Janmey, *Elasticity of semiflexible biopolymer networks.* Physical Review Letters, 1995. **75**(24): p. 4425-4428.
35. Maggs, A.C., *Two plateau moduli for actin gels.* Phys Rev E Stat Nonlin Soft Matter Phys, 1997. **55**(6): p. 7396-7400.
36. Maggs, A.C., *Micro-bead mechanics with actin filaments.* Physical Review E, 1998. **57**(2): p. 2091-2094.
37. Maggs, A.C., *Twist and writhe dynamics of stiff polymers.* Phys Rev Lett, 2000. **85**(25): p. 5472-5.
38. Schmidt, F.G., B. Hinner, and E. Sackmann, *Microrheometry underestimates the values of the viscoelastic moduli in measurements on F-actin solutions compared to macrorheometry.* Physical Review E, 2000. **61**(5): p. 5646-5653.
39. Schmidt, F.G., et al., *Viscoelastic properties of semiflexible filamentous bacteriophage fd.* Physical Review E, 2000. **62**(4): p. 5509-5517.

40. Schmidt, F.G., F. Ziemann, and E. Sackmann, *Shear field mapping in actin networks by using magnetic tweezers.* Eur Biophys J, 1996. **24**(5): p. 348-53.
41. Schnurr, B., et al., *Microrheology in actin gels: Experiment and theory.* Biophysical Journal, 1997. **72**(2): p. TU285-TU285.
42. Valentine, M.T., et al., *Investigating the microenvironments of inhomogeneous soft materials with multiple particle tracking.* Phys Rev E Stat Nonlin Soft Matter Phys, 2001. **64**(6 Pt 1): p. 061506.
43. Xu, J.Y., V. Viasnoff, and D. Wirtz, *Compliance of actin filament networks measured by particle- tracking microrheology and diffusing wave spectroscopy.* Rheologica Acta, 1998. **37**(4): p. 387-398.
44. Xu, J.Y., A. Palmer, and D. Wirtz, *Rheology and microrheology of semiflexible polymer solutions: Actin filament networks.* Macromolecules, 1998. **31**(19): p. 6486-6492.
45. Mason, T.G., *Estimating the viscoelastic moduli of complex fluids using the generalized Stokes-Einstein equation.* Rheologica Acta, 2000. **39**(4): p. 371-378.
46. Mason, T.G., et al., *Particle tracking microrheology of complex fluids.* Physical Review Letters, 1997. **79**(17): p. 3282-3285.
47. Mason, T.G., H. Gang, and D.A. Weitz, *Rheology of complex fluids measured by dynamic light scattering.* Journal of Molecular Structure, 1996. **383**(1-3): p. 81-90.
48. Mason, T.G., H. Gang, and D.A. Weitz, *Diffusing-wave-spectroscopy measurements of viscoelasticity of complex fluids.* Journal of the Optical Society of America a-Optics Image Science and Vision, 1997. **14**(1): p. 139-149.
49. Mason, T.G., et al., *Rheology of F-actin solutions determined from thermally driven tracer motion.* Journal of Rheology, 2000. **44**(4): p. 917-928.
50. Mason, T.G. and D.A. Weitz, *Optical Measurements of Frequency-Dependent Linear Viscoelastic Moduli of Complex Fluids.* Physical Review Letters, 1995. **74**(7): p. 1250-1253.
51. Palmer, A., et al., *Diffusing wave spectroscopy microrheology of actin filament networks.* Biophysical Journal, 1999. **76**(2): p. 1063-1071.
52. Palmer, A., J.Y. Xu, and D. Wirtz, *High-frequency viscoelasticity of crosslinked actin filament networks measured by diffusing wave spectroscopy.* Rheologica Acta, 1998. **37**(2): p. 97-106.
53. Morse, D.C., *Viscoelasticity of tightly entangled solutions of semiflexible polymers.* Physical Review E, 1998. **58**(2): p. R1237-R1240.
54. Morse, D.C., *Viscoelasticity of concentrated isotropic solutions of semiflexible polymers. 1. Model and stress tensor.* Macromolecules, 1998. **31**(20): p. 7030-7043.
55. Morse, D.C., *Viscoelasticity of concentrated isotropic solutions of semiflexible polymers. 2. Linear response.* Macromolecules, 1998. **31**(20): p. 7044-7067.
56. Morse, D.C., *Viscoelasticity of concentrated isotropic solutions of semiflexible polymers. 3. Nonlinear rheology.* Macromolecules, 1999. **32**(18): p. 5934-5943.
57. Morse, D.C. and G.H. Fredrickson, *Semiflexible polymers near interfaces.* Physical Review Letters, 1994. **73**(24): p. 3235-3238.

58. Gittes, F. and F.C. MacKintosh, *Dynamic shear modulus of a semiflexible polymer network.* Physical Review E, 1998. **58**(2): p. R1241-R1244.
59. Gittes, F., B. Mickey, and J. Howard, *The Flexural Rigidity of Microtubules Measured from Fluctuations of Curvature.* Faseb Journal, 1992. **6**(1): p. A27-A27.
60. Gittes, F., et al., *Flexural rigidity of microtubules and actin filaments measured from thermal fluctuations in shape.* J Cell Biol, 1993. **120**(4): p. 923-34.
61. Gittes, F., et al., *Microscopic viscoelasticity: Shear moduli of soft materials determined from thermal fluctuations.* Physical Review Letters, 1997. **79**(17): p. 3286-3289.
62. Isambert, H. and A.C. Maggs, *Bending of Actin-Filaments.* Europhysics Letters, 1995. **31**(5-6): p. 263-267.
63. Isambert, H. and A.C. Maggs, *Dynamics and rheology of actin solutions.* Macromolecules, 1996. **29**(3): p. 1036-1040.
64. Isambert, H., et al., *Flexibility of actin filaments derived from thermal fluctuations. Effect of bound nucleotide, phalloidin, and muscle regulatory proteins.* J Biol Chem, 1995. **270**(19): p. 11437-44.
65. MacKintosh, F.C. and P.A. Janmey, *Actin gels.* Current Opinion in Solid State & Materials Science, 1997. **2**(3): p. 350-357.
66. MacKintosh, F.C., *Theoretical models of viscoelasticity of actin solutions and the actin cortex.* Biological Bulletin, 1998. **194**(3): p. 351-353.
67. Schnurr, B., F. Gittes, and F.C. MacKintosh, *Metastable intermediates in the condensation of semiflexible polymers.* Physical Review E, 2002. **65**(6).
68. Schnurr, B., et al., *Determining microscopic viscoelasticity in flexible and semiflexible polymer networks from thermal fluctuations.* Macromolecules, 1997. **30**(25): p. 7781-7792.
69. Head, D.A., A.J. Levine, and F.C. MacKintosh, *Distinct regimes of elastic response and deformation modes of cross-linked cytoskeletal and semiflexible polymer networks.* Physical Review E, 2003. **68**(6): p. 061907.
70. Head, D.A., A.J. Levine, and E.C. MacKintosh, *Deformation of cross-linked semiflexible polymer networks.* Physical Review Letters, 2003. **91**(10).
71. Wang, K., *Filamin, a new high-molecular-weight protein found in smooth muscle and nonmuscle cells. Purification and properties of chicken gizzard filamin.* Biochemistry, 1977. **16**(9): p. 1857-65.
72. Hartwig, J.H. and T.P. Stossel, *Structure of macrophage actin-binding protein molecules in solution and interacting with actin filaments.* J Mol Biol, 1981. **145**(3): p. 563-81.
73. Rosenberg, S. and A. Stracher, *Effect of actin-binding protein on the sedimentation properties of actin.* J Cell Biol, 1982. **94**(1): p. 51-5.
74. Janmey, P.A., et al., *Resemblance of actin-binding protein/actin gels to covalently crosslinked networks.* Nature, 1990. **345**(6270): p. 89-92.
75. Ruddies, R., et al., *The viscoelastic moduli of actin/filamin solutions: a micro-rheologic study.* Biochem Soc Trans, 1993. **21**(1): p. 37S.

76. Zaner, K.S., *The effect of the 540-kilodalton actin cross-linking protein, actin- binding protein, on the mechanical properties of F-actin.* J Biol Chem, 1986. **261**(17): p. 7615-20.
77. Brotschi, E.A., J.H. Hartwig, and T.P. Stossel, *The gelation of actin by actin-binding protein.* J Biol Chem, 1978. **253**(24): p. 8988-93.
78. Cunningham, C.C., *Actin polymerization and intracellular solvent flow in cell surface blebbing.* J Cell Biol, 1995. **129**(6): p. 1589-99.
79. Cunningham, C.C., et al., *Actin-binding protein requirement for cortical stability and efficient locomotion.* Science, 1992. **255**(5042): p. 325-7.
80. Shin, J.H., et al., *Relating microstructure to rheology of a bundled and cross-linked F-actin network in vitro.* Proc Natl Acad Sci U S A, 2004. **101**(26): p. 9636-41.
81. Gardel, M.L., et al., *Elastic behavior of cross-linked and bundled actin networks.* Science, 2004. **304**(5675): p. 1301-5.
82. Flory, P.J., *Principles of polymer chemistry.* George Fisher Baker non-resident lectureship in chemistry at Cornell University. 1953, Ithaca,: Cornell University Press. 672 p.
83. Ferry, J.D., *Viscoelastic Properties of Polymers.* 2nd ed. 1970, New York: John Wiley & Sons.
84. Nossal, R., *On the elasticity of cytoskeletal networks.* Biophys J, 1988. **53**(3): p. 349-59.
85. Janssen, K.P., et al., *Viscoelastic properties of F-actin solutions in the presence of normal and mutated actin-binding proteins.* Arch Biochem Biophys, 1996. **325**(2): p. 183-9.
86. Muller, O., et al., *Viscoelastic Moduli of Sterically and Chemically Cross-Linked Actin Networks in the Dilute to Semidilute Regime - Measurements By an Oscillating Disk Rheometer.* Macromolecules, 1991. **24**(11): p. 3111-3120.
87. Wachsstock, D.H., W.H. Schwartz, and T.D. Pollard, *Affinity of alpha-actinin for actin determines the structure and mechanical properties of actin filament gels.* Biophys J, 1993. **65**(1): p. 205-14.
88. Wachsstock, D.H., W.H. Schwarz, and T.D. Pollard, *Cross-linker dynamics determine the mechanical properties of actin gels.* Biophys J, 1994. **66**(3 Pt 1): p. 801-9.
89. Podolski, J.L. and T.L. Steck, *Length distribution of F-actin in Dictyostelium discoideum.* J Biol Chem, 1990. **265**(3): p. 1312-8.
90. McGrath, J.L., et al., *Measuring actin dynamics in endothelial cells.* Microsc Res Tech, 1998. **43**(5): p. 385-94.
91. Burlacu, S., P.A. Janmey, and J. Borejdo, *Distribution of actin filament lengths measured by fluorescence microscopy.* Am J Physiol, 1992. **262**(3 Pt 1): p. C569-77.
92. Howard, J., *Mechanics of motor proteins and the cytoskeleton.* 2001, Sunderland, Mass.: Sinauer Associates, Publishers. xvi, 367 p.
93. Fox, J.W., et al., *Mutations in filamin 1 prevent migration of cerebral cortical neurons in human periventricular heterotopia.* Neuron, 1998. **21**(6): p. 1315-25.
94. Sharma, C.P., R.M. Ezzell, and M.A. Arnaout, *Direct interaction of filamin (ABP-280) with the beta 2-integrin subunit CD18.* J Immunol, 1995. **154**(7): p. 3461-70.

95. Calderwood, D.A., et al., *Increased filamin binding to beta-integrin cytoplasmic domains inhibits cell migration.* Nat Cell Biol, 2001. **3**(12): p. 1060-8.
96. Ohta, Y., et al., *The small GTPase RalA targets filamin to induce filopodia.* Proc Natl Acad Sci U S A, 1999. **96**(5): p. 2122-8.
97. Andrews, R.K. and J.E. Fox, *Interaction of purified actin-binding protein with the platelet membrane glycoprotein Ib-IX complex.* J Biol Chem, 1991. **266**(11): p. 7144-7.
98. Stossel, T.P., et al., *Filamins as integrators of cell mechanics and signalling.* Nat Rev Mol Cell Biol, 2001. **2**(2): p. 138-45.
99. Feng, Y. and C.A. Walsh, *The many faces of filamin: A versatile molecular scaffold for cellular motility and signalling.* Manuscript Submitted, 2004.
100. Meyer, S.C., et al., *Identification of the region in actin-binding protein that binds to the cytoplasmic domain of glycoprotein IBalpha.* J Biol Chem, 1997. **272**(5): p. 2914-9.
101. Ott, I., et al., *A role for tissue factor in cell adhesion and migration mediated by interaction with actin-binding protein 280.* J Cell Biol, 1998. **140**(5): p. 1241-53.
102. Ohta, Y., T.P. Stossel, and J.H. Hartwig, *Ligand-sensitive binding of actin-binding protein to immunoglobulin G Fc receptor I (Fc gamma RI).* Cell, 1991. **67**(2): p. 275-82.
103. Liu, G., et al., *Cytoskeletal protein ABP-280 directs the intracellular trafficking of furin and modulates proprotein processing in the endocytic pathway.* J Cell Biol, 1997. **139**(7): p. 1719-33.
104. Thompson, T.G., et al., *Filamin 2 (FLN2): A muscle-specific sarcoglycan interacting protein.* J Cell Biol, 2000. **148**(1): p. 115-26.
105. van der Ven, P.F., et al., *Indications for a novel muscular dystrophy pathway. gamma-filamin, the muscle-specific filamin isoform, interacts with myotilin.* J Cell Biol, 2000. **151**(2): p. 235-48.
106. Stahlhut, M. and B. van Deurs, *Identification of filamin as a novel ligand for caveolin-1: evidence for the organization of caveolin-1-associated membrane domains by the actin cytoskeleton.* Mol Biol Cell, 2000. **11**(1): p. 325-37.
107. Guo, Y., et al., *Physical and genetic interaction of filamin with presenilin in Drosophila.* J Cell Sci, 2000. **113 Pt 19**: p. 3499-508.
108. Binda, A.V., et al., *D2 and D3 dopamine receptor cell surface localization mediated by interaction with protein 4.1N.* Mol Pharmacol, 2002. **62**(3): p. 507-13.
109. Browne, K.A., et al., *Filamin (280-kDa actin-binding protein) is a caspase substrate and is also cleaved directly by the cytotoxic T lymphocyte protease granzyme B during apoptosis.* J Biol Chem, 2000. **275**(50): p. 39262-6.
110. Edwards, D.N., P. Towb, and S.A. Wasserman, *An activity-dependent network of interactions links the Rel protein Dorsal with its cytoplasmic regulators.* Development, 1997. **124**(19): p. 3855-64.
111. Leonardi, A., et al., *Physical and functional interaction of filamin (actin-binding protein-280) and tumor necrosis factor receptor-associated factor 2.* J Biol Chem, 2000. **275**(1): p. 271-8.

112. Marti, A., et al., *Actin-binding protein-280 binds the stress-activated protein kinase (SAPK) activator SEK-1 and is required for tumor necrosis factor-alpha activation of SAPK in melanoma cells.* J Biol Chem, 1997. **272**(5): p. 2620-8.
113. Ozanne, D.M., et al., *Androgen receptor nuclear translocation is facilitated by the f-actin cross-linking protein filamin.* Mol Endocrinol, 2000. **14**(10): p. 1618-26.
114. Bellanger, J.M., et al., *The Rac1- and RhoG-specific GEF domain of Trio targets filamin to remodel cytoskeletal actin.* Nat Cell Biol, 2000. **2**(12): p. 888-92.
115. Krief, S., et al., *Identification and characterization of cvHsp. A novel human small stress protein selectively expressed in cardiovascular and insulin-sensitive tissues.* J Biol Chem, 1999. **274**(51): p. 36592-600.
116. Petrecca, K., D.M. Miller, and A. Shrier, *Localization and enhanced current density of the Kv4.2 potassium channel by interaction with the actin-binding protein filamin.* J Neurosci, 2000. **20**(23): p. 8736-44.
117. Sampson, L.J., M.L. Leyland, and C. Dart, *Direct interaction between the actin-binding protein filamin-A and the inwardly rectifying potassium channel, Kir2.1.* J Biol Chem, 2003. **278**(43): p. 41988-97.
118. Yuan, Y. and Z. Shen, *Interaction with BRCA2 suggests a role for filamin-1 (hsFLNa) in DNA damage response.* J Biol Chem, 2001. **276**(51): p. 48318-24.
119. Sasaki, A., et al., *Filamin associates with Smads and regulates transforming growth factor-beta signaling.* J Biol Chem, 2001. **276**(21): p. 17871-7.
120. Awata, H., et al., *Interaction of the calcium-sensing receptor and filamin, a potential scaffolding protein.* J Biol Chem, 2001. **276**(37): p. 34871-9.
121. Tigges, U., et al., *The F-actin cross-linking and focal adhesion protein filamin A is a ligand and in vivo substrate for protein kinase C alpha.* J Biol Chem, 2003. **278**(26): p. 23561-9.
122. Nagano, T., et al., *Filamin A-interacting protein (FILIP) regulates cortical cell migration out of the ventricular zone.* Nat Cell Biol, 2002. **4**(7): p. 495-501.
123. Tu, Y., et al., *Migfilin and Mig-2 link focal adhesions to filamin and the actin cytoskeleton and function in cell shape modulation.* Cell, 2003. **113**(1): p. 37-47.
124. Woo, M.S., et al., *Ribosomal S6 kinase (RSK) regulates phosphorylation of filamin A on an important regulatory site.* Mol Cell Biol, 2004. **24**(7): p. 3025-35.
125. Dyson, J.M., et al., *SHIP-2 forms a tetrameric complex with filamin, actin, and GPIb-IX-V: localization of SHIP-2 to the activated platelet actin cytoskeleton.* Blood, 2003. **102**(3): p. 940-8.
126. Vadlamudi, R.K., et al., *Filamin is essential in actin cytoskeletal assembly mediated by p21-activated kinase 1.* Nat Cell Biol, 2002. **4**(9): p. 681-90.
127. Lu, S., et al., *New N-RAP-binding partners alpha-actinin, filamin and Krp1 detected by yeast two-hybrid screening: implications for myofibril assembly.* J Cell Sci, 2003. **116**(Pt 11): p. 2169-78.
128. He, H.J., et al., *Interaction of filamin A with the insulin receptor alters insulin-dependent activation of the mitogen-activated protein kinase pathway.* J Biol Chem, 2003. **278**(29): p. 27096-104.

129. Grimbert, P., et al., *The Filamin-A is a partner of Tc-mip, a new adapter protein involved in c-maf-dependent Th2 signaling pathway.* Mol Immunol, 2004. **40**(17): p. 1257-61.
130. Nikki, M., J. Merilainen, and V.P. Lehto, *FAP52 regulates actin organization via binding to filamin.* J Biol Chem, 2002. **277**(13): p. 11432-40.
131. Pawel, *Unpublished.* 2004.
132. Hartwig, J.H. and T.P. Stossel, *Isolation and properties of actin, myosin, and a new actinbinding protein in rabbit alveolar macrophages.* J Biol Chem, 1975. **250**(14): p. 5696-705.
133. Condeelis, J., J. Salisbury, and K. Fujiwara, *A new protein that gels F actin in the cell cortex of Dictyostelium discoideum.* 1981. **292**(5819): p. 161-162.
134. Noegel, A.A., et al., *The Dictyostelium gelation factor shares a putative actin binding site with alpha-actinins and dystrophin and also has a rod domain containing six 100-residue motifs that appear to have a cross-beta conformation.* 1989. **109**(2): p. 607-618.
135. Vargas, M., P. Sansonetti, and N. Guillen, *Identification and cellular localization of the actin-binding protein ABP-120 from Entamoeba histolytica.* 1996. **22**(5): p. 849-857.
136. Gorlin, J.B., et al., *Human endothelial actin-binding protein (ABP-280, nonmuscle filamin): a molecular leaf spring.* J Cell Biol, 1990. **111**(3): p. 1089-105.
137. van der Flier, A. and A. Sonnenberg, *Structural and functional aspects of filamins.* Biochim Biophys Acta, 2001. **1538**(2-3): p. 99-117.
138. Gariboldi, M., et al., *Comparative mapping of the actin-binding protein 280 genes in human and mouse.* Genomics, 1994. **21**(2): p. 428-30.
139. Moro, F., et al., *Familial periventricular heterotopia: missense and distal truncating mutations of the FLN1 gene.* Neurology, 2002. **58**(6): p. 916-21.
140. Kakita, A., et al., *Bilateral periventricular nodular heterotopia due to filamin 1 gene mutation: widespread glomeruloid microvascular anomaly and dysplastic cytoarchitecture in the cerebral cortex.* Acta Neuropathol (Berl), 2002. **104**(6): p. 649-57.
141. Sheen, V.L., et al., *Mutations in the X-linked filamin 1 gene cause periventricular nodular heterotopia in males as well as in females.* Hum Mol Genet, 2001. **10**(17): p. 1775-83.
142. Robertson, S.P., et al., *Localized mutations in the gene encoding the cytoskeletal protein filamin A cause diverse malformations in humans.* Nat Genet, 2003. **33**(4): p. 487-91.
143. Chakarova, C., et al., *Genomic structure and fine mapping of the two human filamin gene paralogues FLNB and FLNC and comparative analysis of the filamin gene family.* Hum Genet, 2000. **107**(6): p. 597-611.
144. Krakow, D., et al., *Mutations in the gene encoding filamin B disrupt vertebral segmentation, joint formation and skeletogenesis.* Nat Genet, 2004. **36**(4): p. 405-10.
145. Xie, Z., et al., *Molecular cloning of human ABPL, an actin-binding protein homologue.* Biochem Biophys Res Commun, 1998. **251**(3): p. 914-9.
146. Hartwig, J. and J. Italiano, Jr., *The birth of the platelet.* J Thromb Haemost, 2003. **1**(7): p. 1580-6.
147. Davies, P.J., et al., *Filamin-actin interaction. Dissociation of binding from gelation by Ca2+-activated proteolysis.* J Biol Chem, 1978. **253**(11): p. 4036-42.

148. Van Troys, M., J. Vandekerckhove, and C. Ampe, *Structural modules in actin-binding proteins: towards a new classification.* Biochim Biophys Acta, 1999. **1448**(3): p. 323-48.
149. Matsudaira, P., *Modular organization of actin crosslinking proteins.* Trends Biochem Sci, 1991. **16**(3): p. 87-92.
150. Banuelos, S., M. Saraste, and K.D. Carugo, *Structural comparisons of calponin homology domains: implications for actin binding.* Structure, 1998. **6**(11): p. 1419-31.
151. Bresnick, A.R., P.A. Janmey, and J. Condeelis, *Evidence that a 27-residue sequence is the actin-binding site of ABP-120.* J Biol Chem, 1991. **266**(20): p. 12989-93.
152. Kuhlman, P.A., L. Hemmings, and D.R. Critchley, *The identification and characterisation of an actin-binding site in alpha-actinin by mutagenesis.* FEBS Lett, 1992. **304**(2-3): p. 201-6.
153. Lebart, M.C., et al., *Characterization of the actin binding site on smooth muscle filamin.* J Biol Chem, 1994. **269**(6): p. 4279-84.
154. Mejean, C., et al., *Inhibition of actin-dystrophin interaction by inositide phosphate.* Biochem Biophys Res Commun, 1995. **210**(1): p. 152-8.
155. Nakamura, F., *Unpublished.*
156. Maruta, H. and E.D. Korn, *Acanthamoeba myosin II.* J Biol Chem, 1977. **252**(18): p. 6501-9.
157. Davies, P., P. Bechtel, and I. Pastan, *Filamin inhibits actin activation of heavy meromyosin ATPase.* FEBS Lett, 1977. **77**(2): p. 228-32.
158. Zeece, M.G., R.M. Robson, and P.J. Bechtel, *Interaction of alpha-actinin, filamin and tropomyosin with F-actin.* Biochim Biophys Acta, 1979. **581**(2): p. 365-70.
159. Koteliansky, V.E., et al., *The regulation by vinculin of filamin, alpha-actinin, and spectrin tetramer-induced actin sol-gel transformation.* FEBS Lett, 1983. **151**(2): p. 206-10.
160. Sobue, K., et al., *Reconstitution of Ca2+-sensitive gelation of actin filaments with filamin, caldesmon and calmodulin.* FEBS Lett, 1982. **138**(2): p. 289-92.
161. Rosenberg, S., A. Stracher, and K. Burridge, *Isolation and characterization of a calcium-sensitive alpha-actinin-like protein from human platelet cytoskeletons.* J Biol Chem, 1981. **256**(24): p. 12986-91.
162. Hanein, D., et al., *An atomic model of fimbrin binding to F-actin and its implications for filament crosslinking and regulation.* Nat Struct Biol, 1998. **5**(9): p. 787-92.
163. Moores, C.A., N.H. Keep, and J. Kendrick-Jones, *Structure of the utrophin actin-binding domain bound to F-actin reveals binding by an induced fit mechanism.* J Mol Biol, 2000. **297**(2): p. 465-80.
164. Miyata, H., R. Yasuda, and K. Kinosita, Jr., *Strength and lifetime of the bond between actin and skeletal muscle alpha-actinin studied with an optical trapping technique.* Biochim Biophys Acta, 1996. **1290**(1): p. 83-8.
165. Finer, J.T., A.D. Mehta, and J.A. Spudich, *Characterization of single actin-myosin interactions.* Biophys J, 1995. **68**(4 Suppl): p. 291S-296S; discussion 296S-297S.
166. Meyer, R.K. and U. Aebi, *Bundling of actin filaments by alpha-actinin depends on its molecular length.* J Cell Biol, 1990. **110**(6): p. 2013-24.

167. Furuike, S., T. Ito, and M. Yamazaki, *Mechanical unfolding of single filamin A (ABP-280) molecules detected by atomic force microscopy.* FEBS Lett, 2001. **498**(1): p. 72-5.
168. Li, H., et al., *Point mutations alter the mechanical stability of immunoglobulin modules.* Nat Struct Biol, 2000. **7**(12): p. 1117-20.
169. Schwaiger, I., et al., *A mechanical unfolding intermediate in an actin-crosslinking protein.* Nat Struct Mol Biol, 2004. **11**(1): p. 81-5.
170. Kellermayer, M.S., et al., *Folding-unfolding transitions in single titin molecules characterized with laser tweezers.* Science, 1997. **276**(5315): p. 1112-6.
171. Tskhovrebova, L., et al., *Elasticity and unfolding of single molecules of the giant muscle protein titin.* Nature, 1997. **387**(6630): p. 308-12.
172. Rief, M., et al., *Reversible unfolding of individual titin immunoglobulin domains by AFM.* Science, 1997. **276**(5315): p. 1109-12.
173. Rief, M., et al., *Single molecule force spectroscopy of spectrin repeats: low unfolding forces in helix bundles.* J Mol Biol, 1999. **286**(2): p. 553-61.
174. Law, R., et al., *Cooperativity in Forced Unfolding of Tandem Spectrin Repeats.* Biophys. J., 2003. **84**(1): p. 533-544.
175. Davies, P.J., et al., *Self-association of chicken gizzard filamin and heavy merofilamin.* Biochemistry, 1980. **19**(7): p. 1366-72.
176. Shizuta, Y., et al., *Purification and properties of filamin, and actin binding protein from chicken gizzard.* J Biol Chem, 1976. **251**(21): p. 6562-7.
177. Blanchoin, L., et al., *Direct observation of dendritic actin filament networks nucleated by Arp2/3 complex and WASP/Scar proteins.* Nature, 2000. **404**(6781): p. 1007-11.
178. Luby-Phelps, K., F. Lanni, and D.L. Taylor, *The Submicroscopic Properties of Cytoplasm as a Determinant of Cellular Function.* Annu Rev Biophys Biophys Chem, 1988. **17**(1): p. 369-396.
179. Hartwig, J.H., J. Tyler, and T.P. Stossel, *Actin-binding protein promotes the bipolar and perpendicular branching of actin filaments.* J Cell Biol, 1980. **87**(3 Pt 1): p. 841-8.
180. Spudich, J.A. and S. Watt, *The regulation of rabbit skeletal muscle contraction. I. Biochemical studies of the interaction of the tropomyosin-troponin complex with actin and the proteolytic fragments of myosin.* J Biol Chem, 1971. **246**(15): p. 4866-71.
181. Lane, D. and E. Harlow, *Two different viral transforming proteins bind the same host tumour antigen.* 1982. **298**(5874): p. 517.
182. Tyler, J.M. and D. Branton, *Rotary shadowing of extended molecules dried from glycerol.* J Ultrastruct Res, 1980. **71**(2): p. 95-102.
183. Mabuchi, K., *Electron microscopic study of tropomyosin binding to actin filaments reveals tethered molecules representing weak binding.* J Struct Biol, 1996. **116**(2): p. 278-89.
184. Niederman, R., P.C. Amrein, and J. Hartwig, *Three-dimensional structure of actin filaments and of an actin gel made with actin-binding protein.* J Cell Biol, 1983. **96**(5): p. 1400-13.
185. Cheng, Y., et al., *Three-dimensional reconstruction of the actin cytoskeleton from stereo images.* J Biomech, 2000. **33**(1): p. 105-13.

186. Lawrence, M.C., *Least-squares method of alignment using markers*, in *Electron Tomography*, J. Frank, Editor. 1992, Plenum Press: New York.
187. Luther, P.K. and M.C. Lawrence, *A method for monitoring the collapse of plastic sections as a function of electron dose.* Ultramicroscopy, 1988. **24**(1): p. 7-18.
188. Hartemink, C.A., *Modeling the interaction between actin and filamin 1 in the cell cytoskeleton*, in *Mechanical engineering*. 1999, Massachusetts Institute of Technology: Cambridge. p. 51.
189. Kas, J., et al., *F-actin, a model polymer for semiflexible chains in dilute, semidilute, and liquid crystalline solutions.* Biophys J, 1996. **70**(2): p. 609-25.
190. Manneville, J.-B., et al., *Interaction of the actin cytoskeleton with microtubules regulates secretory organelle movement near the plasma membrane in human endothelial cells.* J Cell Sci, 2003. **116**(19): p. 3927-3938.
191. Frangos, J.A., et al., *Flow effects on prostacyclin production by cultured human endothelial cells.* Science, 1985. **227**(4693): p. 1477-9.
192. Hishikawa, K., et al., *Pressure enhances endothelin-1 release from cultured human endothelial cells.* Hypertension, 1995. **25**(3): p. 449-52.
193. Langevin, P., *Sur la theorie du mouvement Brownien (On the theory of Brownian motion).* C. R. Acad Sci Paris, 1908. **146**: p. 530-533.
194. Finer, J.T., R.M. Simmons, and J.A. Spudich, *Single myosin molecule mechanics: piconewton forces and nanometre steps.* Nature, 1994. **368**(6467): p. 113-9.
195. Huxley, H.E., *The mechanism of muscular contraction.* Science, 1969. **164**(886): p. 1356-65.
196. Inoue, S. and L.G. Tilney, *Acrosomal reaction of thyone sperm. I. Changes in the sperm head visualized by high resolution video microscopy.* J Cell Biol, 1982. **93**(3): p. 812-9.
197. Dogterom, M. and B. Yurke, *Measurement of the force-velocity relation for growing microtubules.* Science, 1997. **278**(5339): p. 856-60.
198. Tsuda, Y., et al., *Torsional rigidity of single actin filaments and actin-actin bond breaking force under torsion measured directly by in vitro micromanipulation.* Proc Natl Acad Sci U S A, 1996. **93**(23): p. 12937-42.
199. Jing, Q., T. Mukherjee, and G. Fedder. *Large-Deflection Beam Model for Schematic-Based Behavioral Simulation in NODAS.* in *Technical Proceedings of the Fifth International Conference on Modeling and Simulation of Microsystems*. 2002. San Juan, PR.

Appendix: Electron Microscopy Protocols

Making replica transfer pipets

1. Carefully break the tips or microinjection needles where the diameter is about 1/8".
2. Hold the broken tip in the edge of a flame until it liquefies and seals itself.
3. Put the pipette about half an inch into the flame, and the glass tip will bend into an "L" as it heats.

The bent tip needs to be from a section of glass thick enough that the replica cannot wrap all the way around it and touch itself. The bent tip needs to be small enough to fit in the water wells, but long enough to hold a replica.

Making grids

For replicas on glass:

1. Dissolve 0.5g Polyvinyl Formal (Formvar) into 100 ml chloroform. Because chloroform dissolves plastic, all work must be done in glass containers.
2. Fill slide container with 50 ml 0.5% formvar solution.
3. Clean a new slide with a paper towel, using no liquid cleaner or Kim-wipes to prevent surface irregularities and dust.
4. Immerse slide in solution, and remove slowly and evenly. Allow the thin film to air dry while the slide rests vertically on one of its short ends.
5. Cut a large rectangle into the film on one side of the slide through the nearly transparent film. Do not include the runoff at the bottom of the slide. Scrape the edges of the slide with the edge of a razor blade to facilitate detachment.
6. Breathe rapidly on the film three times and quickly immerse slide into water. If the film is floating on the water's surface, proceed. If the film has ripped or bunched or not detached from the glass, repeat with more humid breathing and more suddenly immersion.
7. Place as many grids as possible on the floating rectangle. Orient your grids with the same side up for easier identification of flipped grids. Marking the four corners with grids is a helpful visual technique.
8. When the formvar is filled with grids, place a piece of parafilm on the formvar, sandwiching the grids between the formvar and the parafilm. Gently push the parafilm below the water, invert the system, and bring the parafilm out of the water with the formvar on top. Allow to air dry.
9. Carbon coat the grids in the bell chamber: Close V1 and V3 so the DP is pumping down the RP. Open the bell, insert the carbon rods. The point of the one should just be touching the face of the other. Insert the samples and reseal the bell. Open V3 when the ready light turns on, and turn on current through the Carbon. Only an instant of sputtering is necessary.
10. Remove grids and store covered.

For replicas on mica:
No pretreatment is necessary. The grids are used as manufactured.

Making tabs

1. Cut filter paper into 5 mm × 5 mm squares and apply to rough side of metal tabs with a small droplet of epoxy. Do not saturate paper with epoxy. Warming the glued tabs will enhance bonding. Prepare 200 or more for stock.
2. Dilute 1 g agarose into 100 ml water for a stock 1% solution. Store at 4 °C in gelled form.
3. Place one drop of vacuum grease on the periphery of the tab, and mount a clear plastic O-ring. This standardizes the height of the agar applied.

4. Microwave the agar until it liquefies. Place a large drop on each of 10 tabs. Place a slide over tabs to standardize height, and place the ice-water beaker on slide to cool the gar into a gel.

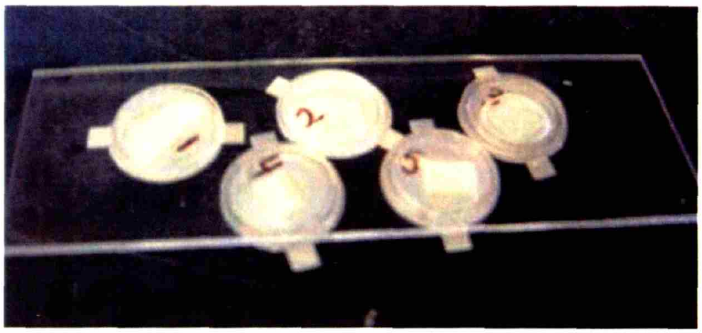

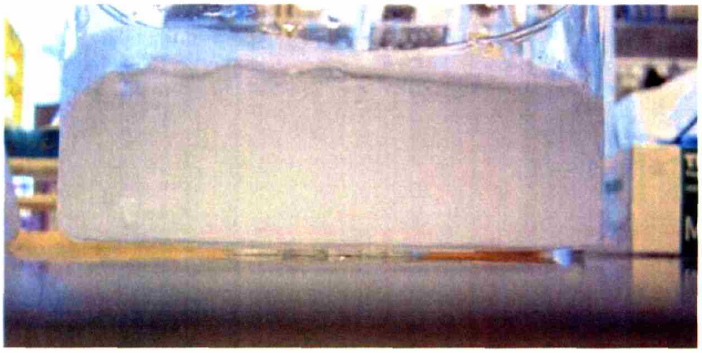

5. After the agar has set, remove the O-rings and trim each agar mount into centered square smaller than a 5 mm circular glass coverslip. If the agar protrudes beyond the coverslip, the sample on the coverslip can be contaminated by the agar during wicking.
6. Replace the O-ring on each tab and use. If the tabs are not removed from the slide, there is enough of a seal to preserve the gelled agar for a couple days in a hydrated chamber at 4°C.

Freezing the sample

1. On the back of each tab write the number of the sample (generally 3-5 digits for record keeping).
2. On the slamming "mount" place the metal tab and bend the side tabs back around the mount with tweezers to ensure no movement. Remove the tab, and bend the side tabs more acutely to prevent sample loss during rotation.

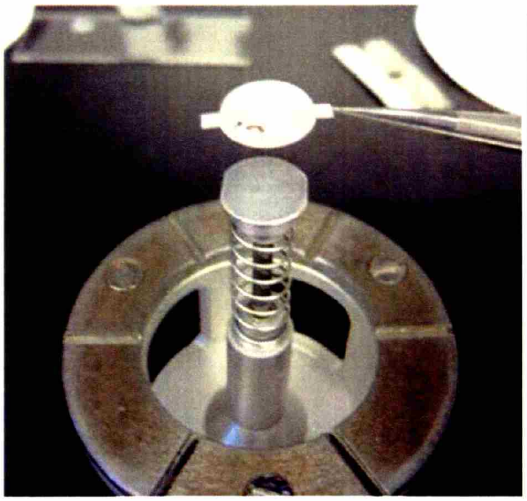

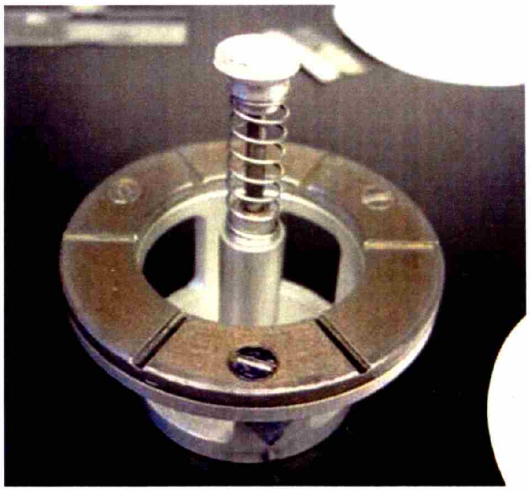

3. Wick the agar dry to create a uniform mount and prevent contamination of liquid sample by agar liquid. Use tweezers to carefully remove a coverslip from its Petri dish and place it on the agar. If the sample contains fixed cells, quickly add a drop of distilled water to prevent the cells from drying out. If the sample contains an actin gel, do not add water as that may damage the network.

4. When the slamming apparatus is ready and cooled to about –220°C, wick the edge of the coverslip to remove the water from the sample. Excess water can shear the sample. Only the top 10 microns of the sample are frozen uniformly and without damage. Cells are bound to the coverslip, and thus below this region, so we wick away the drop. An actin gel permeates the entire drop, and thus does not need to be wicked.
5. Once the water is removed, immediately mount the sample on the magnet and slam.

Preparation for Slamming

1. Boil 500 ml of water to thaw the block during freezing.
2. Prepare two 100 ml beakers of methanol to clean the block.

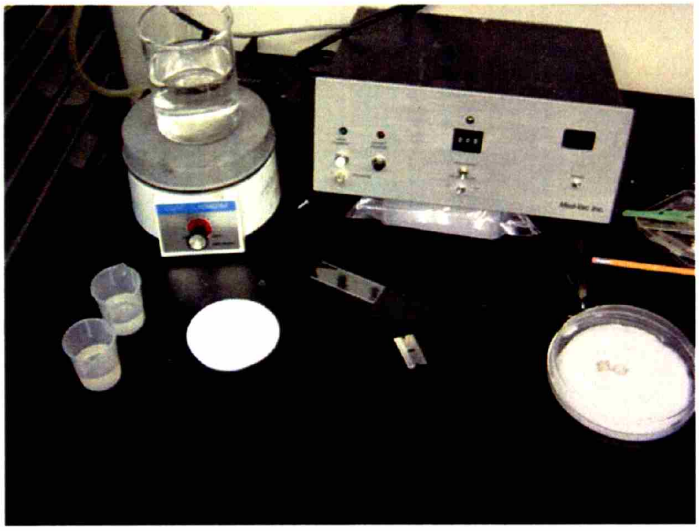

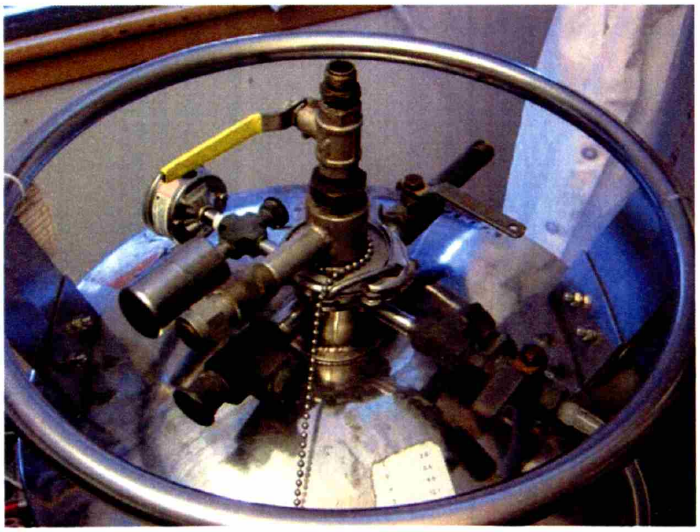

3. Open the He and N_2 gas canisters.
4. Vent the liquid helium tank slowly.
5. When the tank has equilibrated, close the vent. Open the tubed valve that vents into a beaker of water and open the top valve. Unscrew the brass fittings and slide the plunger into the top valve slowly until it reaches the bottom.

6. Secure the plunger outlet with the two screws into the platform.

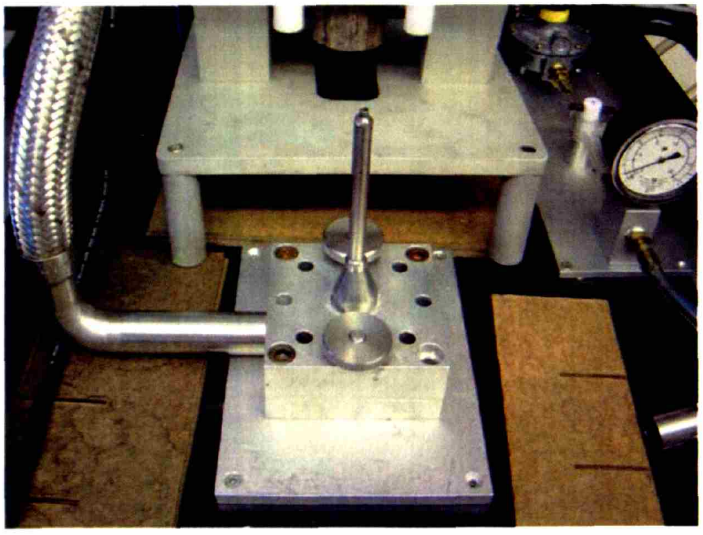

7. Place the magnet apparatus over the plunger.

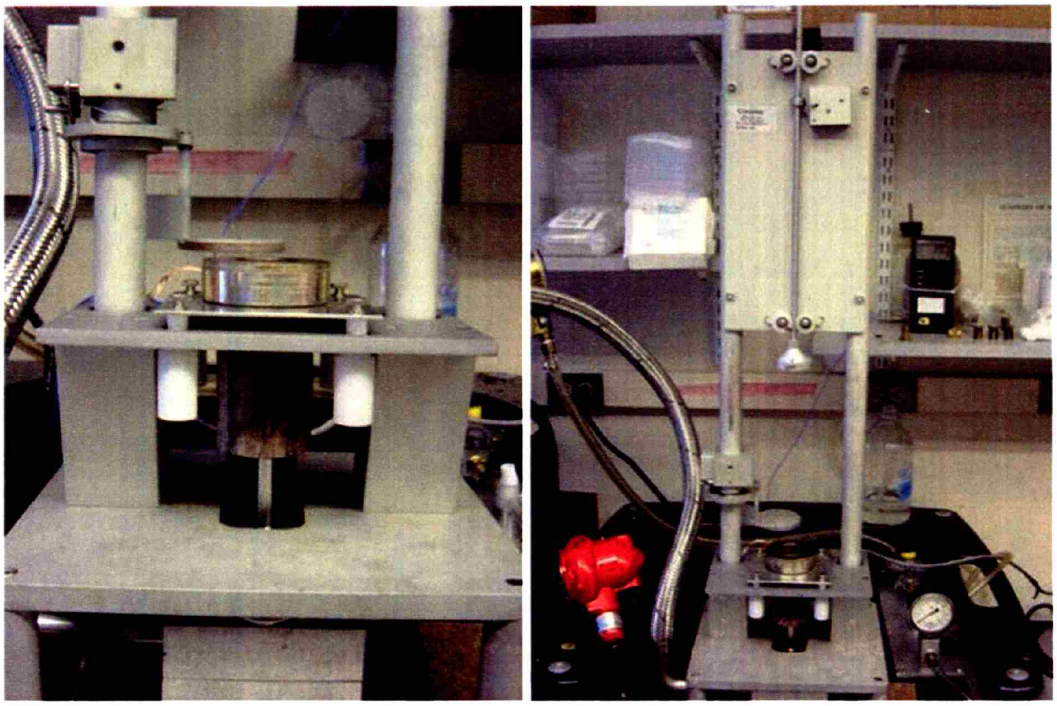

8. Insert a plug into the plunger outlet to prevent helium leakage (generally a cotton swab attached to a pipette tip).

Slamming the sample:

1. Place the cleaned gold stage onto the plunger outlet below the dropper.

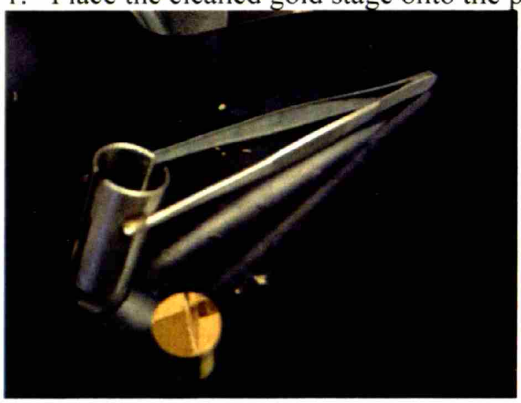
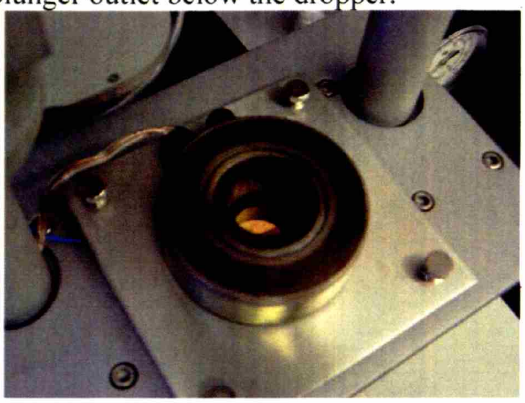

2. Turn the gas T-valve open and close the door over the plunger outlet. The T-valve now connects the back-pressure gaseous helium tank and the liquid helium tank. With the tremendous pressure, the liquid helium is forced up through the plunger and against the gold table. The stage is approaching 50 K (-220 C).

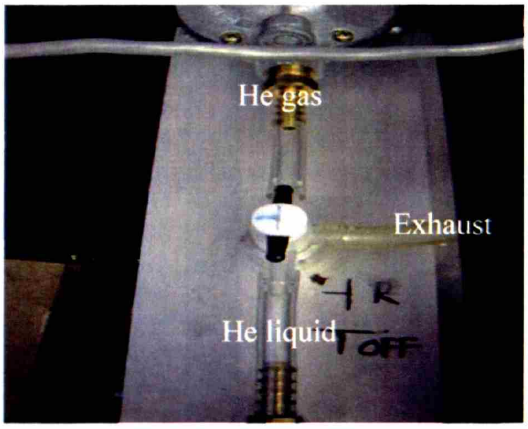

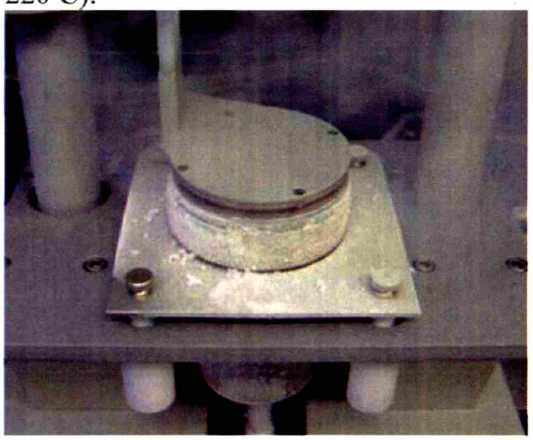

3. When the gold stage reaches -220 C, attach the sample/mount upside down above the gold stage (aligning the arrows), close the T-valve release and press "Drop Plunger."

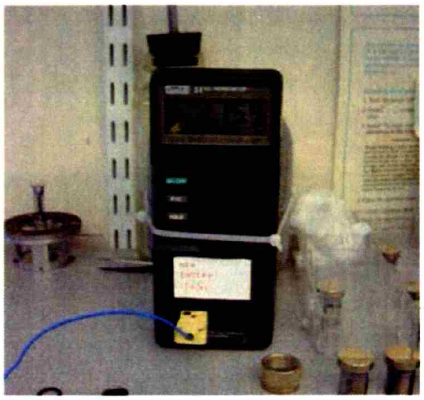

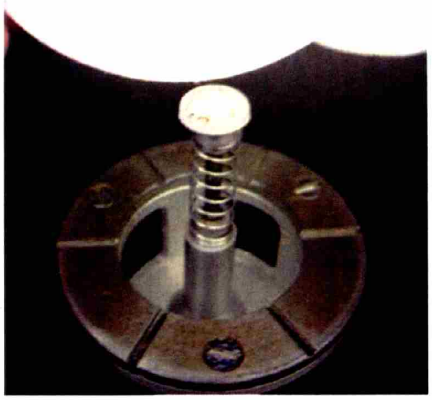

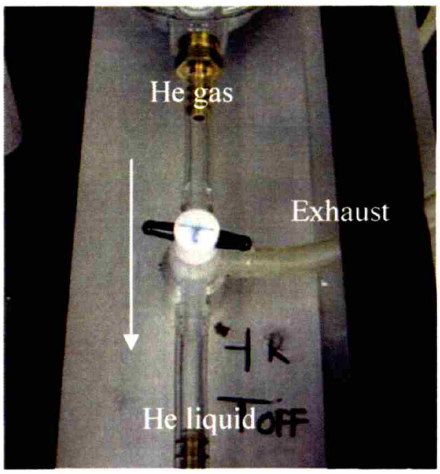

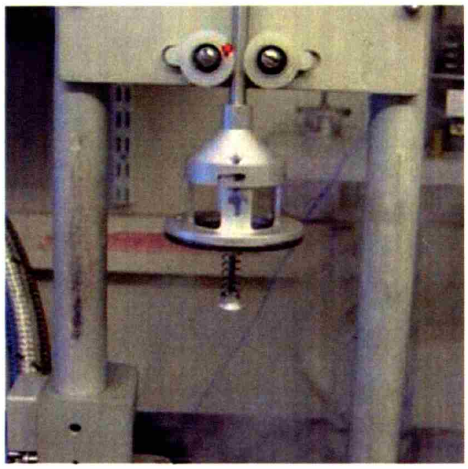

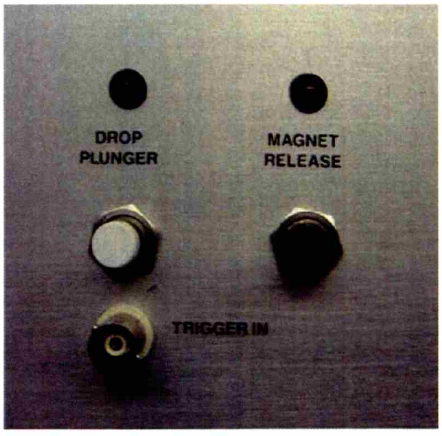

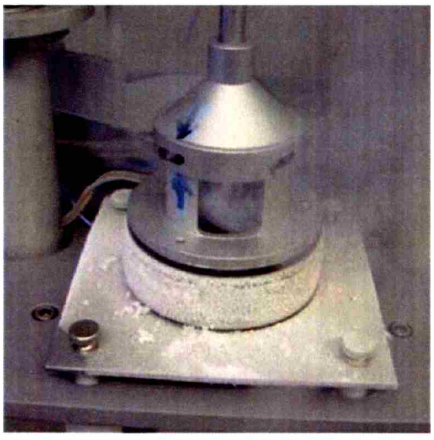

4. Untwist the dropper from the sample, slide the dropper back up to its ready position, and then press "Magnet Release" to free the sample from the gold stage.

5. *Immediately* move the sample to a waiting container of liquid nitrogen, and use forceps to pry the sample from the mount. It is frozen and ready for metal coating.

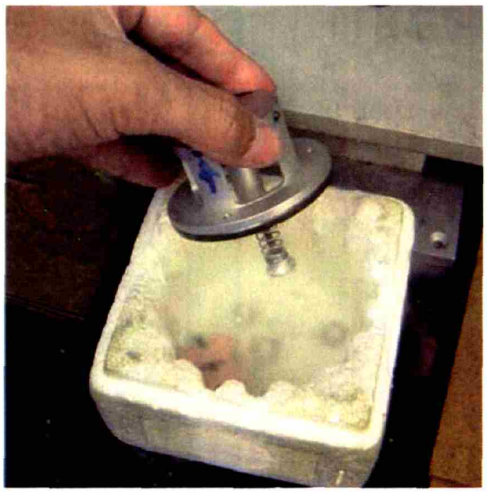

6. Remove the gold stage from the plunger outlet using the stage forceps, then immerse it in boiling water to bring it to room temperature, and then immerse it in methanol twice to clean it from any water residue. Close the gaseous helium tank by turning the T-valve such that the liquid helium vents into the beaker of water.
7. Use the heat gun to warm the slamming apparatus thoroughly, and dry it with a Kim-Wipe.
8. When the next sample is ready, replace the gold stage over the plunger outlet, swing the door closed, and repeat.

Mounting the Sample on the Stage and into Chamber:

1. Pour liquid nitrogen into the two coolers on right side of chamber. Wait for the stage thermometer to reach –170° (about 20-30 minutes).

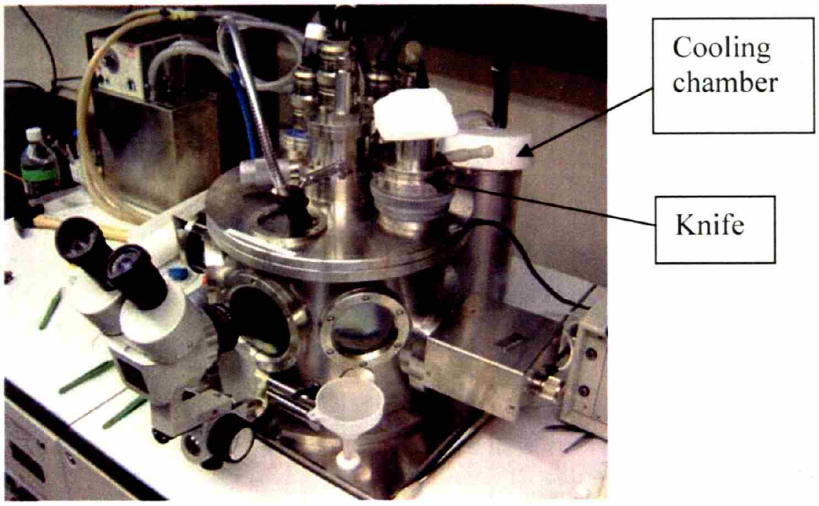

2. Place a copper 4-arm stage in liquid nitrogen. The tabs (with samples) should already be in liquid nitrogen. Move the stage and samples to a shallow dish filled with liquid nitrogen: deep enough to cover the stage and samples at all times, but shallow enough to see and manipulate them precisely.
3. Bend side tabs of samples back to a tight position and slide the tabs onto the copper stage.

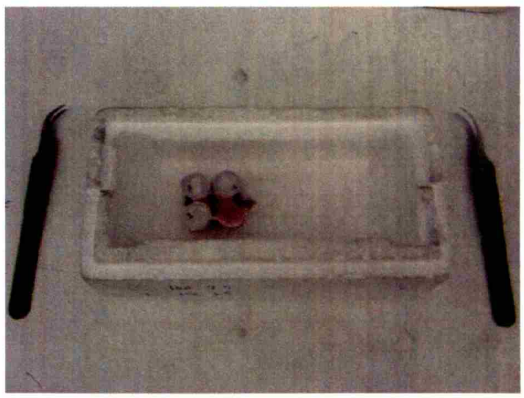

4. Attach mounting arm to stage (using a pair of forceps to hold pin while manipulating). Make sure stage and samples never emerge from liquid nitrogen.

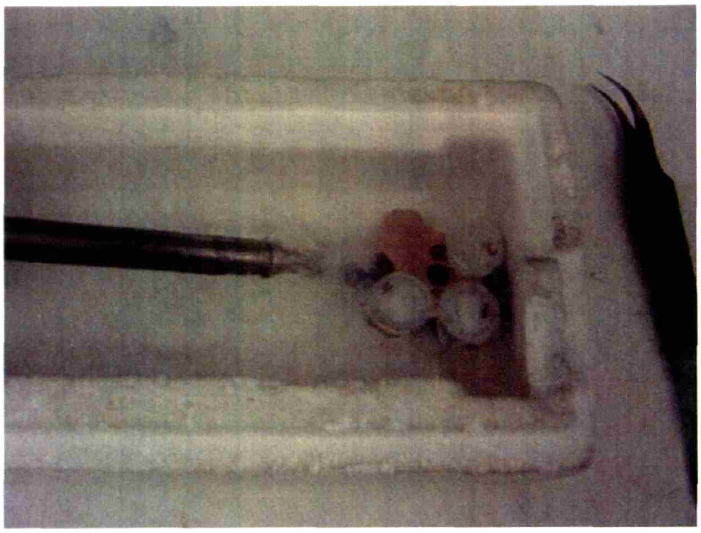

5. With port pump on, insert arm into the loading port and pull grooved handle all the way out to being pumping. After about 10 seconds, push handle to middle position, rotate counterclockwise to open door, and insert stage into chamber.

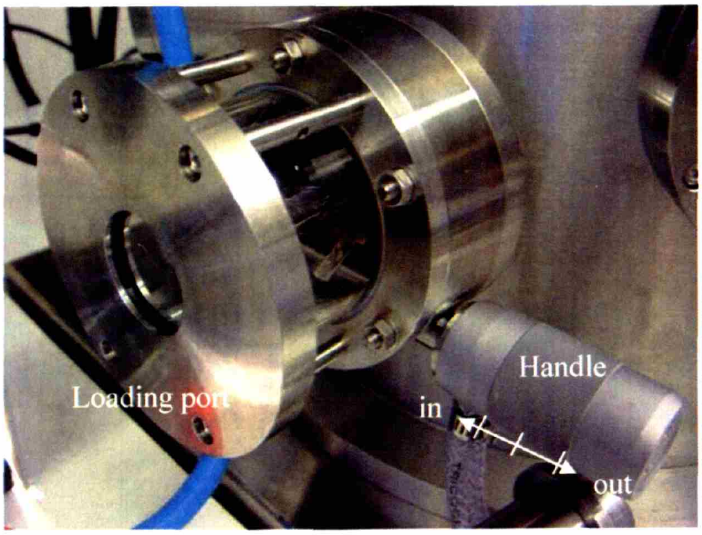

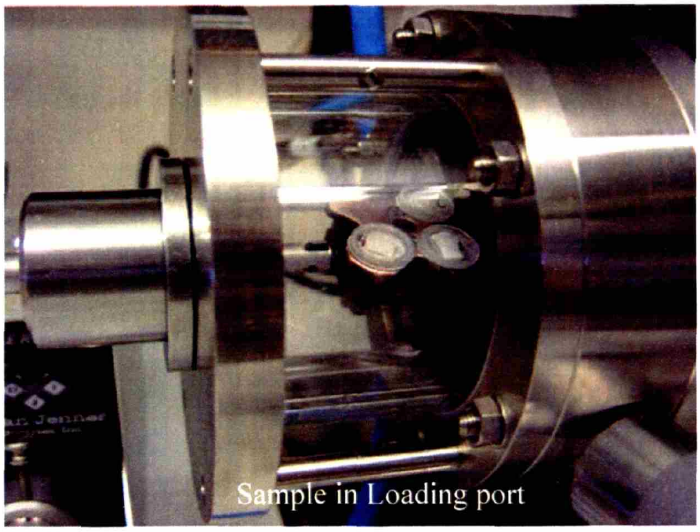

6. The copper stage aligns with the center table. The pin must be vertical (north/south) for the stage to slide into the table. Once it is in, turn the pin horizontal (east/west) to lock the stage in place, and retract the arm to the port. Close the door to chamber. Press the handle all the way in, ejecting the mounting arm.

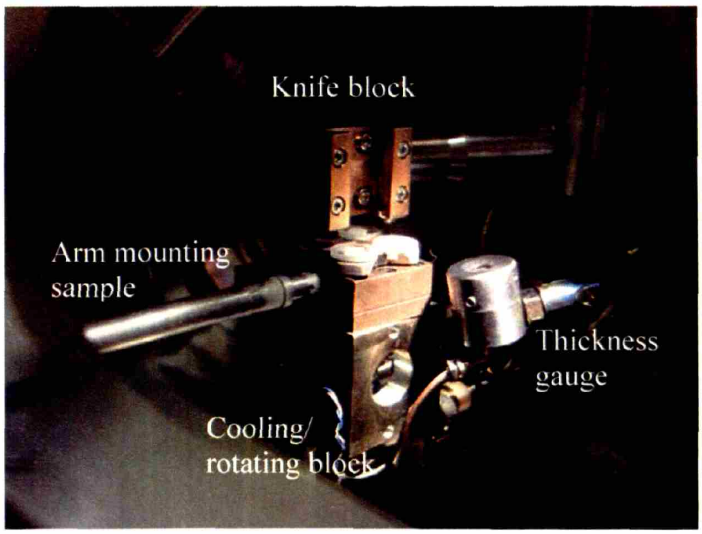

7. Bring the sample to -85°C using the heater. The table needs to be locked down in order to maintain thermal contact. The thermometer measures the temperature of the cooling block, and not the table. Under the large box protruding from the right side of the chamber is a small handle on a radial arm. When the arm is in the nearest notch it is locked down, at all other positions it is free to spin and not in contact with the block.

Scraping sample surface (for actin networks, not cells):

1. Bring the knife next to the sample. Adjust the knife height so that it barely touches the coverslip.
2. Swing blade forward to shave sample.
3. Repeat until a fine layer is removed to your satisfaction. On the final cut do not return the blade to the back position because you do not want to drop shavings onto the sample on the return swing. Raise the knife a bit.
4. Allow a two minute "etch" by exposing the surface to the cold vacuum for 2 minutes. This allows the water to evaporate from the sample. The time can vary from 2 minutes to an hour depending on the depth of the etch desired.

Coating the Sample with Platinum or Tantalum

Platinum or tantalum-tungsten is the high contrast electron-dense metal used to coat the sample for EM visibility. Carbon is added for sample durability.

There are two density settings, A and B. The density setting for Ta-Tn is 17.7 g/ml, Pt is 22.9 g/ml, and C is 2.2 g/ml.

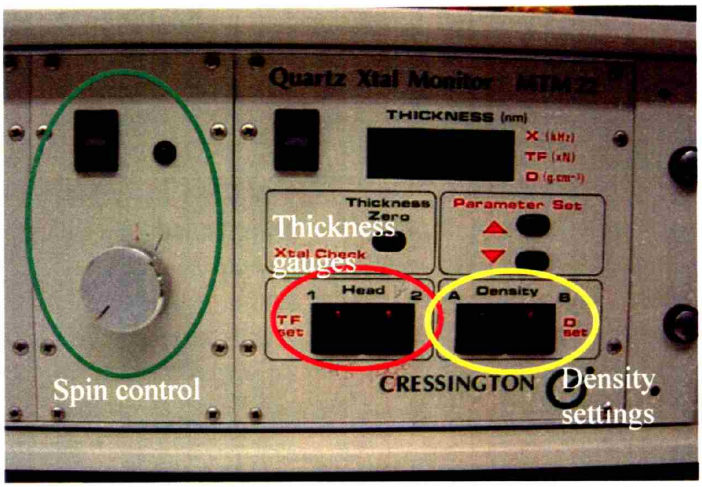

There are two sensors for metal deposition amount, heads 1 and 2. One head is set to measure deposition from 45 or 90 degree guns; the other for 5 or 10 degree guns. The wiring can be easily rearranged, so doublecheck which head is connected to which number. Before spraying, reset the height to 0 nm.

There are two guns connected to each control unit, so the buttons are arranged:

Degas 1 – Degas 2 – Preset 1 – Preset 2 – Manual 1 – Manual 2

The settings for each metal rod are:

Carbon	105 mA	2.4 kV	
Pt	75	1.9	
Ta-Tn	180	3.8	(must be water chilled during use)

1. Degas the guns before use by pressing the appropriate button.

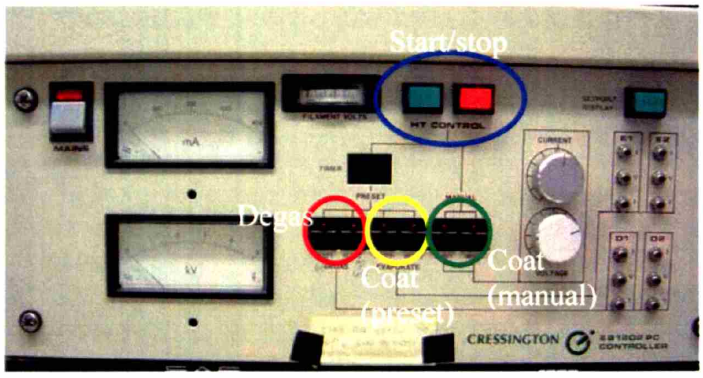

2. Rotate the sample when coating with the 5 or 45 degree guns, which are off-center. Unlock the table and increase rotation slowly until the sample spins approximately once per second.

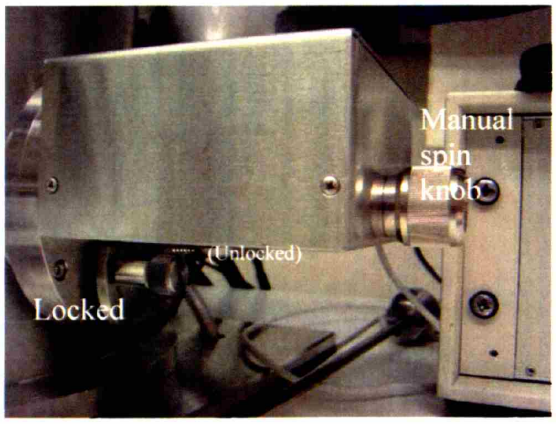

3. Move the knife housing over the sample to act as a shield. Press the appropriate button for the gun being used and after 1-2 seconds of equilibration, move the knife out of the way to expose and coat the sample. Apply approximately 1.5 nm of metal.
4. Stop the rotation and lock table down in its original orientation with the pins on the left. Verify the proper spray gauge and the proper density on the control box. Reposition the knife housing over the sample as before. Reset the gauge thickness to zero.
5. Evaporate 5 nm of carbon onto the sample.
6. Remove the sample using the same procedure as inserting it by pumping down the loading port, opening the door, removing the stage, and closing the door. Vent the loading port slowly in order to prevent air currents from blowing away the coverslips.

Dissolving the sample from the replicas on glass coverslips

1. At room temperature, remove the tabs from the stage by loosening the screw and sliding them into a Petri dish. Do not reuse the copper block until it equilibrates to room temperature.
2. In a fume hood, prepare 24% HF acid in a small Petri dish. By dipping a wire into Photoflo, add a trace amount of desurfactant to the HF to prevent surface tension from ripping the thin replica into fragments. (*HF is dangerous!*)
3. After the coverslip has thawed and dried, use forceps to immerse the coverslip at a low angle into the HF. Surface tension will wick HF in between the replica and the glass, and when the two have separated, release the forceps. The coverslip will fall to the bottom of the HF, and the replica will be floating on the surface.
4. Fill a ceramic tray of "bowls" with as many rows of pure water as samples, with two bowls in each row. Using a bent pipet, immediately move the replica from the HF to a bowl which has also been treated with desurfactant.
5. Using a bent glass pipette, move the sample to the first dish and let the water dilute residual HF for five minutes. Move the sample to the next bowl for additional dilution.
6. Using sharp forceps, pick up the edge of a formvar-coated grid.
7. Immerse the grid perpendicular to water surface, approach sample and pick up as large a section as possible.
8. Blot the edge of the grid with filter paper to remove excess water. Once the replica is completely dry, slide a small piece of filter paper between the forceps as you release the grid into a grid holder. If the forceps are wet or paper is not used to eject the grid from the forceps, surface tension will wick the grid inside the forceps and destroy the sample.

Glycerol Coating of Mica

This method is preferable to freeze-etching for the viewing of individual proteins in the electron microscope. The proteins are diluted in a 50% glycerol solution and sprayed onto freshly cleaved mica. The mica is placed into a vacuum chamber where it evaporates and recedes, leaving proteins adsorbed to the mica surface, which can then be shadowed and mounted on grids.

Description of equipment:

The apparatus consists of a nozzle and a target. The nozzle is connected to a nitrogen gas line at 35 psi, and the target is a metal plate located 25 cm away from the nozzle on an adjustable track. A pipet tip is placed perpendicular to the nozzle orifice. A burst of nitrogen gas sprays the sample onto freshly cleaved mica adhered to the taget. The N_2 does not push the sample through the tip, but draws it out by passing across the orifice (Venturi effect). The distance from tip to tape for good uniform spraying needs to be optimized for each system, as does the location where the small mica sections are attached to the target. Spraying onto a large slide gives a good visible indication of droplet dispersal patterns. The nitrogen pressure should also be optimized.

1. On 5 mm by 5 mm sections of mica write asymmetrical labels on both external faces. Use forceps to pry apart the layers of mica, splitting each section into two sections.
2. Mount the mica sections onto the tape with the freshly cleaved internal surfaces facing the nozzle.
3. Load 25λ of 50% glycerol-protein solution into a pipet tip. Mist the solution onto the mica with the nitrogen tank by pressing the release valve.
4. Remove the mica sections and place them (sprayed side up) on a piece of double-sided tape on a copper stage.
5. Coat the samples as described above with two exceptions
6. Once sprayed, dip the mica into untreated DDH_2O to remove the coating. Dip grids into 10% formic acid to deoxygenate them, and then into water to clean them, and then mount the replicas onto the grids.
7. View the samples at 80 kV because lower accelerating voltage enhances contrast. Protein filamin molecules are found at the edges of the droplets.

Viewing the grid in the electron microscope

Using the electron microscope is a fine art, and those who know the art are loathe to share it. The general idea is that a piece of metal is heated up in a vacuum (with resistive heating) until it emits electrons. These electrons pass down the central chamber through the metal replica, and are blocked to varying degrees by the varying metal coating on the sample. The electrons that do pass through the replica strike a phosphorous screen at the bottom of the chamber, and this is what we are able to visualize. Two replicas can be inserted at a time, and by dialing 1 or 2

mechanically, the proper replica is put in the electron beam. The current and voltage of the emitting metal can be varied, and the magnification can be set from 100× to 100k×. When documentation is desired, the phosphorous screen moves out of the way and the electrons pass directly onto a film negative for a brief duration. Collected here are various notes that I've gleaned over the years, since there is no "How To," and most professionals just know and assume you already do as well, or that you don't need to. It's kind of a secret mystery cult. Anyway...

Do not touch tip of sample-loading arm. It is fragile and precise and expensive.

Using forceps, open the grid holders on the arm and place one or two samples in the correct places (sample side up). The sample at the tip is sample 1 and the proximal sample is sample 2. When you remove the grids, be sure to close the grid holders so that they do not get jammed into the chamber and snap off. Don't slam the holders shut, or they might snap the replica right off the grid (unlikely).

Put the arm in until it stops (the red light turns on) and wait for the pump to equilibrate. When the red light goes off, turn the arm 90 degrees away from you (CW) and gently allow the pump to pull in the arm, using your finger as a bumper. *Do not let the arm bang forcibly into the tower* since there is a small ruby crystal on its end. You remove the arm in the exact opposite way (pull, turn, pull – but no waiting necessary).

Press HT (high tension) to turn everything on. Wait for the machine to warm up and the current to stabilize, and then turn the accelerating current up to its max (physical barrier imposed at about 72 uA). The accelerating voltage is generally set at 100 kV, but can be reduced for greater contrast. The inner mystery workings of the machine (focus) are voltage dependent.

To view the entire grid, use "Low Mag" and open the aperture on the chamber (right above eye level, turn the handle all the way to the right). Move to page N on the monitor, and center the position marker. Then adjust the dial between Grid 1 and Grid 2 so that the imge is centered on the screen. Close the aperture and change to "Magnification 2" or "Magnification 1" as needed.

Low Mag is 50-1000× (150x default)
Magnification 2 is 600-500000× (2500× default).
Magnification 1 is 25000-100000× (25000× default)
Eyepiece itself is 10×.
Use the "Selector" to change the magnification.

In order to maneuver around the grid use the right and left hand knobs. They move in orthogonal directions, and it soon becomes second nature. Some grids are labeled with letters for orientation, so take note of this when documenting a finding. Using the absolute reference

location measured by the knobs will become irrelevant if the grid is removed and viewed again later.

Brightness controls beam size and brightness (trade off). There is a 16x button that eases large changes.

There are coarse and fine focus knobs, as well as another 16x button for ease of either. Coarse itself is 16x Fine, so you can step through focusing with 1, 16, or 256 sized steps.

There is a Spot Size that a beginner uses a lot to make the image brighter, but rarely needs to be changed if everything is working right.

Shift (left and right hands) will center the beam.

There is another aperture on the left of the chamber.

There are eight pages on the keyboard. Page 1 is the most important, and it gives a good summary of all the system parameters (magnification, voltage, exposure time, photo number, etc). Page 2 is an absolute reference of where the current grid location is relative to the system. Obviously this cannot be used to mark regions of interest session-to-session since the grid will be inserted into the holder differently each session.

When taking pictures adjust brightness so that the necessary exposure time is between 0.5s (less bright) and 2s (more bright). Press Photo and phosphorous screen should rise out of way. If the machine is set on Auto Advance, the next negative will be ready. If not, you have to press the photo button to advance to the next negative, and then press it again to take the picture. Enter text by pressing the Text button the keyboard. There are only 12 characters permitted, so be clear but concise (10uM A 10:1F might mean 10 micromolar actin with 1:10 filamin:actin). Use the F No. to change to your initials if desired. The number of negatives left should be accurate, but depends on the last person to replace the film setting it to 50.

Screen can be moved manually with lever to right of viewing area.

Wobbling can be used to ease focusing. There are coarse and fine focus knobs. Pressing button to the right of the knobs will increase sensitivity 16x.

P1-3 (on page 2) must be below 36.

To take stereo images, the z-axis must be aligned. When not aligned (normal) you can switch from -10 to +10, and the image shifts. In order to align them, you push the handle behind the angle away from you, unlocking it. Then you dial the small knob below the angle until switching from -10 to +10 produces little or no shift. It is important to do this at every site, not

just once per session, since the grids are not flat. Additionally, the image needs to be focused before every photo, even in a stereo pair.

Developing photo plates from EM

1. Turn on N_2 feed into developing bins.
2. Make sure all lights are off, except the green overhead lamp, including the CRT monitor.
3. Open photo door on front of EM by turning knob CW 90 (door depressurizes for a minute).
4. Remove blank film from desiccating chamber after turning it off and venting it.
5. Once EM door has depressurized, open drawer and remove film chambers. Insert new chambers into EM and close door and lock. The EM will be equilibrated and ready to use again in approximately 30 minutes.
6. Remove exposed film from chamber (not marked "FILM") and place film negatives into film rack.
7. Submerse film rack and film into room temperature developer bin for 4 minutes, making sure N_2 is bubbling while timer is turned on.
8. When developer is done, submerse film in Stop bin for 1 minute. Switch N_2 to Stop bin.
9. When Stop is done, submerse film in Fixer bin for 10 minutes. Switch N_2 to Fixer bin.
10. When Fixer is done, submerse film in running water bin for 30 minutes. Turn off N_2.
11. When wash is done, place film in dryer for 60 minutes.

D-19 developer:

1. Pour old developer from its bin down the drain. To prevent leaks, do not disturb the stopper.
2. Heat 1500 ml of water to 55 C (130 F), and mix with 1500 ml of room temperature water for a combined temperature around 38 C (100 F).
3. Stir in D-19 powder from packet until dissolved into a light yellow solution.
4. Pour developer into developer bin and dilute with distilled water until the developer bin is full enough to cover film submersed in the film rack (approximately 3×).

Changing the 90 (carbon) gun

The 90 gun door operates exactly as the sample door, the only difference is that the gun door's default position is open and the sample door's default position is closed.

To remove the gun,

1. REMOVE POWER SUPPLY FROM GUN.
2. Raise the gun out of the door's way by pulling the handle up and locking.
3. Close the door by turning the port handle 90 .
4. Vent the port by pressing the port handle in.
5. Unscrew and remove gun. It will be hot if it was fired recently.

To install the gun,

1. Clean all O-rings and surfaces from debris using ethanol. Do not use grease.
2. Screw the gun in place, making sure gun is opposite door hinge (there are six configurations).
3. With the port pump on, pull the port handle out to evacuate the port.
4. After a minute, push the port handle in halfway and turn to open the door.
5. Lower the gun.
6. Reattach the power supply.

The knife is also changed through this port, using a circular template and the mounting arm. Once the door is closed, replace the gun fixture with the circular template so that the gun port looks like the sample port, insert the arm into the chamber, and withdraw the knife.

Venting the chamber (Changing any non-90 gun with no door)

To modify a generic access port (5 degree Pt or 45 degree TaTn for example),

1. Open the N_2 line that feeds the chamber.
2. Press the Vent button to pull in N_2.
3. Wait 2 minutes.
4. Press the Vent button again to stop the N_2 feed.
5. Open the chamber.

Press Pump to pump down the chamber when ready.